LEVEL III

OFFICE OF ONR NAVAL RESEARCH
USN

A THEORETICAL AND EXPERIMENTAL INVESTIGATION OF
VORTEX FLOW CONTROL FOR HIGH LIFT GENERATION

Richard P. White, Jr.
Santu T. Gangwani
D. S. JanakiRam

RASA Division of
SYSTEMS RESEARCH LABORATORIES, INC.
1055 J. Clyde Morris Boulevard
Newport News, Virginia   23602

D D C
OCT 10 1978
F

Interim Report for the Period 1 January - 31 December 1977

78 10 06 100

PREPARED FOR THE

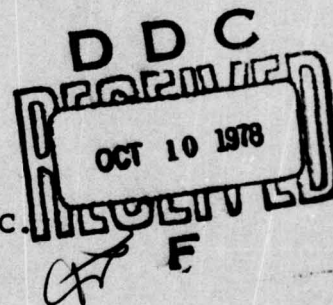OFFICE OF NAVAL RESEARCH ● 800 N. QUINCY ST. ● ARLINGTON ● VA ● 22217

A THEORETICAL AND EXPERIMENTAL INVESTIGATION OF
VORTEX FLOW CONTROL FOR HIGH LIFT GENERATION

Richard P. White, Jr.
Santu T. Gangwani
D. S. JanakiRam

RASA Division of
SYSTEMS RESEARCH LABORATORIES, INC.
1055 J. Clyde Morris Boulevard
Newport News, Virginia   23602

CONTRACT N00014-74-C-0091
ONR TASK 212-223
December 1977

Interim Report for the Period 1 January - 31 December 1977

Approved for public release; distribution unlimited.

PREPARED FOR THE

OFFICE OF NAVAL RESEARCH ●800 N. QUINCY ST. ●ARLINGTON ●VA● 22217

78 10 06 100

Change of Address

Organizations receiving reports on the initial distribution list should confirm correct address. This list is located at the end of the report. Any change of address or distribution should be conveyed to the Office of Naval Research, Code 211, Arlington, Virginia 22217.
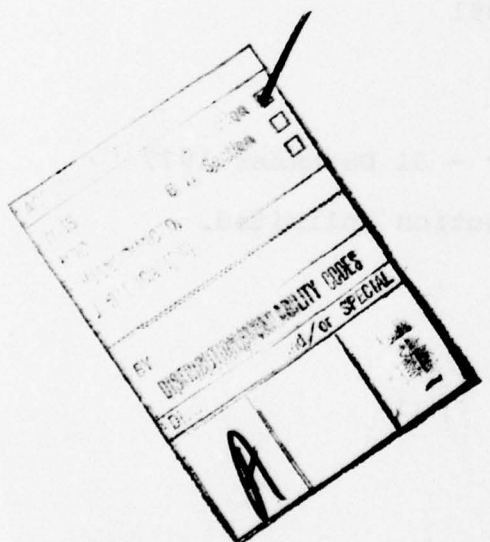
Disposition

When this report is no longer needed, it may be transmitted to other organizations. Do not return it to the originator or the monitoring office.

Disclaimer

The findings and conclusions contained in this report are not to be construed as an official Department of Defense or Military Department position unless so designated by other official documents.

Reproduction

Reproduction in whole or in part is permitted for any purpose of the United States Government.

REPORT DOCUMENTATION PAGE		READ INSTRUCTIONS BEFORE COMPLETING FORM
1. REPORT NUMBER ONR-CR-212-223-4	2. GOVT ACCESSION NO.	3. RECIPIENT'S CATALOG NUMBER
4. TITLE (and Subtitle) A THEORETICAL AND EXPERIMENTAL INVESTIGATION OF VORTEX FLOW CONTROL FOR HIGH LIFT GENERATION		5. TYPE OF REPORT & PERIOD COVERED Interim Report, 1 Jan - 31 Dec 1977
		6. PERFORMING ORG. REPORT NUMBER RASA/SRL-14-78-1
7. AUTHOR(s) Richard P. White, Jr., Santu T. Gangwani D. S. JanakiRam		8. CONTRACT OR GRANT NUMBER(s) N00014-74-C-0091
9. PERFORMING ORGANIZATION NAME AND ADDRESS RASA Division of Systems Research Laboratories, Inc. 1055 J. Clyde Morris Boulevard Newport News, Virginia 23602		10. PROGRAM ELEMENT, PROJECT, TASK AREA & WORK UNIT NUMBERS
11. CONTROLLING OFFICE NAME AND ADDRESS Department of the Navy Office of Naval Research Vehicle Technology Program (Code 211) Arlington, Virginia 22217		12. REPORT DATE March 1978
		13. NUMBER OF PAGES 130
14. MONITORING AGENCY NAME & ADDRESS(if different from Controlling Office)		15. SECURITY CLASS. (of this report) Unclassified
		15a. DECLASSIFICATION/DOWNGRADING SCHEDULE

16. DISTRIBUTION STATEMENT (of this Report)

Approved for public release; distribution unlimited.

17. DISTRIBUTION STATEMENT (of the abstract entered in Block 20, if different from Report)

18. SUPPLEMENTARY NOTES

19. KEY WORDS (Continue on reverse side if necessary and identify by block number)

vortex lift
vortex flow
stall flow

wing-vortex interactions
leading edge vortex generators

20. ABSTRACT (Continue on reverse side if necessary and identify by block number)

An experimental and theoretical program of research was conducted to determine the effect of the main wing wake on the effectiveness of the horizontal tail surface and to further refine and expand the predictive theory initiated during the previous years' effort. Experimentally, it was determined that while the vortex flows developed large pitching moments on the wing, the horizontal tail surface, regardless of its geometrical location with respect

20. to the wing MAC, was able to counter the pitching moment and trim the configuration.

The experimental data also indicated that, while large changes in the pitch angle of the horizontal tail were required to obtain configuration trim when the concentrated wing vortex wake was in the vicinity of the horizontal tail surface, the aerodynamic angle of attack remained relatively small and the tail effectiveness did not change by more than 25%.

The refined and expanded theoretical prediction method provided greater insight in the aerodynamic characteristics on the upper and lower surface and, in general, predicted the vortex flow effects more accurately. The results suggest that with the proper program streamlining and documentation the predictive program can be used successfully as a design tool.

SUMMARY

An experimental and theoretical program of research was conducted to determine the effect of the main rotor wake on the effectiveness of the horizontal tail surface and to further refine and expand the predictive theory initiated during the previous years' effort. Experimentally, it was determined that while the vortex flows developed large pitching moments on the wing, the horizontal tail surface, regardless of its geometrical location with respect to the wing MAC, was able to counter the pitching moment and trim the configuration.

The experimental data also indicated that, while large changes in the pitch angle of the horizontal tail were required to obtain configuration trim when the concentrated wing vortex wake was in the vicinity of the horizontal tail surface, the aerodynamic angle of attack remained relatively small and the tail effectiveness did not change by more than 25%.

The refined and expanded theoretical prediction method provided greater insight in the aerodynamic characteristics on the upper and lower surface and, in general, predicted the vortex flow effects more accurately. The results suggest that with the proper program streamlining and documentation the predictive program can be used successfully as a design tool.

3

FOREWORD

The work described in this technical report was performed by RASA Division of Systems Research Laboratories, Inc., for the Department of the Navy, Office of Naval Research, Arlington, Virginia, under Contract Number N00014-74-C-0091. The research program was undertaken under the technical cognizance of Dr. Robert E. Whitehead of the Vehicle Technology Program of ONR.

TABLE OF CONTENTS

LIST OF FIGURES

8

LIST OF TABLES

LIST OF SYMBOLS

A	Surface area of the wing
$\bar{c}$	Parametric constant in viscous vortex model
C_D	Drag coefficient of the wing
C_L	Lift coefficient of the wing
C_M	Pitching moment coefficient about the wing MAC
C_{Pi}	Pressure coefficient, (at point i on the wing surface)
c_r	Constant in Equation (45)
c_u	Constant in Equation (46)
c_w	Constant in Equation (44)
D	Doublet strength per unit area
d	Distance between the centerline of viscous leading edge vortex and any point on the surface of the wing
d'	$= d/r_c$
dw_t	Vertical offset between the wing and tail
H	Horizontal separation between the mean aerodynamic chords of the wing and the tail
K_1, K_2, K_3, K_4, K_5	Constants in Equations (47) and (48)
K_∞	Circulation strength of leading edge vortex divided by 2π
L	Longitudinal separation between the mean aerodynamic centers of the wing and the tail
$\vec{n}$	Unit vector normal to the wing surface
P_n	Pressure measured at the wing or tail surface
P_s	Static pressure at the tunnel centerline
P_t	Tunnel total pressure

11

Q	Volume flux in the core of the free vortex
q	Dynamic pressure
q_i	Total velocity at any point i on the wing surface
R_{c_t}	Root chord of the tail
R_N	Reynolds Number
r_c	Radius of the viscous core of the leading edge vortex
U_i	Perturbation velocity component in the x direction at point i on the wing surface
U_o	Free stream velocity
U_c	Critical velocity of the viscous leading edge vortex
V_a	Axial velocity due to leading edge vortex
V_i	Perturbation velocity component in the y direction at point i on the wing surface
V_{ic}	Tangential velocity in the chordwise direction at any point i on the wing surface
V_{is}	Tangential velocity in the spanwise direction at any point i on the wing surface
V_{in}	Velocity component normal to the wing surface at any point i
V_ϕ	Swirl velocity due to leading edge vortex
W_i	Perturbation velocity component in the z direction at point i on the wing surface
x	Kinematic eddy viscosity parameter
x, y, z	Cartesian coordinate system fixed to the wing
x_t	Distance along the free vortex after which Bachelor's model is used

α	Eddy viscosity parameter in full Equation (54)
α_t	Angle of attack of the tail with respect to the wingchord
α_w	Angle of attack of the wing
ΔC_{pv}	Incremental pressure coefficient due to leading edge vortex vortices
ΔH	Loss in total pressure in Equation (60)
ν	Kinematic viscosity of the air
ν_t	Turbulent eddy viscosity of the vortex core
θ_i	Chordwise slope of the wing surface at any point i on it
Φ	Velocity potential
ϕ	Perturbation velocity potential
ϕ_0	Velocity potential of the undisturbed flow
σ_{ij}	Velocity influence coefficient
ρ	Density of the air

1. INTRODUCTION

For the past several years, the RASA Division of Systems Research Laboratories, Inc., has been conducting an experimental and theoretical study of the vortex-flow interactions with low aspect ratio lifting surfaces under contract N00014-74-C-0091. The general objective of this study has been to investigate the concept of vortex control for the improvement of the performance characteristics of lifting surfaces, especially low aspect ratio swept wings at high angles of attack. The initial experimental investigation conducted under this contract effort (Ref. 1) showed that significant improvement on the performance characteristics of low aspect ratio swept lifting surfaces could be achieved by the use of vortex generation and control techniques. A second set of experimental results (Ref. 2) showed that a beneficial change could be effected in the lift up to angles of attack of approximately 28° by the use of leading edge vortex generators. However, further attempts to improve the maximum lift coefficient could not be achieved, partially because the flow on the outboard section of the lifting surface was difficult to stabilize.

The experimental research conducted to date has been concerned primarily with a 1/4-scale model similar to the F4E wing planform and with retrofit leading edge vortex control devices attached to it. While the test results on the configuration have shown that positive performance gains can be obtained by the interaction of the wing with the vortices generated by leading edge surfaces, it was found, however, that the pitching moment tended to become an unstable moment (nose up) with increasing angle of attack at the higher angles of attack. This is particularly true for configurations that utilized leading edge vortex generators. This unstable pitching

14

moment characteristic is realized as the large incremental lift forward of the MAC obtained on the inboard sections of the swept wing is not balanced by the lift generated by the outboard sections of the wing which are aft of the pitching moment axis and only carry small amounts of vortex lift. It was believed, however, that the magnitude of the overall pitching moment was well within the control capability of a conventional tail plane operating in undisturbed air. Because the possible interaction of the vortex flow generated by the wing with the tail plane might significantly reduce the effectiveness of the horizontal tail, it was concluded that the effectiveness of the horizontal tail operating in the wake of the wing should be investigated. The interaction of the wing vortex flow with the tail surface is different from that of the vortex flow on the primary lifting surface, as in that case, the vortices are generated on the surface itself, whereas at the tail plane location, the vortices are free vortices. Because of the large effect that the vortices had on the performance characteristics of the primary lifting surface, their effect as free vortices on the aerodynamic characteristics of the tail plane was investigated experimentally and the results of this investigation are presented in this report.

In addition to the experimental investigation of the wing vortex flows on the effectiveness of the tail plane, development of the theoretical prediction method was continued.

In the initial work, a nonlinear theoretical prediction technique was formulated to determine the aerodynamic loads on a swept, low-aspect ratio lifting surface at high angles of attack. It involved the use of doublet lattice method along with the accounting of all the pertinent flow phenomena associated with high angle of attack, e.g., flow separation, leading edge and tip vortex flows, etc. Favorable correlation

15

between measured and predicted results was shown both in the total lift and in the loading distributions. Due to some inherent assumptions involved in the analysis, however, its prediction capabilities were limited. For example, in the original formulation, the no-flow boundary conditions were satisfied along the mean camber line of the airfoil. This resulted in the omission of the thickness and the curvature effects in the computation of surface potential pressures.

In the study, presented herein, the original formulation has been extended so that flow tangency boundary conditions can be satisfied on the true wetted surface of the wing instead of only the upper surface. This enables the computation of surface pressures individually on the upper and lower airfoil surfaces. In addition, a better and more realistic mathematical model than the one utilized in Reference 2 was developed for the representation of the leading edge vortex system. The new representation of the leading edge vortex system has been derived under the basic assumption that the velocity in the core is very large in comparison with the velocity outside the vortex viscous core. Also, the radial flow has been included in the representation of the vortex core flow. The resulting solution has been utilized for the prediction of suction pressure peaks in the vicinity of leading edge vortices.

Since the thickness and chordwise slope of the airfoil has been included in the analysis, it has resulted in an improved determination of fully separated flow regions on the surface. Additionally, a new criterion for the prediction of vortex breakdown phenomenon has been incorporated in the program. This criterion is based on the theory of finite transition and it implies that when the axial velocity in the core reaches a certain velocity (critical velocity) the vortex is assumed to have burst.

16

2. DESCRIPTION OF MODEL AND INSTRUMENTATION

2.1 Model

The model for this experimental investigation consisted of two lifting surfaces, a basic wing panel with suitable leading edge attachments and a tail plane. Both the lifting surfaces are semi-span models similar in geometry to and approximately 1/4-scale versions of the F-4 phantom wing planform and its horizontal tail. The model wing and tail, however, have no diheral unlike those of the F-4 phantom aircraft. A picture of the wing tail model in the wind tunnel is shown in Figure 1.

The basic wing panel has a nominal leading edge snag starting at the 68% semi-span and extending to the tip. The basic wing was tested with and without a root strake. The wing panel as well as the root strake employed were exactly the same as those used in earlier tests and a detailed description of these configurations was given in Reference 1.

A planform sketch of the basic wing panel with the root strake is shown in Figure 2. The root strake consists of a triangular shaped leading edge extension. The base of the triangular strake increased the root chord of the basic planform by 38% and its leading edge was swept 75% with respect to the free stream. Pressure taps were installed at 220 locations on one side of the wing panel. The locations of the pressure taps were shown and listed in Reference 2.

A 1/4-scale semi-span model approximating the F-4 tail planform but with no dihedral was designed and fabricated. The tail plane model was constructed of wood and had a NACA 0006 airfoil section. A planform sketch of the tail plane with all the dimensions listed is given in Figure 3 and Figure 4 presents a photograph of the tail surface. Pressure taps were installed at 98 locations on the tail surface, half

17

of which are on one side and the other half on the other side. The locations of these pressure taps on the tail surface are shown in Figure 5 and tabulated in Table I.

The model incorporated provisions for mounting the tail plane at various lateral and longitudinal distances from the wing panel as well as means of remotely controlling the angle of attack of the tail surface relative to the wing about a vertical axis passing through its mean aerodynamic center.

2.2 Instrumentation

Forces and moments on the model system, the wing and tail plane, were measured by a six-component, yoke-type balance located beneath the floor of the test section at the University of Maryland wind tunnel facility (Reference 3). The balance measurements were monitored on-line prior to off-line computer processing into the lift, drag, and side force, and the pitch, roll and yawing moment coefficients based on the planform area of the wing. The forces and moments were resolved into a wind-axes coordinate system. The pitching moment was taken about an axis which passes through the quarter chord line of the mean aerodynamic chord, and the rolling and yawing moments were taken about the wing root. A sketch of the coordinate system is shown in Figure 6.

The balance system that was used to record the total force measurements at the University of Maryland wind tunnel has the following accuracy:

Lift	± 0.5 lb
Drag	± 0.1 lb
Side Force	± 0.2 lb
Pitching Moment	± 0.2 ft-lb
Rolling Moment	± 0.2 ft-lb
Yawing Moment	± 0.2 ft-lb

18

The data for the tests was reduced to coefficient form using
the following constants:

$$A = 16.570 \text{ ft}^2 \text{ (wing and snag)}$$
$$= 17.580 \text{ ft}^2 \text{ (wing and snag and strake)}$$
$$q = 11.89 \text{ lbs/ft}^2 \text{ (dynamic pressure)}$$
$$\bar{c}_W = 4.01 \text{ ft (wing mean aerodynamic chord)}$$
$$s = 4.8 \text{ ft (wing semi-span)}$$

The coefficients were then transferred from the balance center
directly down to the floor of the test section (vertical dis-
tance of 3.469 ft). The forces and moments were then trans-
ferred to the wind axes at the main wing (see Figure 6). After
transferring the data to the wind axes at the wing, corrections
were applied to the balance measurements to account for wind
tunnel wall and blockage interference effects according to the
following relationships, which were derived from References 4
and 5.

$$\alpha = \alpha_m + 1.57008 \, C_L$$
$$C_D = C_{D_m} + .02247 \, C_L^2$$
$$C_M = C_{M_m} + 0.004646 \, C_L$$

The total C_L (wing and tail) was used to calculate these cor-
rections. Further appropriate corrections to the data as de-
scribed in Reference 1 were not made as the tests were conducted
primarily on a comparative basis.

For the pressure measurements, the transducers in
each scanivalve were calibrated against the central manometer
system of the University of Maryland wind tunnel. The wind
tunnel total, static and the centerline static pressure were
monitored from three ports in each scanivalve. The normal
sensitivity of the pressure measurement system yielded a
resolution of $\Delta P/q = \pm.01$. Since the system measures the
steady pressures instantaneously, the mean rms pressures may
not always be measured, particularly for stalled flow.

19

The pressures at the 220 pressure taps located on the semi-span wing model were recorded from the pressure transducers housed in five 48-port scanivalves. Three ports on each scani-valve monitored the tunnel total, static and tunnel centerline static pressures. Similarly, the pressures at the 98 pressure taps located on the semi-span tail model were recorded from the pressure transducers housed in a different set of scanivalves. The pressure transducers were calibrated in the range of ± 2.5 lb/in^2. The pressure measurements were recorded on punched cards and were converted to coefficient form, $\Delta P/q$ as follows:

$$\Delta P/q = (P_s - P_n) / |P_t - P_s|$$

where P_s is the static pressure at the tunnel centerline, P_n is the pressure measured at each port and P_t is the tunnel total pressure.

2.3 Model Installation

Each configuration of the wing-tail system tested differed from the other in two parameters: (1) The longitudinal separation between the wing MAC and tail MAC (L); (2) The horizontal separation (H) between the wing mean aerodynamic chord and that of the tail. A given configuration had a specific value for L and H, which were set using the turntable mechanism on the floor of the test section. The model arrangement on the turntable for a typical configuration is shown in Figure 7. For given values of L and H, the turntable (and hence the balance beam underneath) was rotated clockwise (looking from the top) through an angle ϕ' where $\phi' = \sin^{-1} (H/L)$. After mounting the wing and tail on the balance beam, their chord lines were aligned with the free stream such that they were at a geometric angle of attack of zero degrees (see Figure 7). The configuration was tested at various angles of attack, by rotating the turntable counter-clockwise (looking from the top) through α degrees and the distances between the wing and tail remained the same.

20

3. WIND TUNNEL TESTS

The wing-tail configuration, as discussed earlier, is specified by two geometric parameters: (1) The longitudinal separation between the wing MAC and tail MAC (L) in inches; (2) The horizontal separation (H in inches) between the wing mean aerodynamic chord and that of the tail. Apart from these the wing itself had two basic configurations: (1) wing plus conventional snag and, (2) the wing plus snag with the root strake added.

Wing configurations with two different values of L and five different values of H were tested. These are:

$L_1 = 75"; L_2 = 60";$

$H_1 = 0; H_2 = (0.3)Rc_t; H_3 = (0.6)Rc_t; H_4 = (0.9)Rc_t;$

$H_5 = (1.2)Rc_t$

where Rc_t is the root chord of the tail in inches. The tests conducted can be broadly classified into two types. (1) Wing along with and without the root strake, but at the same orientation and position which it would have with the tail at the various longitudinal and horizontal separations; (2) Wing-tail combinations, each of which differs from the other in the values of L and H. Basic wing as well as wing with strake were tested in combination with the tail.

Each configuration was represented by a five digit number followed by a letter A or B. The first digit can be either 1 or 2 where 1 refers to the basic wing with an outboard snag and 2 refers to the basic wing plus snag and a root strake. The second and third digits together give the longitudinal separation (L) in inches. The fourth and fifth digits together give the offset (H) in tenths of root chord of the tail. The letter A denotes the wing alone configuration

21

and the letter B denotes the wing-tail configuration. For example, 2-75-06-B designates a configuration with the basic wing, snag and the tail where L = 75" and H = 0.6 Rc_t.

Associated with each configuration is a specific initial turntable angle, ϕ', at which both the wing and tail are mounted, each aligned in the free stream direction. Each configuration is set up as per the procedure described earlier.

The current tests were conducted at a Reynolds number of 2.5 x 10^6 based on the wing MAC and a dynamic pressure of 11.89 lbs/ft^2. The primary purpose of this test program was to find the effect if any of the vortex flow generated by the main wing on the tail surface, especially at large angles of attack.

The first series of tests conducted involved wing alone configurations (with and without strake), with the wing at the same orientation and position which it would have with various wing-tail configurations. Balance data was taken for these configurations at various angles of attack ranging from 0° to 30° by turning the turntable through an appropriate angle.

The next series of tests involved wing-tail configurations with various values of L and H. With the tail present, at each wing angle of attack, the angle of attack of the tail was varied until the wing tail combination had zero pitching moment about the wing MAC. Balance data as well as pressure measurements on the wing and tail were taken at this approximate trim condition. The angle of attack of the tail was then varied $\pm4^o$, $\pm8^o$ about its approximate trim angle and at each tail angle of attack (wing angle of attack remaining constant), the balance data as well as pressure measurements were taken, to determine the effectiveness of

22

the tail. This procedure was repeated for a number of angles
of attack of the wing. The wing angles of attack chosen were
8°, 16°, 20°, 24°, and 28°. A description of the configurations
that were tested are given in Table II.

4. DESCRIPTION OF THEORETICAL PREDICTION MODEL

In the recent years, the prediction of aerodynamic loads on lifting surfaces of various shapes by lifting surface theory has been developed rather extensively (e.g., References 6, 7, and 8). The simplest lifting surface methods for predicting aerodynamic loads are limited to flows at low angles of attack (linear methods). In these cases, the lattice representing the surface and the wake consists of elements which are parallel and normal to the free-stream velocity. In the nonlinear methods, this constrained representation is relaxed so as to account for leading edge and tip vortex systems and also to account for flow separation, etc.

In an earlier effort of the present contract (Reference 2) a nonlinear theoretical prediction technique was formulated to determine the aerodynamic loads on a swept, low aspect ratio lifting surface at high angles of attack. It involved the use of doublet lattice method along with the accounting of all the pertinent flow phenomena associated with high angle of attack, e.g., flow separation, leading edge and tip vortex flows, etc. Favorable correlation between measured and predicted results was shown both in the total lift and in the loading distributions. Due to some inherent assumptions involved in the analysis, however, its prediction capabilities were limited. For example, the no-flow boundary conditions were satisfied only along the mean camber line of the airfoil thus ignoring the thickness and the curvature effects for the computation of surface potential pressures.

In the present study, the previous analysis has been extended so that flow tangency boundary conditions can be satisfied on the true wetted surface of the lifting surface instead of only the mean camber line which enables the

24

computation of surface pressures on the upper and lower surfaces of the airfoil separately. The present analysis to be discussed herein, has a more realistic mathematical model for the representation of the leading edge vortex system than the one previously utilized in Reference 2. The new representation of the leading edge vortex system has been derived under the basic assumption that the axial velocity in the core is very large compared to the velocity outside the vortex viscous core. Also the radial flow has been included in the representation of the vortex core flow.

Since the thickness and chordwise slope of the airfoil profile has been included in the analysis, it has resulted in an improved determination of fully separated flow regions on the surface. Additionally, a new criterion for the prediction of vortex breakdown phenomenon has been incorporated in the program. This criterion is based on the theory of finite transition and it implies that when the axial velocity in the core reaches a certain velocity (critical velocity) the vortex is assumed to have burst.

A more detailed description of the above-mentioned analyses and modifications are included in the following sections.

4.1. General Formulation

4.1.1. Statement of the Problem

The objective of the analysis procedure developed herein is the prediction of the aerodynamic loads of low aspect ratio lifting surfaces operating at high angles of attack, by a simple but inclusive analysis.

The steady subsonic flow over a swept, low-aspect ratio lifting surface of arbitrary shape is considered herein and a nonlinear lifting surface theory is utilized to predict the aerodynamic loads on the lifting surface at moderate to high angles of attack. All the pertinent flow phenomena at high angles of attack are included in the analysis. More specifically, the nonlinear prediction of aerodynamic loads on a lifting surface is formulated so as to include the suction effect of the free vortices and to account for vortex bursting and flow separation. The vortex flows are represented as viscous line vortices by means of a finite element approach during their formation and life over the wing surface. The vortices are considered to be "free" as they are allowed to move due to the mutually induced interaction with the wing and each other. Once the stabilized positions of the vortices with respect to the lifting surfaces are achieved, the spatial distribution of vortex suction lift is computed by determining the suction pressure required to balance the centrifugal force of the swirling vortex flows and adding these pressures to those suction pressures developed by the axial flows.

4.1.2. Potential Flow Formulation

4.1.2.1. Basic Equations

Consider a Cartesian coordinate system attached to the wing and as shown in Figure 8, the x-y plane describes

26

the zero-mean angle of attack plane of the wing and z-axis is directed away from the upper surface of the wing.

Potential flow implies that the flow is irrotational so that the velocity vector $\vec{V}$ can be expressed by the gradient of a velocity potential Φ,

$$\vec{V} = \vec{\nabla} \Phi \tag{1}$$

Since the continuity equation is given by

$$\vec{\nabla} \cdot \vec{V} = 0 \tag{2}$$

for incompressible steady potential flows, the velocity potential Φ of the flow around a wing surface satisfies the Laplace equation

$$\nabla^2 \Phi = 0. \tag{3}$$

Therefore the problem of determining the steady, inviscid, irrotational, and incompressible flow around a wing surface described by a boundary surface S, involves the solution of the Laplace equation

$$\frac{\partial^2 \Phi}{\partial x^2} + \frac{\partial^2 \Phi}{\partial y^2} + \frac{\partial^2 \Phi}{\partial z^2} = 0 \tag{4}$$

with appropriate boundary conditions. After the velocity potential Φ is determined, the velocity can be obtained from Equation (1) and the pressure can be obtained from Bernoulli's equation.

For convenience Φ is separated into two parts, i.e.,

$$\Phi = \phi_0 + \phi . \tag{5}$$

Here, ϕ is the perturbation velocity potential, which vanishes in very far regions and ϕ_0 is that part of the potential which gives the free stream velocity, i.e.,

$$\vec{U}_0 = \vec{\nabla} \phi_0 . \tag{6}$$

27

4.1.2.2. Boundary Conditions

The Laplace equation being a second order differential equation requires two boundary conditions for its solution. In the regions very far from the wing, the perturbation potential is zero or the total velocity at large upstream distances corresponds to the free stream velocity $\vec{U}_0$. The second boundary condition, related to the requirement for flow tangency, states that over the wing surface S, the normal velocity $\vec{V}_n$ should be zero, i.e.,

$$\vec{\nabla} \phi \cdot \hat{n} = 0 \tag{7}$$

where $\hat{n}$ is the surface unit normal. The boundary condition Equation (7) can be rewritten in terms of the perturbation potential and the free stream velocity after combining Equations (5) and (6) as follows:

$$\vec{\nabla} \phi \cdot \hat{n} = - \vec{U}_0 \cdot \hat{n} \tag{8}$$

For convenience $\vec{\nabla} \phi$ can be defined as the induced velocity vector $\vec{v}_i$, which allows the boundary condition, Equation (8), to be written as

$$\vec{v}_i \cdot \hat{n} = - \vec{U}_0 \cdot \vec{n} \tag{9}$$

The above boundary conditions and the Kutta condition, which will be discussed in a later section, are utilized for the determination of the perturbation potential ϕ.

4.1.2.3. Solution of the Laplace Equation

It can be shown that the potential function induced by singularities such as a source, or doublet will identically satisfy the Laplace equation and will vanish at infinity. Therefore, the solution of the Laplace equation is one of finding a singularity distribution on the surface S that satisfied the normal boundary conditions in Equation (9).

28

Since a source distribution alone does not produce any
resultant lift, the doublet distribution has
been utilized in the present formulation.

If "D" corresponds to a surface doublet distribution
whose axis is everywhere along the outward normal to the local
surface S, the potential induced at any point P is given by

$$\phi_p = -\iint_S \frac{D}{4\pi} \frac{\hat{n} \cdot \vec{r}}{r^3} \, ds \tag{10}$$

where $\vec{r}$ is the distance vector from doublet source "D" on S
to point P, and $\hat{n}$ is the unit vector outward normal on the
elemental local surface ds and S is the total surface on
which doublets are distributed. In general, the surface S
consists of the upper and lower surfaces of the lifting sur-
face and the wake surfaces.

Substitution of Equation (10) into Equation (8)
results in the following integral equation

$$\frac{1}{4\pi} \vec{\nabla} \iint_S D \frac{\hat{n} \cdot \vec{r}}{r^3} \cdot \hat{n} = -\vec{U}_0 \cdot \hat{n} \tag{11}$$

In the present analysis the integration of the above equation,
for the determination of doublet distribution D, is carried
out numerically.

4.1.2.4. Numerical Method of Solution

In order to carry out the integration of Equation
(11), the surface of a semi-wing is assumed to be divided
into a finite number of quadrilateral elements as shown in
Figure 8. The value of the doublet strength D is assumed
to be constant over each surface element and it is assumed
that the axis of the doublet is directed along the local
surface normal at each control point which is at the centroid

29

of each element. A numerical procedure is then utilized such that Equation (11) is satisfied at a finite number points corresponding to the centroids of the various elements representing the wing surface.

It can be shown, by analogy with electromagnetic theory, that the flow induced by a doublet distribution of density "D" over a given area is the same as that due to a vortex of strength D around its boundary. Therefore, numerically the doublet distribution on the surface of the wing corresponds to a network of vortex elements as indicated in Figure 8. Once the strengths of the vortices is obtained, the Biot-Savart law is utilized to obtain the velocity field induced by the network of vortex elements. The manner by which this is accomplished will be discussed in the following paragraphs.

Let N be the total number of elements representing the upper and lower surfaces of a lifting surface. Since it is assumed that the load distribution is symmetric, only a semi-wing need be considered. It is noted, however, if it is desired to include the effect of the loading from the other half of the wing, a mirror image of the loading on the semi-span wing must be utilized for symmetrical loads. For un-symmetrical loadings a similar representation of the complete lifting surface from tip to tip would have to be utilized. Let v_{n_i} be the flow induced by the doublet distribution at the ith control point in the direction of the negative local normal (inward normal), then in general, it can be written that

$$v_{n_i} = -\vec{v_i} \cdot \vec{n} = \sum_{j=1}^{N} \sigma_{ij} D_j \qquad (12)$$

Here σ_{ij} is the total influence coefficient of all the vortex elements of unknown strength D_j.

30

In general σ_{ij} is a function of the relative distance and orientation of the vortex elements (assumed to have unknown strength D_j) with respect to the location of the control point i and the angle with respect to the local normal associated with the control point. Physically, σ_{ij} is the downwash velocity normal to the local surface at the control point i (along the local negative normal) due to a doublet distribution of unit strength located at element j and its image. The angle θ_i defining the slope of the unit normal vector at control point i on the airfoil surface is given by

$$\theta_i = \tan^{-1} (dz/|dx|) \tag{13}$$

If a_{ij} and c_{ij} are the induced velocities at point i in the positive x- direction and in the positive z- direction respectively, due to the unit doublet distribution at element j, then σ_{ij}^u along the local inward normal on the upper surface face can be defined as:

$$\sigma_{ij}^u = -(c_{ij} \cos \theta_i + a_{ij} \sin \theta_i). \tag{14}$$

For the lower surface σ_{ij}^l is

$$\sigma_{ij}^l = (c_{ij} \cos \theta_i + a_{ij} \sin \theta_i) \tag{15}$$

The free stream velocity component in the local outward normal direction U_{ni}^u for the control point i on upper surface is expressed as

$$U_{ni}^u = U_0 \sin (\alpha_0 - \theta_i) \tag{16}$$

The corresponding free stream component U_{ni}^l for the control point on lower surface is given by

$$U_{ni}^l = - U_0 \sin (\alpha_0 - \theta_i) \tag{17}$$

In Equations (16) and (17) α_0 is the geometric angle of attack of the mean line of the wing and U_0 is the magnitude of free stream velocity as indicated in Figure 8.

The problem of solving the integral Equation (11) has now been reduced numerically to the solution of a linear set of N equations, which was obtained

$$\sum_{j=1}^{N} \sigma_{ij} d_j = - U_0 \sin (\alpha_o - \theta_i) \qquad (18)$$

by combining Equations (9), (12), (14), (15), (16) and (17).

In Equation (18) the superscripts u and l have been dropped since σ_{ij} is the general expression for the influence coefficient given by

$$\sigma_{ij} = c_{ij} \cos \theta_i + a_{ij} \sin \theta_i \qquad (19)$$

So far, in the development of the equations in the form for numerical solution, the effect of the wake has not been considered. It can be shown, by using the Helmholtz vorticity theorem, that the doublet strengths on the wake are constant along each streamline; and by imposing the Kutta condition, their magnitudes are equal to the difference of the doublet strength evaluated at the trailing edge. Therefore, in general, the doublet strength on each wake element can be expressed in terms of the doublet strength imparted to a particle as it leaves the wing surface. Thus, the elements on the wake do not introduce any new unknowns. Once the wake geometry is prescribed, the influence of all the wake elements along the same streamline can be summed in the streamline direction and included as part of the coefficients a_{ij} and c_{ij} in Equation (19).

4.1.2.5. Determination of Pressure Coefficients Over the Wing Surface.

Bernoulli's equation is utilized for the determination of wing pressure loading under the assumptions of potential flow. The pressure coefficient at any point i may be defined as c_{pi} where

32

$$c_{pi} = 1 - q_i^2 / U_0^2 \qquad (20)$$

and q_i is the total velocity at point i.

Let u_i, v_i, and w_i be the perturbation velocity components at point i in the x, y, and z directions respectively, then the total velocity in the chordwise tangential direction v_{ic}, the spanwise tangential direction v_{is} and in the normal direction v_{in} can be expressed in terms of u_i, v_i, and w_i as follows:

$$v_{ic} = -u_i \cos \theta_i + w_i \sin \theta_i + U_0 \cos (\alpha_\circ - \theta_i) \qquad (21)$$

$$v_{is} = v_i \qquad (22)$$

$$v_{in} = w_i \cos \theta_i + u_i \sin \theta_i + U_0 \sin (\alpha_\circ - \theta_i) \qquad (23)$$

Here, v_{in} is zero due to the boundary condition of no flow through the wing surface. Substituting Equations (21), (22) and (23) into Equation (20) results in the following expression for the pressure coefficient:

$$c_{pi} = 1 - \cos^2 (\alpha - \theta_i)$$

$$-\left[-u_i / U_0 \ \text{ços} \ \theta_i + w_i / U_0 \ \sin \theta_i\right] (2\cos(\alpha-\theta_i)$$

$$-\left[- u_i / U_0 \cos \theta_i + w_i / U_0 \sin \theta_i\right]^2 - (v_i / U_0)^2 \qquad (24)$$

The perturbation velocity components in the two tangential directions, v_{ic} and v_{is}, are obtained from the doublet distribution, D, in the manner outlined in the following paragraphs.

33

The average velocity vector $\vec{V}_i$ at any control point is computed from the gradient of the potential defined by Equation (10):

$$\vec{V}_i = - \vec{\nabla}_i \iint_S \frac{D}{4\pi} \; \frac{\hat{n} \cdot \vec{r}}{r^3} \, ds \tag{25}$$

During the numerical computation of $\vec{V}_i$ the contribution of the surface element at which the coefficient is calculated is skipped since that element contributes only to a discontinuity in the tangential velocity. This component, of $\vec{V}_i$ due to D_i, $\nabla D/2$, is computed numerically from the surface doublet distribution, D, by using finite differences. The velocity components at i due to D_i in both the chordwise and spanwise tangential directions are then added to the corresponding average velocity components as computed by Equation (25).

34

4.2. Formulation of the Equations Describing Vortex and Suction Lift

The interaction of a concentrated free vortex with a lifting surface can be separated into two mechanisms; (1) the influence of the vortex induced velocity field, and (2) the effect of the viscous core on the near field pressure distribution of the lifting surface. The first effect is easily accounted for, as it can be included in determining the potential flow field. For example, the doublet lattice method discussed in the earlier section adequately includes the influence of the vortex induced velocity field. The second mechanism, the nonlinear suction lift is the main subject of the present section.

Due to the complexity of the equations of motion, only simplified solutions of the wing-vortex interactions problem have been obtained to date. These simplified solutions are limited to the cases such as the pressure field generated is a uniform free stream due to a Rankine or to a decaying vortex (Batchelor's solution, Reference 9) and for the case of a line vortex adjacent to a slender body. A good review of these existing theoretical models is presented in Reference 10.

In general, as indicated by the equations of motion, the incremental suction peaks obtained due to a wing-vortex interaction are the result of the radial pressure gradient term which is balanced by centrifugal and/or Coriolos forces arising from rotational flow and from axial and radial motion in the vortex flow field. This is also noted in the experimental results presented in Reference 11, where strong suction peaks are accompanied with high axial flow, core growth and vortex displacement. Therefore, it is apparent that an adequate accounting of vortex axial and radial flow is essential for the

35

correct prediction of suction peaks associated with wing vortex interactions. The Rankine vortex completely neglects axial flow, while the Batchelor vortex is valid only for weak axial flows and neither of these representations include radial flow. Since for the leading edge vortex, both the axial flow and the radial flow effects are important, it was found necessary to develop a new model which can include these effects.

4.2.1. Self-similar Solution of the Forming Vortex

It is observed that the leading edge vortex flow has some distinct characteristics such as the presence of a turbulent core at the center when the leading edge vortex sheet rolls up tightly to form a concentrated vortex. This turbulent core appears almost conical and there is a definite presence of a large axial flow in the core. These physical characteristics suggest that any mathematical representation of a leading edge vortex system should be such as to account for the large axial flow in the core compared to that outside or far away from the core of the vortex. T. R. Goodman (Reference 12) obtained a self-similar solution of the Navier-Stokes equations under boundary-layer approximations and with certain additional assumptions. This solution of the vortex flow includes the characteristics similar to those of a leading edge vortex system during its formation.

As previously mentioned, the leading edge vortex system contains a central core where viscous effects predominate. A characteristic feature of this core is the presence of a strong axial flow produced by an axial pressure gradient which is induced by the axial variations in the radial pressure gradient. The solution which will be utilized for the prediction of suction pressure peak, has been derived under the basic assumption that the axial flow in the core of the vortex

36

is very large in comparison with the axial velocity far away from the center of the vortex. Also, the radial flow is included in the representation of the vortex core flow. The equations which result are nonlinear and lead to a two-point boundary value problem. A brief description of equations is given in the following paragraphs.

The equations of motion (the Navier-Stokes equations) written in terms of the cylindrical coordinates x, r, θ with corresponding velocity components u, v, w and under the usual boundary layer approximations are:

$$u\, \partial u/\partial x + v\, \partial u/\partial r = -\, 1/\rho\, \partial p/\partial x + \nu_t/r\, \partial/\partial r\, (r\, \partial u/\partial r) \tag{26}$$

$$-\, w^2/r = -\, 1/\rho\, \partial p/\partial r \tag{27}$$

$$u\, \partial w/\partial x + v\, \partial w/\partial r + vw/r = \nu_t\, \partial/\partial r\, (1/r\, \partial/\partial r\, (rw)) \tag{28}$$

$$\partial(ur)/\partial x + \partial(vr)/\partial r = 0 \tag{29}$$

In the above equations ν_t corresponds to the kinematic turbulent eddy viscosity. Upon making the following substitutions

$$k = rw \tag{30}$$
$$h = rv \tag{31}$$
$$y = r^2/2 \tag{32}$$

in Equations (26) through (29) and upon defining a stream function ψ such that

$$h = \partial\psi/\partial x \tag{33}$$
$$u = \partial\psi/\partial y \tag{34}$$

37

with $\psi = \nu_t x F (\eta)$ (35)

where $\eta = \dfrac{K_\infty^2}{\nu_t^2} \dfrac{y}{x^2}$ (36)

and also letting

$K = K_\infty G (\eta)$ (37)

$\dfrac{p}{\rho} = \dfrac{K_\infty^4}{\nu_t^2 x^2} K (\eta)$ (38)

the equations of motion are reduced to the following set of ordinary differential equations:

$FF'' - F'^2 = 2 (K + \eta K') + 2 \dfrac{d}{d\eta} (\eta F'')$ (39)

$\dfrac{G^2}{4\eta^2} = K'$ (40)

$- FG' = 2\eta G''$ (41)

The corresponding set of boundary conditions are:

$G = 0, F = 0 \quad$ at $\eta = 0$ (42)

$G \to 1, F' \to 0, K\eta \to -1/4$ (43)

Equations (39) through (43) indicate that a self-similar solution of Equation (26) through (29) can be obtained in terms of a similarity variable η as defined by Equation (36). Physically K_∞ is the value of the circulation of the vortex divided by 2π.

The details of the numerical solution of Equations (39) through (41) with the boundary conditions given by Equations (42) and (43) are described in Reference 12 and will not be repeated herein. The solution involves the specification of a parametric constant $\overline{C}$ the value of which may vary

38

from 0 to - 1/2. The radial distribution of circumferential velocity is such that the vortex consists of a core near the center resembling a solid body rotation, but outside the core the circumferential velocity varies asymptotically as $1/r$, that is, similar to a potential vortex. The maximum circumferential velocity is given by

$$w_{max} = C_w \frac{K_\infty^2}{\nu_t x} \qquad (44)$$

and the core radius is defined as

$$r_c = C_r \frac{\nu_t x}{K_\infty} \qquad (45)$$

Here C_w and C_r are constants depending on the parameter $\bar{C}$ mentioned earlier. For example when $\bar{C} = - 1/2$, $C_w = 0.16$ and $C_r = 4.2$. The radial flow behaves as a sink, entraining fluid which is then jetted out at the core in the form of the axial flow. The maximum axial velocity for $\bar{C} = - 1/2$ is defined by

$$U_{max} = C_u \frac{K_\infty^2}{\nu_t x} \qquad (46)$$

at the center of the core of the vortex. It can be seen from Equation (46) that the axial velocity becomes smaller as x increases. This indicates that after some downstream distance the axial velocity will no longer be very large when compared to free stream velocity and therefore, at that stage the vortex should be represented by a different mathematical model such as that of Batchelor, Reference 9. Also, it should be noted from Equation (45) that the turbulent core is conical as indicated by the flow visualization of the leading edge vortex presented in Reference 11.

39

4.3. Application of the Self-similar Solution to Represent the Leading Edge Vortex

The self-similar solution described as needed in the previous section can be utilized for the prediction of incremental suction peaks in the vicinity of leading edge vortices generated by highly swept low aspect ratio wings at moderate to high angle of attack. For the present application it will be assumed that the leading edge vortex during its formation has radial, swirl, and axial flow characteristics as described in the previous section. This solution may be described analytically as

$$v_\phi = (W_{max}) \frac{k_1}{d'} (1 - K_2 e^{-K_3 d'^2}) \text{ for } d' > 0 \tag{47}$$

$$v_a = (W_{max}) K_4 e^{-K_5 d'} \text{ for } d' > 0 \tag{48}$$

where

$$d' = \frac{d}{r_c} \tag{49}$$

Equations (47) and (48) describe the swirl velocity and axial velocity components of the vortex at any radial distance d from the center of the vortex when d is greater than r_c. Here r_c is the core radius as described by Equation (45). Also (W_{max}) is the maximum swirl velocity given by Equation (44). K_1, K_2, K_3, K_4, and K_5 are constants obtained by curve fitting the numerical solution of Equations (39) through (41).

By placing two identical vortices, whose flow characteristics are represented by Equations (47) and (48), adjacent to a lifting surface, one above and its image below the wing at equal distances, the no flow boundary condition

40

through the airfoil surface is identically satisfied. It is assumed that the distance d is greater than the viscous core radius r_c. Since most viscous effects are confined within the core of the vortex, the vortex flow characteristics outside of the core are assumed to be similar to that of potential vortex. Due to the image vortex, the tangential and axial velocity components in the image plane (wing surface) are doubled and the suction field is intensified by a factor of four compared to the isolated vortex. Thus, the incremental static pressure coefficient created by the wing vortex interaction on the surface for $d > r_c$ may be defined as

$$\Delta C_{pv} = \frac{4}{U_0^2} \ (v_\phi^2 + v_a^2) \tag{50}$$

Here the effects of the swirl flow and axial flow have been combined and Bernoulli's Law has been utilized. Also, the increment of suction pressure has been nondimensionalized with respect to $1/2 \ \rho \ U_0^2$. Substitutions of Equations (47) and (48) into (50) results in the following relationship

$$\Delta C_{pv} = 4 \ (\frac{W_{max}}{U_0})^2 \ \left[K_4^2 e^{-2K_5 d'} + \frac{K_1^2}{d'} \ (1 - K_2 e^{-K_3 d'^2})^2 \right] \tag{51}$$

Equation (51) in combination with Equations (44), (45), and (49) describe, in general, the incremental suction peaks due to the vortices at any point on the wing surface, with d being the radial distance of the point from the axis of the vortex.

4.3.1. Empiricity of the Method

The prediction of the incremental suction peaks by application of Equation (51) is semi-empirical due to the fact

41

that turbulent kinematic viscosity ν_t and the parameter constant $\overline{C}$ have to be established empirically at the present time. The other parameter, circulation K_∞, is obtained analytically by application of Helmholtz vorticity theorem and a simple roll up theory. The distance d is known once the force free position of the vortex is established.

Under the assumption of a constant eddy viscosity in the core of the vortex, ν_t has been shown to be a function of Reynolds number $2\pi K_\infty/\nu$ where ν is the kinematic viscosity of the air. Based upon the experimentally obtained results from various sources as given in Reference 13, an empirical expression has been developed for the eddy viscosity ν_t. If the Reynolds number R_N is defined as

$$R_N = \frac{2\pi K_\infty}{\nu} \tag{52}$$

and the kinematic eddy viscosity parameter α as

$$\alpha = \frac{\nu_t}{2\pi K_\infty} \tag{53}$$

then for Reynolds numbers R_N between 10^3 and 5×10^5, the parameter α is given by

$$\alpha = 10^{-3} \frac{197}{\sqrt{R_N}} + .6 \tag{54}$$

For R_N outside the range mentioned above, α has to be obtained from some other source. For example, Reference 13 also gives a value of $\alpha = 0.2 \times 10^{-3}$ for very large Reynolds number ($> 10^7$). It is believed that this value of α may be utilized for full scale wings with vortices of large magnitude.

42

The value of parameter $\bar{C}$ depends on the shape of the leading edge. As mentioned in an earlier section, the value of $\bar{C}$ varies between 0 to -0.5. Physically, $\bar{C}$ equal to -0.5 corresponds to a smooth formation of leading edge vortex with drag associated with it being a minimum. A vortex from a sharp leading edge should correspond to a value of $\bar{C}$ which is greater than -0.5 such as -0.3. A larger value of $\bar{C}$ (e.g., $-.3$) results in greater axial velocity at the center of the vortex and consequently corresponds to a vortex with higher drag associated with it. This vortex also has higher values of the maximum swirl velocity. For the present application the formation of the vortex has been assumed to be smooth and, therefore $\bar{C}$ has been taken to be equal to -0.5. For this value of $\bar{C}$, C_W is equal to 0.16 in Equation (44) and C_r is equal to 4.2 in Equation (45). Also substitution of the definition in Equation (53) into Equation (44) and (45), gives

$$\frac{r_c}{x} = 24.6 \, \alpha \tag{55}$$

and

$$W_{max} = .02545 \, \frac{K_\infty}{\alpha x} \tag{56}$$

Here x is measured along the axis of the vortex. Equation (51) reduces to the following expression after substitution of the constants K_1, K_2, K_3, K_4, and K_5:

$$\Delta C_{pv} = 4 \, \left(\frac{W_{max}}{U_0}\right)^2 \, F \, (d/r_c) \tag{57}$$

with

$$F(d') = 8.058e^{-1.320d'} + \frac{2.3}{d'} (1 - .741e^{-.882d'^2})^2 \tag{58}$$

Equations (54) through (58) are sufficient for the complete determination of incremental suction peaks ΔC_{pv} after the

43

circulation K_∞ and the distance d of the vortex from the wing have been computed.

4.4. Determination of Vortex Breakdown

The self-similar solution representing the upstream portion of the leading edge vortex indicates (Equation (46)) that the maximum axial velocity becomes smaller at downstream stations, that is as x increases. Therefore, it seems obvious that after some distance downstream, say at x equal to x_t, the flow described here must evolve into some different flow such as that flow described by Batchelor. Batchelor's solution is based on the assumption that the axial velocity in the core region is small in comparison with the free stream velocity. It is obvious that this assumption is clearly valid for some downstream stations of the leading edge vortex. One of the main differences between the two flows is in regards to the variation of the viscous core radius r_c with the downstream distance x. At upstream stations $(x < x_t)$ r_c increase linearly with x Equation (55), while at downstream stations $(x > x_t)$ r_c varies approximately as the square root of the distance, say $(x - x_t)^{1/2}$. Also, the core velocity continues to decrease, keeping the flow of volume flux in the core approximately constant, until the vortex bursts.

The criterion, for the determination of vortex breakdown, that has been utilized in the present analysis is based on the theory of finite transition as given by Benjamin (Reference 14). In this theory of finite transition, the breakdown is thought of as a process similar to the hydraulic jump or a shock wave. Using the hydraulic jump analogy, the theory explains the vortex-breakdown phenomenon as a transition between two steady states of axisymmetric swirling flow. The state upstream from the breakdown is assumed to be supercritical and conservation equations for mass, axial momentum and angular momentum are applied to relate the flow conditions

45

upstream and downstream of the transition. Barcilon (Reference 15) has worked out the details of a simple case of a vortex having a core rotating as a solid body surrounded by potential flow and having uniform axial velocity in the core. The result indicates the existence of critical velocity u_c which is analogous to the velocity of sound in a compressible flow. Barcilon defines this critical velocity as

$$u_c = \frac{\pi K_\infty^2}{2Q} \tag{59}$$

with Q being the volume flux in the core. It is noted that transition can occur only from a velocity higher than the critical (supercritical) velocity u_c to one that is lower.

For the present application the leading edge vortex has been assumed to have burst when the average axial velocity in the core of the vortex reaches u_c as given by Equation (59). At stations downstream of the point of vortex breakdown, the incremental suction peaks are taken to be zero.

46

4.5. Determination of the Force-Free Positions of the Vortices

For the computation of the correct pressure distribution over the lifting surface in the presence of vortices, it is essential that the *force-free positions of the vortices* be determined. In the present analysis, control points are described along the length of each of the vortices. At each of these control points the following components of velocities are computed:

    a. the velocity components induced by the surface doublet distribution of the lifting surface,

    b. the self-induced velocities due to vortex curvature and the velocities induced by the other free vortices,

    c. the free-stream velocity component, and

    d. the axial velocity in the vortex core.

Since a force-free vortex allows for only the flow along its axis, the vortex is considered stationary when this condition is satisfied. It is obvious that since these above velocity components are dependent upon the unknowns being solved for, the force-free position of the vortices must be determined in an iterative manner. A complete description of this iterative procedure is presented in a later section.

47

4.6. <u>Determination of the Regions of Separated Flow</u>

At moderate to high angles of attack, the flow over the surface of a low aspect ratio swept wing is very complex and may be described by a mixture of potential and separated flow regions. The separation and/or reattachment are highly influenced by the character of the boundary layer, such as laminar boundary layer or turbulent boundary layer. Several methods have been developed for the calculation of three-dimensional boundary layers over swept wings. These methods are semi-empirical as regards to the specification of shear stresses and the initial conditions. These methods are very successful in predicting separation at low angles of attack but the procedures breakdown in case of wings at high angles of attack.

A simple criterion for the prediction of the sep-arated flow regions was utilized in the earlier work (Reference 21) and reasonable results were obtained. Specifically, the procedure, for determining whether at any point on the wing separation had occurred, or not, involved a comparison of the net aerodynamic angle of attack (the geometric angle of attack minus the induced angle) versus an empirically defined angle above which the section was assumed to be stalled. The evaluation as to whether or not separation had occurred or not was conducted on an element-by-element basis so that at various geometric angles of attack, the lifting surface had different regions of separated flow.

Since in the present analysis, the slope of the surface of the airfoil (Equation (13)) is included, an improvement was obtained in the determination of the fully separated flow regions based on the same separation criterion as used in Reference (2). Here the aerodynamic angle corresponds to the

48

local geometric angle of attack of the surface element with respect to flow minus the induced angle. Also, it may be noted that since the upper and lower surfaces of the wing are treated independently, the flow is always attached (potential) on the lower surface, while the upper surface has a mixture of potential-separated flow regions. This representation of both airfoil surfaces eliminated the necessity of the use of an empirical cross-flow coefficient to compute the lift on the separated element as was done in Reference (2).

4.7. Iterative Procedure Utilized for Solution of Equation of Motion

As previously discussed, the problem of determining the aerodynamic loads on a lifting surface at high angles of attack is highly nonlinear in nature. It is obvious, therefore, that the solution must be determined in an iterative manner. The iterative calculation procedure that is utilized to obtain the desired solution is presented below:

Step a - The doublet strengths over the lifting surface are calculated at low or moderate angle of attack, when it can be assumed that the flow is fully attached or potential on both the lower and upper surfaces. Also, no free concentrated vortices such as leading edge vortices, tip vortex, etc. are included in this initial computation. This step and the next two steps may be skipped if the approximate strength and locations of the concentrated vortices are known for the configuration under consideration.

Step b - The initial path of the various vortices such as strake vortex, leading edge vortex, tip vortex, etc. is estimated approximately from the distribution of the doublet strength along the edges of the lifting surface as computed in Step a. The subsequent path of these vortices in space is assumed here. As an example, doublet strength distribution along the leading edge is examined. The point along the edge where the peak of this distribution occurs, corresponds approximately to the location where the leading edge vortex starts moving away from the edge in the downstream direction. Also, generally, this point of origin of the vortex moves inboard as the angle of attack is increased. An analogous procedure is followed for the other vortices.

Step c - Knowing the approximate locations of the concentrated vortices (their strengths are unknown at this stage), the influence coefficients of all the control points with

50

respect to boxes along the edges are altered appropriately by including the effect of all the free vortices. More specifically, the strengths of the various segments of the free vortices are related to the differences of doublet strengths of some of the boxes along the edges of the lifting surface. This procedure is identical to the one used for the inclusion of the wake at the trailing edge. Utilizing these modified influence coefficients, the distribution of doublet strength over the lifting surface is computed for the given angle of attack. As a result of this calculation, the approximate strengths of all the vortices are known for the prescribed locations of the free vortices.

Step d - Since an estimate of strengths and locations of the vortices has been obtained, the effect of flow separation on the upper surface is computed in the next step. The criterion followed for the determination of separated flow regions is as previously described.

Step e - Based on the computed strengths of the vortices, doublet distribution on the lifting surface, free stream components, etc., the total velocity vector at each element of each free vortex is computed.

Step f - The difference in the orientation of the velocity vector with respect to the axis of each free vortex is determined and the vortex location moved so that this difference is less than some specified value.

Step g - Steps c, d, e, and f are repeated until converged locations and strengths of vortices have been obtained.

Step h - On the basis of converged solution obtained in Step g the pressure coefficients on the lifting surface are computed as per procedure previously described. Also, the incremental suction peaks in the vicinity of vortices are computed. Finally, the pressure distribution on the lifting surface is appropriately integrated to obtain the overall aerodynamic lift.

4.8. Application of the Analysis

The analysis formulated in the previous sections was utilized to develop a computer program for the prediction of the aerodynamic loads on a lifting surface. The basic assumptions of any nonlinear lifting surface theory are also inherent in the present program. Some additional assumptions and limitations involved in the present program are noted below:

a. The general solution of equations describing the formation of vortices at the leading edges is not incorporated in the program at this stage. Only the solution corresponding to the value of parameter $\bar{C}$ being equal to -1/2 is included in the program. This assumes that the formation of the vortices is along a relatively smooth rounded edge. For general applicability, the solution of equations described in the previous sections should be included in the present program for all possible values of the parameter $\bar{C}$ ($-1/2 < \bar{C} < 0$).

b. Some of the parameters for the representation of vortices such as value of kinematic turbulent viscosity ν_t in the core, the initial value of x in Equation (43), the value of parameter $\bar{C}$, etc., have to be established empirically.

c. The variation of ν_t with Reynolds number is yet to be established for a full range of Reynolds numbers. The relationship described by Equation (52) is utilized in the present program. This relationship is valid only for the values of Reynolds number between 10^3 and 5×10^5. Moreover the variation of ν_t with Reynolds number as given by Equation (52) was derived from the data of wing tip vortices. Even though the qualitative variation of ν_t with Reynolds number seems to be correct, the quantitative variation of ν_t with Reynolds number is yet to be verified.

52

d. The primary unknowns of the problem such as circulation strengths and spatial positions of vortices, regions of separated flow, etc., are determined in an iterative manner which may result in a limitation of the accuracy of the solution.

e. Even though the force free positions of all the vortices can be established in an iterative manner by the program, the initial approximate spacial location of all the vortices has to be specified beforehand. This may be very cumbersome in some cases.

While the above might be considered to be limitations of the analysis, they really indicate parameters whose values will be better defined when the program has been used more extensively than it has been to date.

53

5. DISCUSSION OF RESULTS

Since there were two distinct parts to the research effort during this contract, tests of wing tail configurations and modifications and extension of the theoretical predictive method, the discussion of the results that were obtained from each invidiaual part will be discussed separately.

5.1. Experimental Tests of Wing Tail Configurations

Since, because of the lateral and longitudinal offset of the horizontal tail (Figure 7), the wing would be in different locations in the wind tunnel, it was necessary to measure the basic aerodynamic characteristics of the various wing configurations prior to conducting the tests of the wing tail configurations. The results of these tests, and a comparison of these results with those obtained with the wing pivoted about the tunnel centerline, are presented in Figures 9 through 14. While it can be seen from the data presented in Figure 9 that the lift coefficient was not altered by the location of the basic wing in the wind tunnel, it was for the wing strake configuration, at angles of attack above 26 degrees (Figure 10). It is believed that the reason for the noted differences between the data from the previous tests and those obtained during the present series is due to slight extension of the strake into the converging section of the tunnel as the angle of attack became large. The slight flow misalignment caused by this would cause the strake vortex formation to be affected and thus change the relationship between the strake and leading edge vortex over the wing surface. While this effect reduced the maximum lift coefficient that could be obtained due to wing vortex interaction, it is not believed that the basic flow mechanism under study was altered.

54

The reduction in the drag coefficient noted at high angles of attack for the wing strake configuration (Figure 12) would be expected due to the reduction of the lift in this angle of attack region (Figure 10). Since the lift coefficient was not altered for the basic wing, it was not surprising that the drag coefficient was not altered for those same configurations.

The pitching moment coefficient about the aerodynamic center for the basic wing in the various locations in the tunnel is presented in Figure 13. From the data presented in this figure it can be seen that except for configuration 1-60-09-A all of the pitching moment data agreed very well with that previously obtained with the wing when it was pivoted about the centerline of the tunnel. The data obtained for configuration 1-60-09-A indicates that the leading edge vortex formed earlier and was stronger than that of the other configurations. At high angles of attack, since the flow is almost all separated, the pitching moment coefficient for all configurations would be expected to be the same. The reason for the unique behavior of configuration 1-60-09-A was not determined as this configuration was not utilized further in the investigations that were conducted.

The pitching moment coefficients for the wing strake configurations are compared with those obtained during a previous test with the wing pivoted about the centerline of the tunnel in Figure 14. At first glance there seems to be a considerable amount of scatter in the data. While it is recognized there is scatter, the absolute magnitude of the scatter in C_M is only on the order of ±0.01 which is approximately 1/15 of the maximum value of the C_M measured for the basic wing configurations. It is believed that the reason for this

scatter is two-fold, first, the pitching moments are relatively small and thus difficult to measure accurately and secondly, since the pitching moments are transferred from the balance point to the mean aerodynamic center of the wing, small measurement errors in the drag and lift all contribute to the small differences in the pitching moment that is plotted. Even though there is scatter in the data, all of the configurations, regardless of their position in the tunnel, exhibited the same kind of pitching moment with angle of attack particularly in the angle of attack region of 28 degrees where the pitching moment suddenly changes from a stabilizing to a destabilizing value.

On the basis of these preliminary tests, it was concluded that while there were some effects on the aerodynamic characteristics of the lifting surfaces due to its location in the tunnel, they were not of a magnitude to sufficiently affect the results of the test program.

To determine the effect of the wing wake on the tail effectiveness, tests were conducted for the various configurations to determine for various wing angles of attack, the pitch angle of the tail at which the pitching moment of the wing-tail configuration went to zero. In addition, the effectiveness of the tail surface in generating pitching moment about the wing MAC was also determined by varying the tail angle of attack about its trim value. The results of these tests are presented and discussed below.

Figure 15 presents the results of the tests conducted with configuration 1-75-06B which is the basic wing configuration (without strake). This configuration produced an increasing nose down pitching moment with increasing angle of attack similar to those configurations for which data was presented in Figure 13. As can be seen from the

56

data presented in Figure 15, the pitching moment generated about the wing MAC by the tail surface, as its angle of attack was altered, was surprisingly linear regardless of the angle of attack of the main wing. The slope of the pitching moment curve with tail angle of attack $dC_M/d\alpha_T$ provides a measure of the effectiveness of the tail and the results presented in Figure 15 indicated that while there is some loss in tail effectiveness as the wing angle of attack is increased from 15 to 30 degrees, it is only on the order of 25%, which is much less than might be expected.

The variation of the tail angle of attack (relative to the wing mean chord) with increasing wing angle of attack, shown in Figure 15, indicates that above a wing angle of attack of 20 degrees very large changes in the tail geometric angle of attack are required to maintain aircraft trim. In investigating the reasons for this apparent large change in angle of attach of the tail surface, the system forces and moments were inspected in detail as well as the tail pressure distributions. Figure 16 presents a sketch of the directions of the force and moments as well as the relative geometric orientations of the lifting surfaces at a moderate angle of attack. As is shown in this figure for configuration 1-75-06B, the wing generates a nose down pitching moment about its MAC, and the drag force on the tail produces an opposing nose up pitching moment about the wing MAC. In order to provide moment trip about the wing MAC the tail must then develop a lift force in the direction shown. Since at lower angles of attack of the wing, the tail drag moment and the wing pitching moment tend to oppose each other, the lift developed by the tail would tend to be small. The pressure distributions presented in Figure 17 for the tail when the configuration is in trim for a wing angle of attack of 8.7 degrees, indicates that indeed the tail lift force is small.

57

As the angle of attack of the wing is increased, Figure 16, the MAC of the tail surface will, with respect to the free stream direction, be located such that its drag force will create a nose down instead of a nose up pitching moment about the wing MAC. For configuration 1-75-06B this shift occurs at a wing angle of attack of 11.3 degrees. At wing angles of attack of between 12 and 20 degrees the pitching moment of the wing does not increase very much due to the formation of the leading edge vortex in this angle of attack range (Figure 13). It would be anticipated therefore that the tail angle of attack to maintain pitching moment trim in this angle of attack range would therefore not have to be changed significantly. The data presented in Figure 15 indicates that the tail angle of attack with respect to the wing chord plane does not change much although the tail geometric angle of attack with respect to the free stream changes from approximately +3 degrees to +12. The only manner by which this could be accomplished is that the induced effect of the wing wake on the tail surface is very strong and increases with every angle of attack such that the tail surface has a small effective negative angle of attack.

As the wing angle of attack is increased above 20 degrees, the wing nose down pitching moment increases and the pitching moment of the tail drag force increases the pitching moment about the wing MAC. Since the lift of the tail must be increased to counter the nose down pitching moment, the induced drag of the tail increases and thus its effect on the nose down pitching moment is also increased. Thus, as the angle of attack of the wing increases, the drag moment arm of the tail increases negatively and the moments generated about the wing MAC by the tail lift and drag force tend to offset each other. Since the lift force increases more rapidly than the drag force with increasing angle of attack,

58

trim balances can be obtained but the angle of attack of the
tail surface must undergo a larger change to maintain trim
than is required when the tail drag is generating a pitching
moment about the wing MAC in the same direction as the tail
lift force.

Comparison of the tail pressure distribution pre-
sented in Figure 18 with those presented in Figure 17 shows
that the tail surface is indeed, developing more lift at the
higher wing angles of attack.

When the strake is added to the leading edge, con-
figuration 2-75-06B, the pitching moment characteristics are
different than the basic wing (Figure 14) but the average
tail effectiveness as a function of wing angle of attack is
not changed to any great degree (Figure 19). It is noted,
however, that the data presented in Figure 19 indicates there
is a noticeable variation in the tail effectiveness as a
function of angle of attack. This variation seems to corre-
late with the radical changes in the tail geometric trim
angle α_t with respect to the chordplane of the main wing. On
the basis of the analysis of the wing-tail pitching moment
characteristics of the basic wing configuration previously
presented and because the pitching moment of the wing strake
configuration in the angle of attack range $0 \leq \alpha_w \leq 20$
degrees is of the order of one half that of the basic wing,
it might be expected that the variation of the tail trim
angle might be similar, instead of radically different, for
both configurations. Inspection of the pressure distribution
for the wing strake - tail configuration shows why there is
a sufficient difference in the behavior of the tail trim angle
variation between the two configurations. Figure 20 presents
the pressure distribution on the tail surface when the wing

59

tail configuration is in trim at 13.1 degrees. As can be noted from the pressure distribution, while there is some net lift, there is an obvious vortex interaction in the tail surface at approximately the 70% span. It is believed that this reversal of the pressure distribution in the tip region is caused by the induced effect of the strake vortex crossing the tail around 65% of its semispan. It is apparent that the induced effect of this vortex is sufficiently strong to reverse the angle of attack in the tip region and thus change the sign of the lift force developed by the tail in the region. This belief is strengthened by the pressure distribution presented in Figure 21 which was obtained on the tail at an angle of attack 4 degrees less than that presented in Figure 20. While the induced effect of the strake vortex of the wing significantly reduces the lift over the tip region of the tail, the lift over the entire span is now all in the same direction. This type of change in the pressure distributions due to a change in the tail angle of attack is what might be expected.

At a wing angle of attack of 17.4 degrees, the pressure distributions over the tail surface at the trim angle of attack are basically the same as they were for a wing angle of attack of 13.1 degrees. These pressure distributions, presented in Figure 22, indicate that while the lift produced by the tail is greater, the increased strength of the strake vortex from upstream still causes a load reversal near the tip. However, under the influence of leading edge vortex, the strake vortex moves outboard and crosses the tail around 75% of its semispan.

As the angle of attack is decreased by 4 and then 8 degrees, Figures 23 and 24 respectively, the increased lift of the tail surface moves the lift reversal outward. This outward shift of the lift reversal is what might be expected if it is caused by the induced effect of a strong free vortex such as that generated by the strake.

60

At a wing angle of attack of 21.7 degrees, no evidence of induced effects from a concentrated vortex could be found in the pressure distributions over the tail. This can be explained as follows. The strake vortex, under the influence of strong leading edge vortex generated by the wing, moves farther outboard and is located outboard of the tail tip. Therefore, the reversal of the pressure distribution near the tip, as was found at lower angles of attack, was not present. This is also true for wing angle of attack of 30.3 degrees where the strake vortex is swept further outboard into the leading edge vortex due to its strong induced effect (Reference 2). As the wing angle of attack is increased above 21.7 degrees, a tail trim angle of attack trend similar to that obtained with the basic wing is obtained except that the maximum change in trim angle is only 5 degrees instead of 16 degrees as it was for configuration 1-75-06B. This much smaller tail trim angle variation is attributed to the fact, that for the wing strake configuration at high angles of attack, the pitching moment developed by the tail drag and lift are working together to counter the wing pitching moment instead of working against each other as they were for the basic wing tail configuration.

It is interesting to note, that at a wing strake angle of attack of 30.3 degrees, the tail is at a geometric angle of attack of 27 degrees with respect to the airstream when trim is obtained. Since the lift force developed by the tail surface is relatively small as shown by the pressure distributions presented in Figure 25, it indicates that the flow angularity induced by the wing wake is of the order of 25 degrees which corresponds to a mean induced velocity from the wing wake of 47 feet per second. It is obvious that this significant induced velocity cannot be ignored when considering the design of a tail operating in the wake of a lifting

61

surface generating strong leading edge and strake vortex
flows. In comparison, the wake induced effect was estimated
to be of the order of 17 feet per second for the basic wing
which is approximately 1/3 of the wing strake configuration.

The tail effectiveness data obtained for configura-
tion 1-75-12B is presented in Figure 26. This data when com-
pared to the data presented in Figure 15 shows the effect of
moving the tail chordplane higher up from the wing chordplane.
It can be seen that the results are very similar for the two
configurations except that for Conf. 1-75-12B, there is a
sharp drop in the tail effectiveness as the wing angle is in-
creased from 25.6 degrees to 29.6 degrees. It is also noted
that the accompanying change in the tail trim angle is not as
large as it was for Conf. 1-75-06B. It is believed that the
reason the tail trim angle does not vary as much as it did for
Conf. 1-75-06B in this angle of attack range, is that the angle
of attack at which the moment generated by the tail drag force
about the wing MAC opposes the moment due to tail lift (Fig. 16)
is approximately 23 degrees instead of approximately 11 degrees
as it was for Conf. 1-75-06B. Therefore, the tail lift force
is much more effective for Conf. 1-75-12B to obtain trim than
it was for Conf. 1-75-06B.

It is reasoned that the sharp drop in the tail ef-
fectiveness as the wing angle is increased from 26 to approxi-
mately 30 degrees is due to the induced effects of the diffused
leading edge vortex that separated from the wing. Comparison
of the pressure distributions presented for the tail surface at
trim for wing angles of attack of 25.6 and 29.6 degrees re-
spectively indicates that the induced effect of the wing wake
flow significantly reduced the lift over the outboard section
of the tail surface which would reduce the effectiveness of the
tail. Comparison of the tail effectiveness data presented in
Figure 29 for Conf. 2-75-12B with that presented in Figure 19
shows the effect of doubling the distance of the

62

tail surface from the wing chordplane for the wing strake configuration. It can be seen from a comparison of this data that while the tail effectiveness has a slightly different trend, the trend of the tail geometric trim angle with wing angle of attack is significantly different. It is believed that this significantly different trend is due to the different orientation of the wing wake with respect to the tail plane. At 21.5 degrees wing angle of attack, the small positive pitching moment generated by the wing (Figure 14) is countered by the lift moment generated by the tail surface and therefore the lift required to be generated by the tail surface would be small. The pressure distribution presented in Figure 30 tend to confirm this reasoning. As the wing angle of attack is increased the sudden jump in the positive pitching moment generated by the separation of the leading edge vortex makes a demand for a much greater lift from the tail surface. The pressure distributions presented in Figure 31 indicate, however, that the wing vortex system has a strong induced effect on the tail at this location and tends to destroy the effectiveness of the tail surface thus requiring a significant angle of attack adjustment.

The effect of moving the tail surface closer to the wing trailing edge on the tail effectiveness for the wing and wing strake configurations is shown in Figures 32 and 33, respectively. When this data is compared to that obtained for configurations 1-75-06B and 2-75-06B, respectively, it can be seen that the results and the trend of the results with the wing angle of attack are very similar. The pressure distributions obtained for configuration 2-60-03B also exhibit the same type of tail vortex interaction as shown for configuration 2-75-06B which also explains the rapidly varying angle of attack, with wing angle for this configuration. It is

63

believed that the somewhat more consistent tail effectiveness value obtained for these configurations can be related to the stronger tail drag pitching moment component since the change in the sign of this component occurs at the relatively small wing angle of attack of approximately 7 degrees.

Figures 34 and 35 present the effect of the tail on the lift of the wing strake and the basic wing configurations. It can be seen from the data presented that the effect of adding the tail did not significantly effect the total system lift of the wing strake configuration. However, since the tail lift required to obtain pitching moment trim was in a direction opposite to the wing lift for the basic wing configuration (1-60-03A), a significant reduction in the configuration lift was obtained when the tail was added. While data was not obtained for the wing strake configuration having the tail closer to the wing trailing edge, it might be conjectured that since the pitching moment developed by the wing is positive instead of negative, that the tail surface might increase the lift of this configuration in trim flight.

64

5.2. Theoretical - Experimental Correlation

The computer program that was developed was exercised to predict the pressure distributions and the total integrated lift for the basic wing at 13.1 and 21.6 degrees angles of attack and for the wing strake configuration (Configuration 3A) at angles of attack of 21.6 degrees and 27.7 degrees. For these cases, the experimental data against which the predictive results compared is available in Reference 1. For most of the computations, the upper surface of the wing was represented by 104 quadrilateral elemental surfaces with thirteen control points along the chord at each of eight spanwise stations. The lower surface was divided into a total of 72 boxes with nine chordwise and eight spanwise control points. The free vortices such as the strake vortex, leading edge vortex, etc., were represented by up to 30 segments. The effects of airfoil thickness and curvature were accounted for in the present computations where the chordwise slopes of the surface (dz/dx) were obtained from the analytical expression describing the geometric characteristics of NACA0006 airfoil. The effects of the spanwise slope (dy/dx) were not included in the present computations. For all computations the stall angle of the surface segments was assumed to be 20 degrees.

The computations conducted on the basic wing configuration determined the pressure distributions on the upper and lower surfaces at the angle of attack 13.1 degrees. The pressure distributions were calculated under the assumption of fully attached flow and the weak leading edge vortex which exists for this wing at this angle of attack was not included. These computations were carried out to check the correctness of the linear (potential flow) analysis. Some of the results

65

of the computations are shown in Figure 36. As illustrated
in Figure 36, the results obtained indicate a good correla-
tion between theory and experiment except near the trailing
edge. This is believed due to the fact that the distance be-
tween the upper and lower surfaces near the trailing edge is
very small which results in numerical errors. Some degree of
success in eliminating this problem was achieved by altering
the wake representation near the trailing edge and by increas-
ing the number of control points in the same regions. At
high angles of attack, the flow near the trailing edge of
the upper surface is separated from the wing and, therefore,
numerical errors were not encountered when the computations
are carried out at high angles of attack. It should be noted
that the comparisons between the theory and experiment, pre-
sented in Figure 36 have been presented at an inboard station
(approximately at 15% span) where the influence of the weak
leading edge vortex is negligible. The leading edge vortex
at 13.1 degrees angle of attack is very weak and, therefore,
does not contribute significantly to the integrated lifting
characteristics of the wing. However, it can alter the local
pressure distributions at the outboard spanwise location.

On an integrated lift basis, the overall value of
the lift coefficient C_L that was predicted for this configu-
ration was 0.65 which compares very well with a measured
value of 0.68.

As the angle of attack is increased, the leading
edge vortex becomes more concentrated, and its suction effect
becomes more predominant. For the basic wing shown in Figure
2 at angle of attack 21.6 degrees the vortex geometry of the
leading edge vortex and tip vortex for a wing angle of attack

66

5.2. Theoretical - Experimental Correlation

The computer program that was developed was exer-
cised to predict the pressure distributions and the total
integrated lift for the basic wing at 13.1 and 21.6 degrees
angles of attack and for the wing strake configuration (Con-
figuration 3A) at angles of attack of 21.6 degrees and 27.7
degrees. For these cases, the experimental data against
which the predictive results compared is available in Ref-
erence 1. For most of the computations, the upper surface
of the wing was represented by 104 quadrilateral elemental
surfaces with thirteen control points along the chord at
each of eight spanwise stations. The lower surface was di-
vided into a total of 72 boxes with nine chordwise and eight
spanwise control points. The free vortices such as the
strake vortex, leading edge vortex, etc., were represented
by up to 30 segments. The effects of airfoil thickness and
curvature were accounted for in the present computations where
the chordwise slopes of the surface (dz/dx) were obtained
from the analytical expression describing the geometric char-
acteristics of NACA0006 airfoil. The effects of the spanwise
slope (dy/dx) were not included in the present computations.
For all computations the stall angle of the surface segments
was assumed to be 20 degrees.

The computations conducted on the basic wing configu-
ration determined the pressure distributions on the upper
and lower surfaces at the angle of attack 13.1 degrees. The
pressure distributions were calculated under the assumption
of fully attached flow and the weak leading edge vortex which
exists for this wing at this angle of attack was not included.
These computations were carried out to check the correctness
of the linear (potential flow) analysis. Some of the results

65

of 21.6 degrees is shown in Figure 37. A comparison of the
measured and predicted surface pressure distributions are
presented in Figures 38a through 38d.

Comparing the measured and predicted spanwise pres-
sure distributions along constant chordlines in Figures 38a
through 38d, it can be seen that the spanwise variation of
the pressures are reasonably well predicted. In the region
of the strong vortex flows, however, the correlation is not
as good as is desired. These regions are on the upper sur-
face at points immediately inboard and outboard of the lead-
ing edge vortex where the pressures predicted are generally
less than the measured pressures. It is believed that there
are two reasons for the poor correlation in this region. The
first is that it is believed that the leading edge vortex
core size is more diffuse and larger than that which is pre-
dicted which tends to concentrate the vortex suction effect
over a narrower section of the span. The second reason for
the under-prediction of the surface pressures outboard of
the vortex is believed to be due to the somewhat approximate
and crude criterion which has been utilized for the prediction
of the location of flow separation. The present analysis
predicts that the flow outboard of the leading edge vortex
is separated at 21.6 degrees angle of attack due to the up-
wash induced by the vortex in this region of the wing. In
the region outboard of the vortex the flow is highly turbulent
and separation occurs in a much more gradual manner than that
predicted by the analysis. In addition to the above noted
limitation, it must be recognized that it is difficult to
predict the pressure coefficient in separated flow regions
due to the highly complex nature of the flows. In fact, a
rigorous viscous flow analysis using Navier-Stokes equations
is necessary to determine the pressure distribution in the

67

in the separated flow regime. However for the present
purposes, an approximate but simple expression based on Ber-
noulli's equation was used to determine the pressure distri-
bution. In the separated flow region, the total pressure of
the flow is reduced due to viscosity. Denoting this reduction
by ΔH, the pressure coefficient C_{pi} in the separated flow

region can be expressed as

$$C_{pi} = 1 - \frac{V_i^2}{U_o^2} - \Delta H \tag{60}$$

where V_i is the total velocity and U_o is the free stream
velocity. The discrete vortices in the flow (surface lattice
in the attached flow and free vortices from the leading and
trailing edges) were used to determine the induced velocities
in the separated flow. Using these induced velocities, the
pressure coefficient C_{pi} in the separated flow region was
therefore assumed to be

$$C_{pi} \simeq 1 - \frac{V_i^2}{U_o^2} \tag{61}$$

where it was assumed that ΔH is small. For the present
analytical formulation, the value of the pressure coefficient
C_p in separated flow is assumed to be equal to $-\cos^2(\alpha-\theta)$.

Another region where the correlation seems to be
poor is in the tip region of the wing. It is believed that
due to the presence of the tip or a secondary vortex this
region of the wing should be unstalled. Apparently, for the
present computations, the location and strength of the tip
vortex are not predicted to a significant degree of accuracy
which results in the overprediction of C_p in the tip region
on the upper surface (Figures 38a through 38d). On the lower

68

surface the correlation between the predicted and measured
pressures is generally very good for most of the wing. Near
the tip, on the lower surface, however, the predicted pres-
sures are a bit higher than the measured values which is
believed due to the omission during the present computation
of one nonlinear term from the analytical expression of C_p

given by Equations (24) and (25). The contribution of the
spanwise gradient of doublets distribution dD/dY was con-
sidered to be negligible and was not included in the compu-
tations. This nonlinear term is definitely negligible
compared to the other terms in Equation (24) in the normal
angle of attack range. At high angles of attack, however,
the doublet distribution indicates the value of dD/dY is
significant on the lower surface in the tip region and
therefore this term should be included in the computations
of C_p in this region of the wing. Qualitatively, the results
of hand computations indicate a better correlation in the tip
region on the lower surface once this correction is applied
to the predicted results.

A comparison of the measured and predicted chord-
wise pressure distribution for the basic wing at an angle of
attack of 21.6 degrees, are presented in Figures 39a through
39c. As can be seen in the data presented, the theory pre-
dicts that the flow separates earlier over the upper surface
of the wing near the trailing edge than that which the experi-
ment indicates. At approximately 44% span, the theory also
predicts that the leading edge is stalled whereas the experi-
mental data indicates that the surface is not stalled in this
region. The possible reasons for the discrepancies between
the measured and predicted pressure distributions were dis-
cussed previously and are believed to be due to the under-
prediction of the core radius of the leading edge vortex
and the simplified separation criterion that is utilized in
the theory.

Although the pressures predicted by the analysis
do not match the experimental data well in some regions, the
overall lift coefficient C_L predicted by the program for this
configuration at an angle of attack of 21.6 degrees, is 1.03
which agrees well with the experimental values of 1.01. The
breakdown of predicted value of C_L into its various compon-
ents indicates that 0.08 of the total C_L is that due to non-
linear suction lift in the vicinity of vortices while 0.95
is due to potential lift. It is evident from the comparison
of the predicted and measured pressure distribution that for
this case, the program has slightly under-predicted the non-
linear suction lift and it has over-predicted the components
of the lift due to potential flow.

The predicted vortex geometry for wing-strake con-
figuration (3A) at an angle of attack equal to 21.6 degrees
is shown in Figure 40. Comparisons of the spanwise surface
pressure distributions predicted by the analysis and the
measured pressures for several constant chord lines are
shown in Figures 41a through 41d. While overall, the pre-
dicted pressure distributions are generally closer to the
measured values than they were for the basic wing, the pre-
dicted pressures tend to be smaller than the measured
pressures outboard of the leading edge vortex on the upper
surface. This again is believed to be due to the under-
prediction of the core radius and the simplified separation
criteria. The overall computed lift coefficient C_L for this
case is 1.03, of which 0.16 corresponds to nonlinear suction
lift due to vortices and 0.87 is due to potential flow. This
compares reasonably well with the experimental obtained value
of C_L equal to 1.09. It is believed that the discrepancy is
due to the under prediction of C_L component due to the vortex
suction pressures.

70

As the angle of attack is increased to 27.7 degrees
for the wing-strake configuration, the strake vortex moves
further outboard over the wing surface and the leading edge
vortex moves slightly inboard. The predicted vortex geometry
is shown in Figure 42 for this configuration. A comparison
between the predicted and measured spanwise surface pressures
along several constant chord lines for this wing-strake con-
figuration at an angle of attack of 27.7 degrees are shown
in Figures 43a and 43b as with the previous configurations,
outboard of the leading edge vortex the predicted spanwise
pressure distributions indicate abrupt stalling whereas the
measured distributions indicate a gradual transition into the
stalled portions of the wing.

The peak vortex suction pressures in the vicinity
of the strake vortex are somewhat lower than the measured
values. Apparently, this is because some of the characteris-
tics of the strake vortex at this angle of attack are incor-
rectly predicted. The difficulty in predicting the vortex
characteristic partly is due to the fact that the strake
vortex originated from a sharp edge of a delta shaped plate
while the present program assumes all the vortices to have
been formed from smooth edges. It is believed that a better
estimation of some of the characteristics of the strake vortex
such as the initial value of viscous core radius, etc., will
result in improved correlations. At this angle of attack, the
total predicted lift coefficient is 1.18, with 0.96 being due
to potential flow and 0.22 due to the nonlinear suction in the
vicinity of the vortices. The experimental value of C_L at
this angle of attack is 1.32. The analysis of the results for
this case indicates that the lift component corresponding to
nonlinear suction lift in the vicinity of vortices must have
been significantly under-predicted.

71

CONCLUSIONS AND RECOMMENDATIONS

On the basis of the experimental and theoretical research reported in this report, it is generally concluded that the test data demonstrated that an aircraft configuration can be stabilized with a nominal size tail surface operating in the vortex wake of the main lifting surface. In addition, it was concluded that the improved theoretical prediction technique developed, while not yielding perfect correlation with the measured surface pressure distributions, is sufficiently accurate to be used as a design tool to investigate the effects of attached vortex flows on the aerodynamic characteristics of wings having arbitrary planforms and operating at high angles of attack.

In addition to the above general conclusions, the following specific conclusions were also formulated.

(1) The trim angle of the tail surface relative to the chord plane of wing varied differently with wing angle of attack for the basic wing and the basic wing with the root leading edge strake.

(2) When the concentrated strake vortex from the main wing intersected the tail plane, large angle changes of the tail were required to maintain system trim.

(3) Even though the characteristics of the wing wake were changing significantly as its angle of attack was changed in the range of $0 \leq \alpha_w \leq 30$ degrees, the tail effectiveness, $(dC_m/d\alpha_t)$, remained relatively constant.

(4) Even though the tail surface could have a geometric angle with respect to the free stream of 24 degrees, it is estimated, on the basis of the tail pressure distributions, that because of the strong induced effect of the wing wake

72

that the aerodynamic angle of attack of the tail surface never exceeded 10 degrees at trim.

(5) On the basis of conclusions (3) and (4) it is believed that the total dynamic pressure at the leading edge of the tail surface remained relatively constant over the entire angle of attack range of the wing.

(6) Depending on the longitudinal and vertical location of the tail surface relative to the wing MAC, the drag of the tail surface can have a significant effect on the pitching moment about the wing MAC.

(7) For the basic wing configuration having a nose down pitching moment, the tail lift required for system trim tended to reduce the lift from the value developed by the wing alone. This reduction became more significant as the longitudinal distance between the wing and tail MAC's was reduced.

(8) While the expanded theoretical prediction technique did not necessarily result in an improved correlation with the measured pressure distribution it did result in a program in which the basic mechanisms of the flow can be studied and analyzed independently.

(9) The major limitations of the theory lies in the prediction of the effect of the turbulent transition to the separated flow in the presence of a viscous vortex.

(10) It is believed that the prediction of the pressure distributions, particularly in the region of turbulent transition, will be improved by the better estimation of empirical parameters that will result from the extensive use of the program.

On the basis of the above conclusions, it is recommended that the theoretical prediction program be extensively utilized to predict the pressure distributions

of the lifting surfaces tested under this contract as well as
for other configurations of general interest and for which
pressure data is available. In addition, it is recommended
that the prediction program be streamlined, documented and
then made available to other interested organizations to
utilize as a design tool.

REFERENCES

1. An Experimental Investigation of Vortex Flow Control for High Lift Generation -- Richard P. White Jr. and John Balcerak; ONR CR212-223-2, December 1975.

2. A Theoretical and Experimental Investigation of Vortex Flow Control for High Lift Generation -- Richard P. White Jr., Santu T. Gangwani, and John Balcerak; ONR CR212-223-3, December 1976.

3. An Inventory of Aeronautical Ground Research Facilities -- C. J. Pierello, R. D. Hardin, M. V. Heckart, and K. R. Brown; NASA CR-1874, November 1971.

4. Jet Boundary Corrections for Complete and Semispan Wings in Circular Tunnels" -- J. C. Sevelles and R. M. Salmi, NACA TN 2454, 1951.

5. Calculation of Tunnel Induced Upwash Velocities for Swept and Towed Wings -- S. Katzoff and M. E. Hannah, NACA TN 1748, 1948.

6. "New Directions in Lifting Surface Theory"-- H. Ashley, S. E. Windall, and M. T. Landahl; AIAA Journal, Vol. 3, No. 1, January 1965, pp. 3-16.

7. "Extension of a Vortex - Lattice Method to Include Effects of Leading-Edge Separation" -- D. T. Mook and S. A. Maddox; Journal of Aircraft, Vol. 11, February 1974, pp. 127-128.

8. "Subsonic Unsteady Aerodynamics for General Configurations; Direct Application of the Nonplanar Doublet-Lattice Method" -- J. P. Giesing, T. P. Kalman and W. P. Roden; USAF FDL-TR-71-5, 1971.

9. "Axial Flow in Trailing Vortices" -- G. K. Batchelor; Journal of Fluid Mechanics, Vol. 20, Part 4, December 1964, pp. 645-658.

10. High Lift Generation by Use of Vortices -- R. P. White Jr. and A. D. Zalay; ONR NR212-223, RASA/SRL Report 74-12, July 1975.

11. High Lift Capabilities from Favorable Flow Interaction
    with Close-Coupled Canards -- R. W. Hale and D. E.
    Ordway; Sage Action, Inc., SAI-RR 7501, December 1975.

12. The Vortex Core Jet Near the Point of Generation --
    T. R. Goodman; AFOSR-TR-72-1158, Oceanics, Inc., Report
    No. 72-91, April 1972.

13. "The Decay of a Turbulent Trailing Vortex" -- P. R. Owen;
    The Aeronautical Quarterly, February 1970, pp. 69-78.

14. "Some Developments in the Theory of Vortex Breakdown"--
    J. B. Benjamin; Journal 9, Fluid Mechanics, Vol. 28,
    Part 2, 1967, pp. 65-84.

15. "Vortex Decay Above a Stationary Boundary" -- A. I.
    Barcilon; Journal 9, Fluid Mechanics, Vol. 27, Part 1,
    1967, pp. 155-175.

FIGURE 1: Picture of Wing Tail Model in the Wind Tunnel.
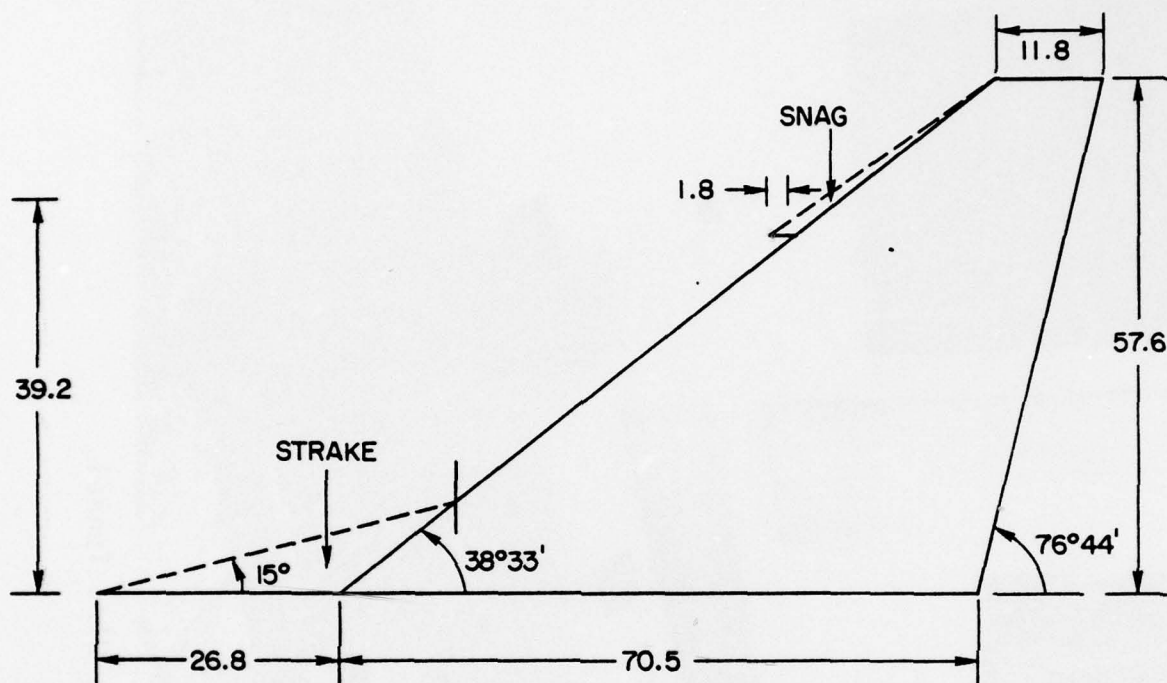
ALL DIMENSIONS ARE IN INCHES

FIGURE 2:   Wing Surface with Optional Appendages.
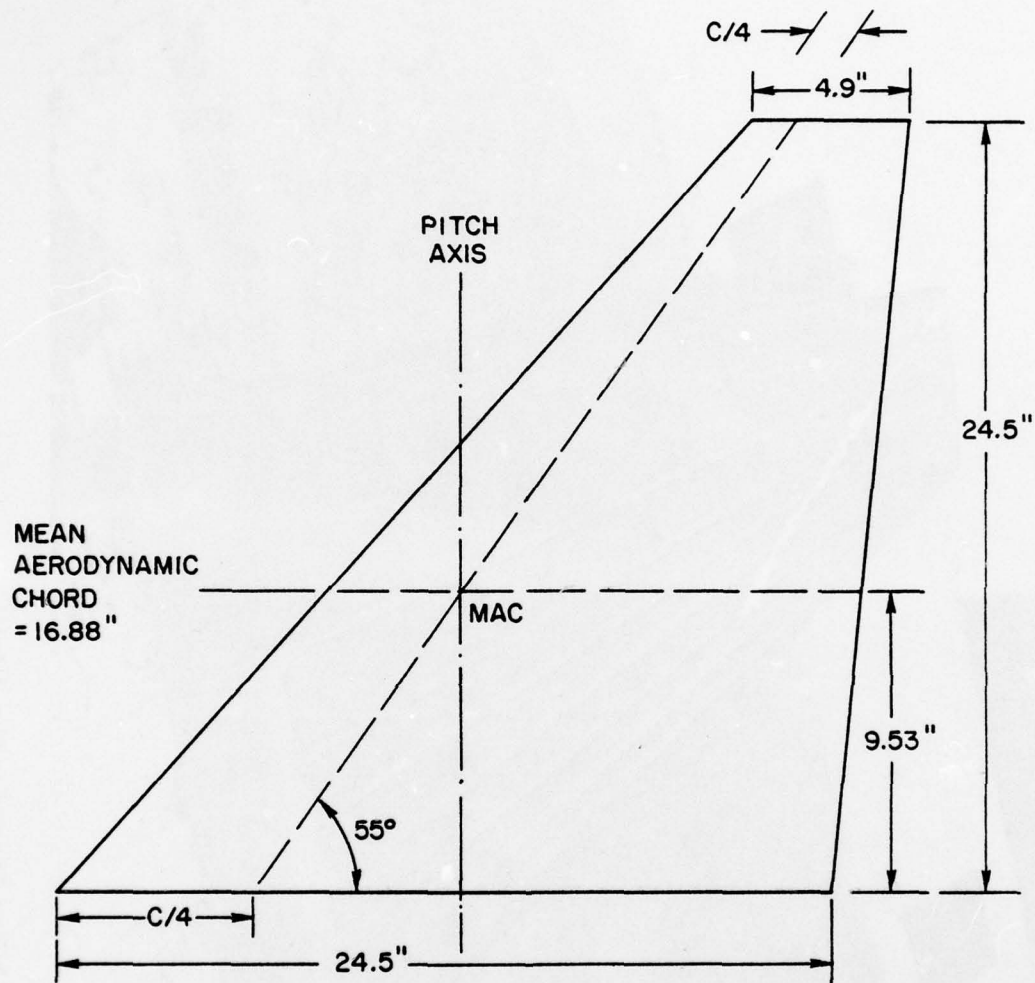
AIRFOIL SECTION: NACA 0006

ALL DIMENSIONS IN INCHES

FIGURE 3:   Tail Surface Geometry.
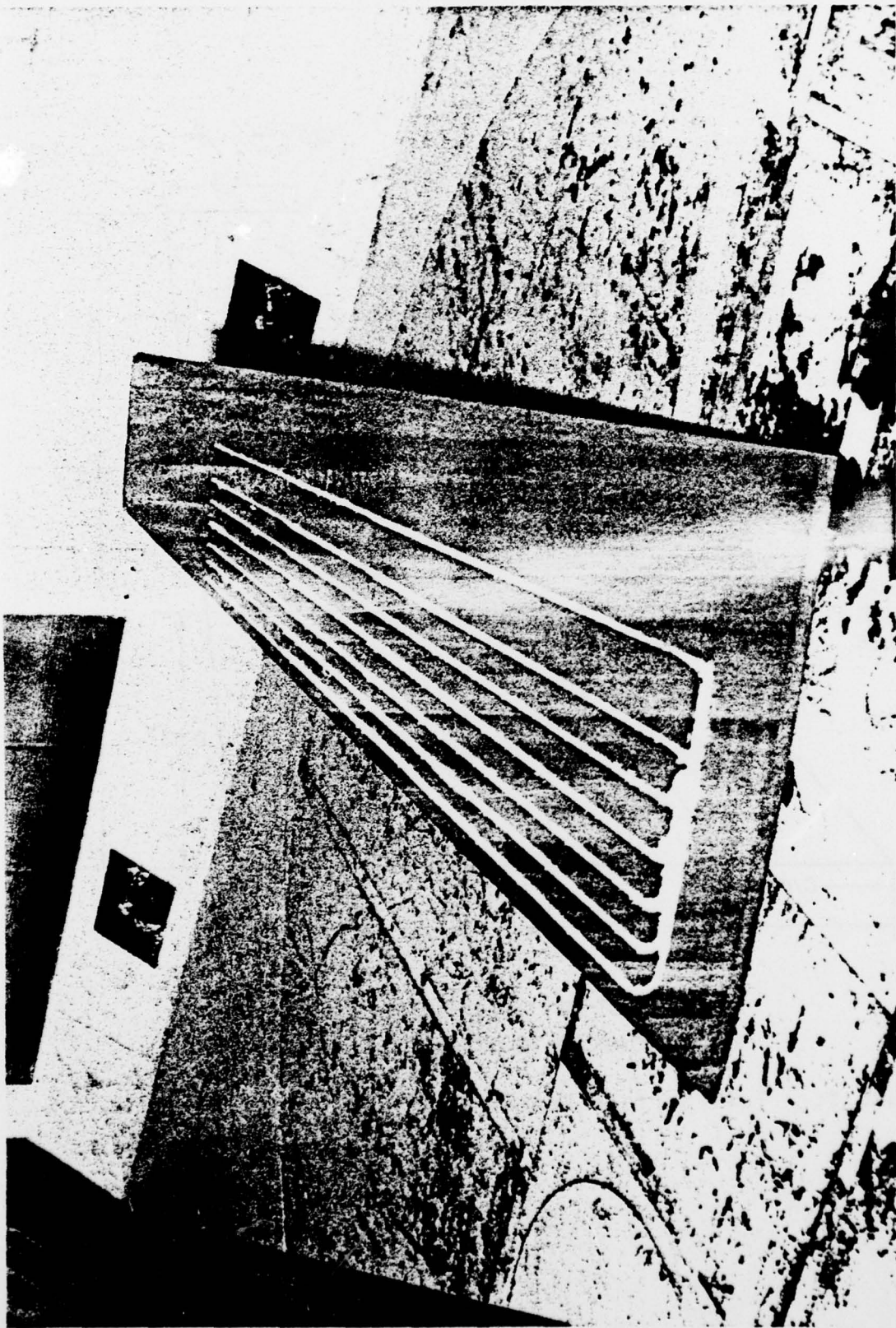
FIGURE 4: Picture of Tail Surface in the Wind Tunnel.
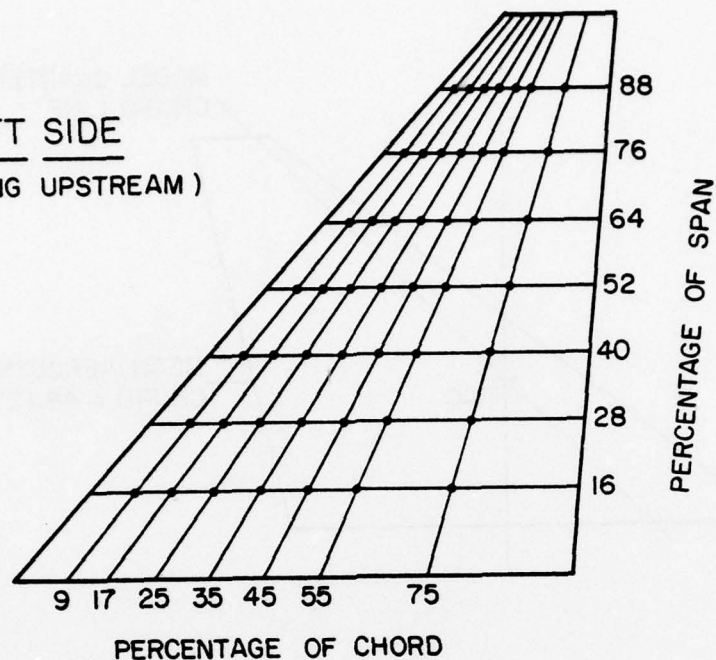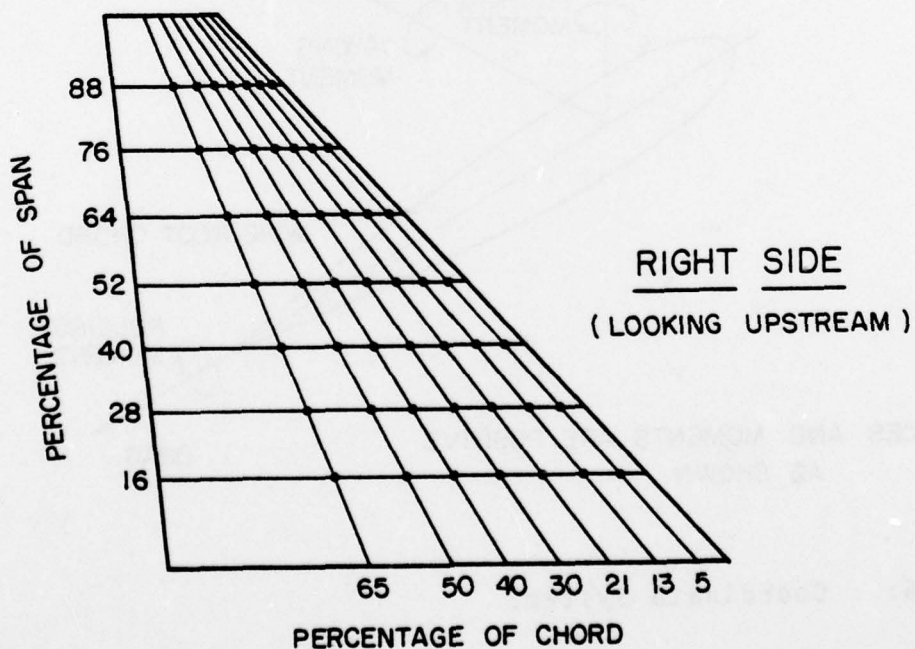
FIGURE 5:   Pressure Tap Locations on the Tail Surface.

MODEL QUARTER-
CHORD LINE

MEAN AERODYNAMIC
CHORD = 48.12"

MAC

21.96"

SIDE
FORCE

AIRFLOW

PITCHING
MOMENT

LIFT

YAWING
MOMENT

WING ROOT CHORD

ROLLING
MOMENT

FORCES AND MOMENTS ARE POSITIVE
AS SHOWN

DRAG
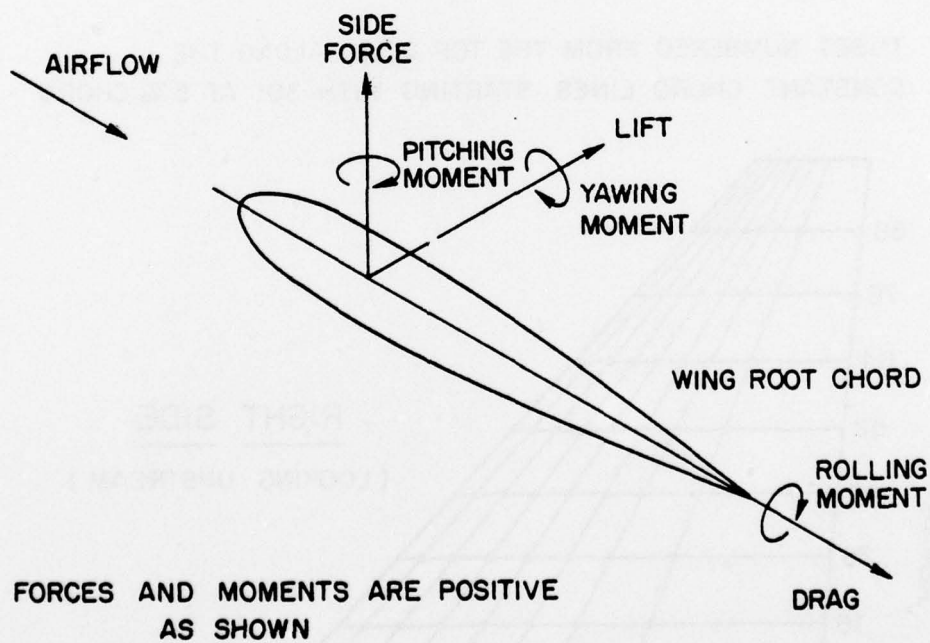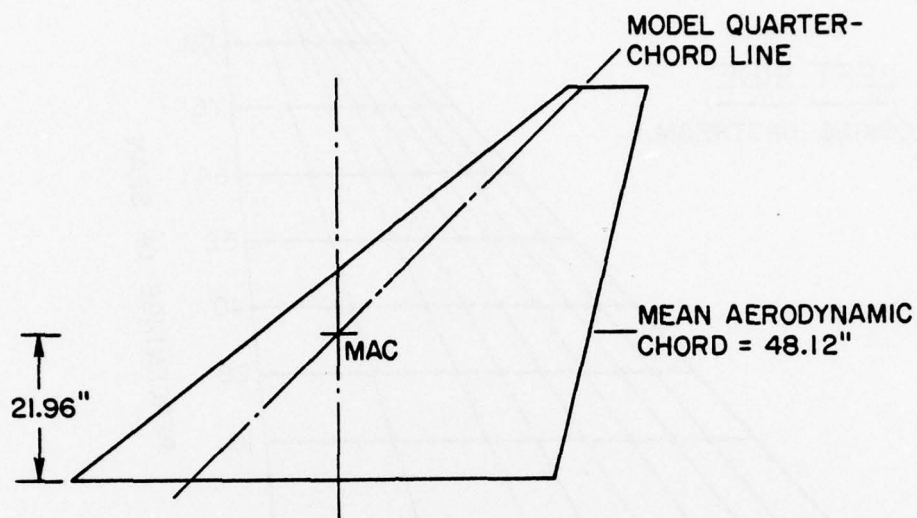
FIGURE 6:   Coordinate System.

82
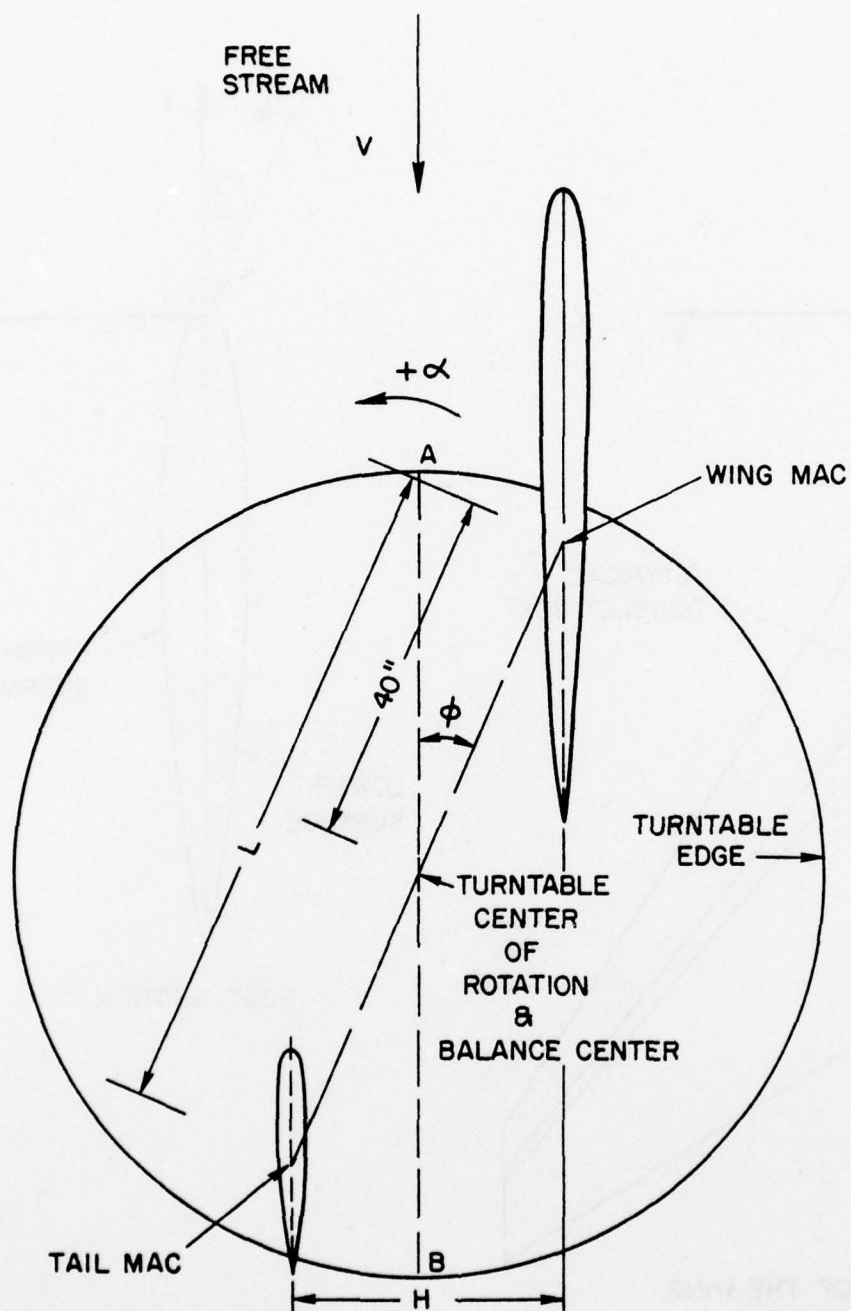
FIGURE 7: Model Arrangement on the Wind Tunnel Turntable.

83

PLANFORM OF THE WING

FIGURE 8: Geometry of the Potential Flow Model.

84
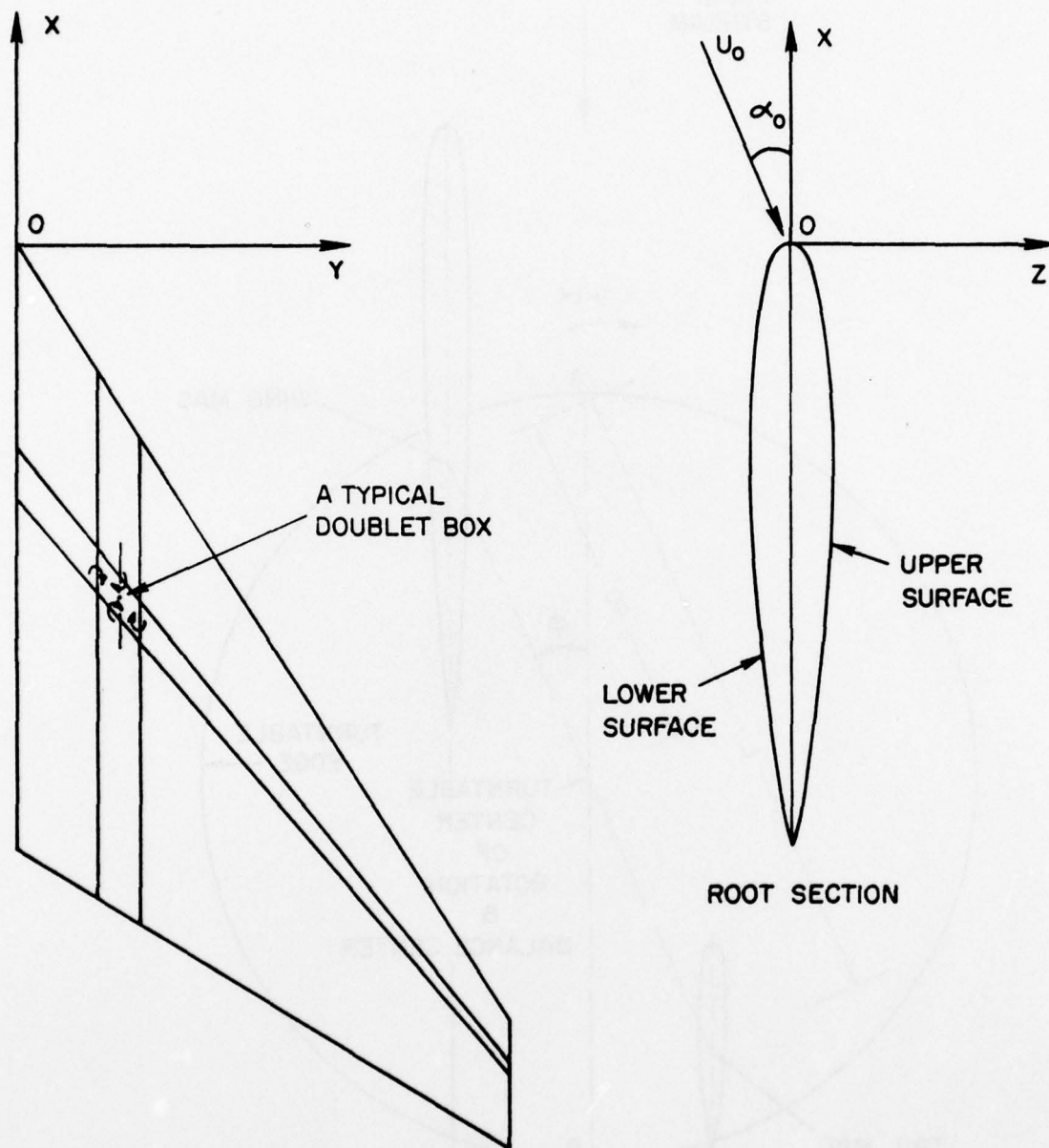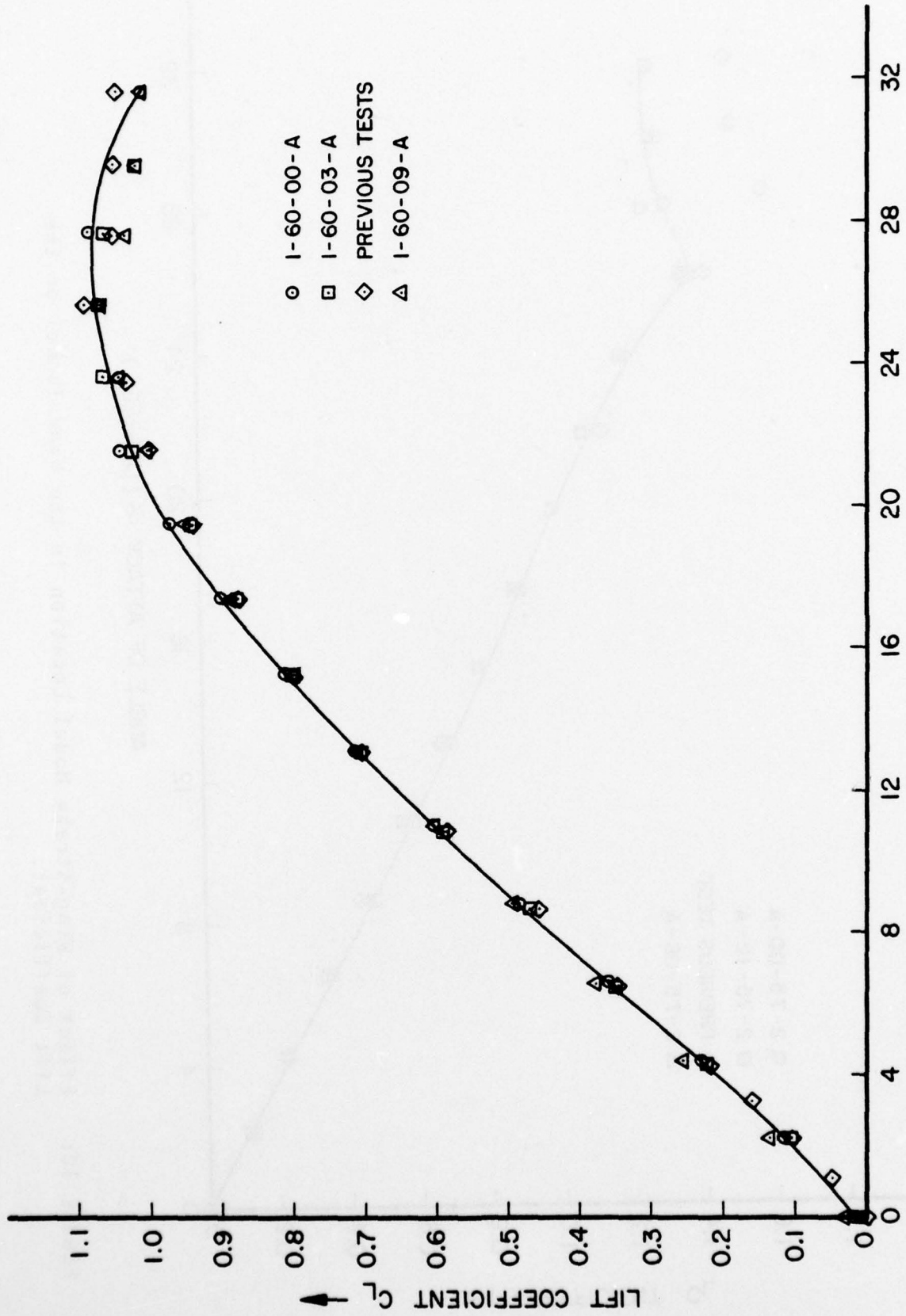
FIGURE 9: Effect of Basic Wing Location in the Wind Tunnel on the Lift Coefficient.

85
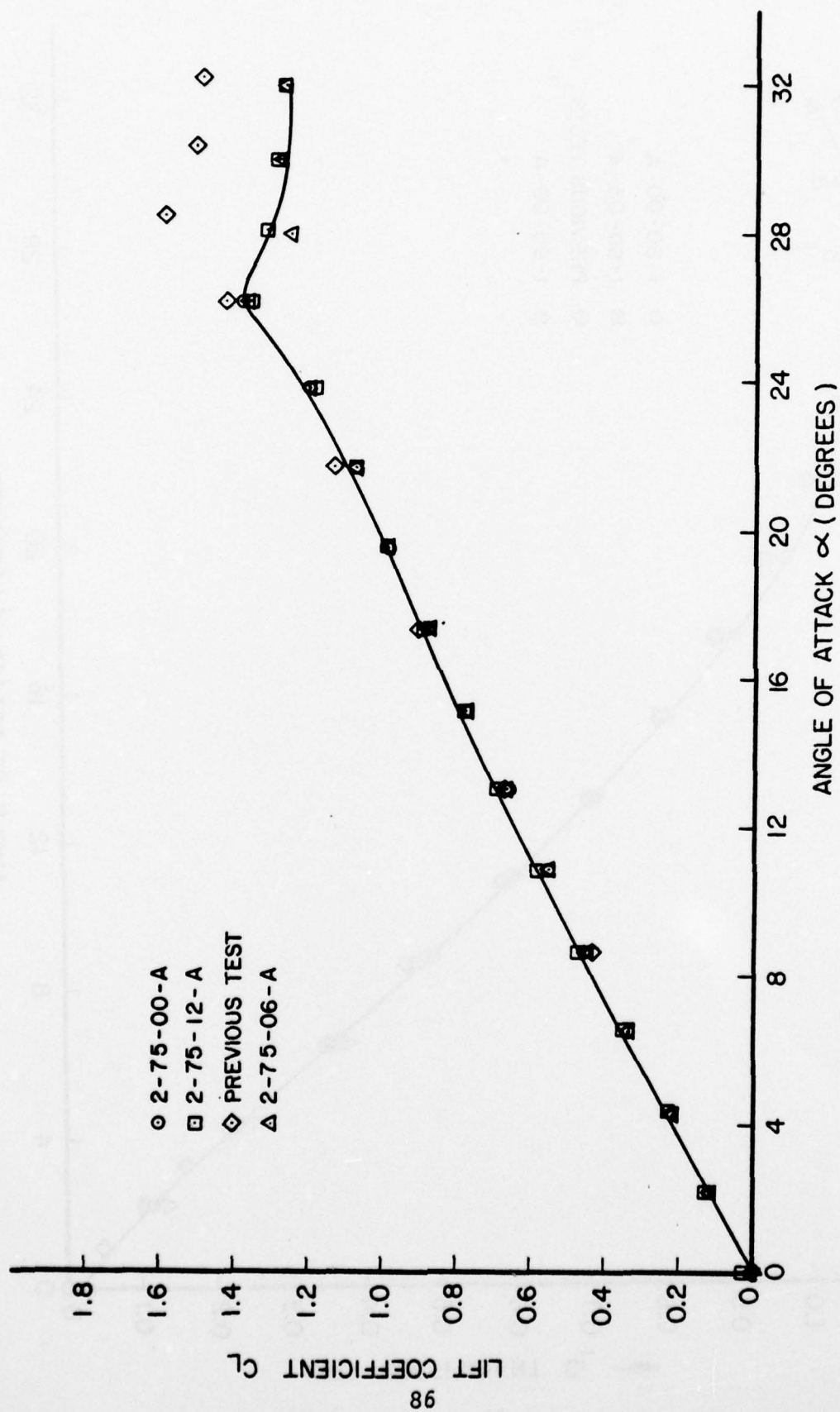
FIGURE 10: Effect of Wing-Strake Model Location in the Wind Tunnel on the Lift Coefficient.
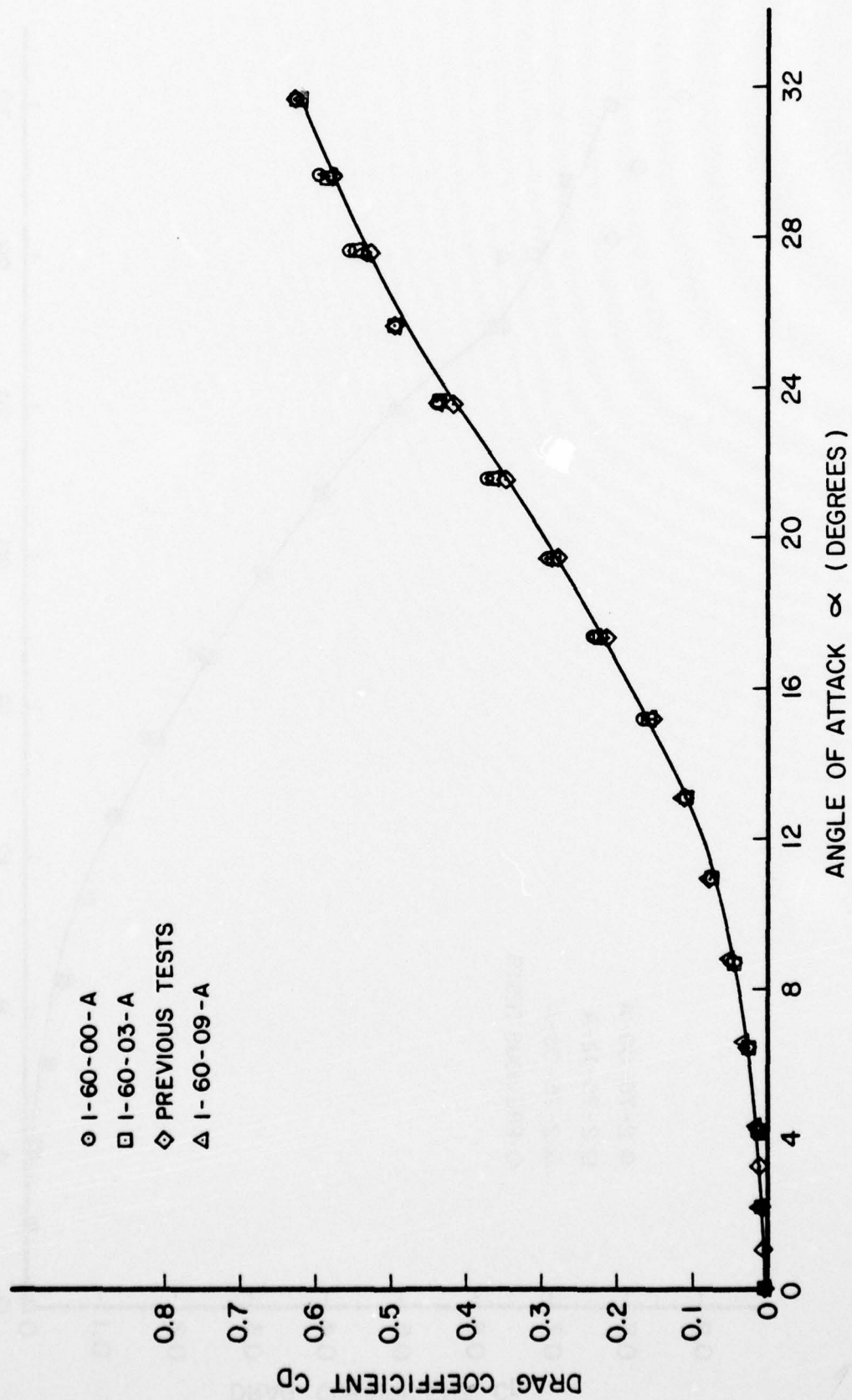
FIGURE 11: Effect of Basic Wing Location in the Wind Tunnel on the Drag Coefficient.

87
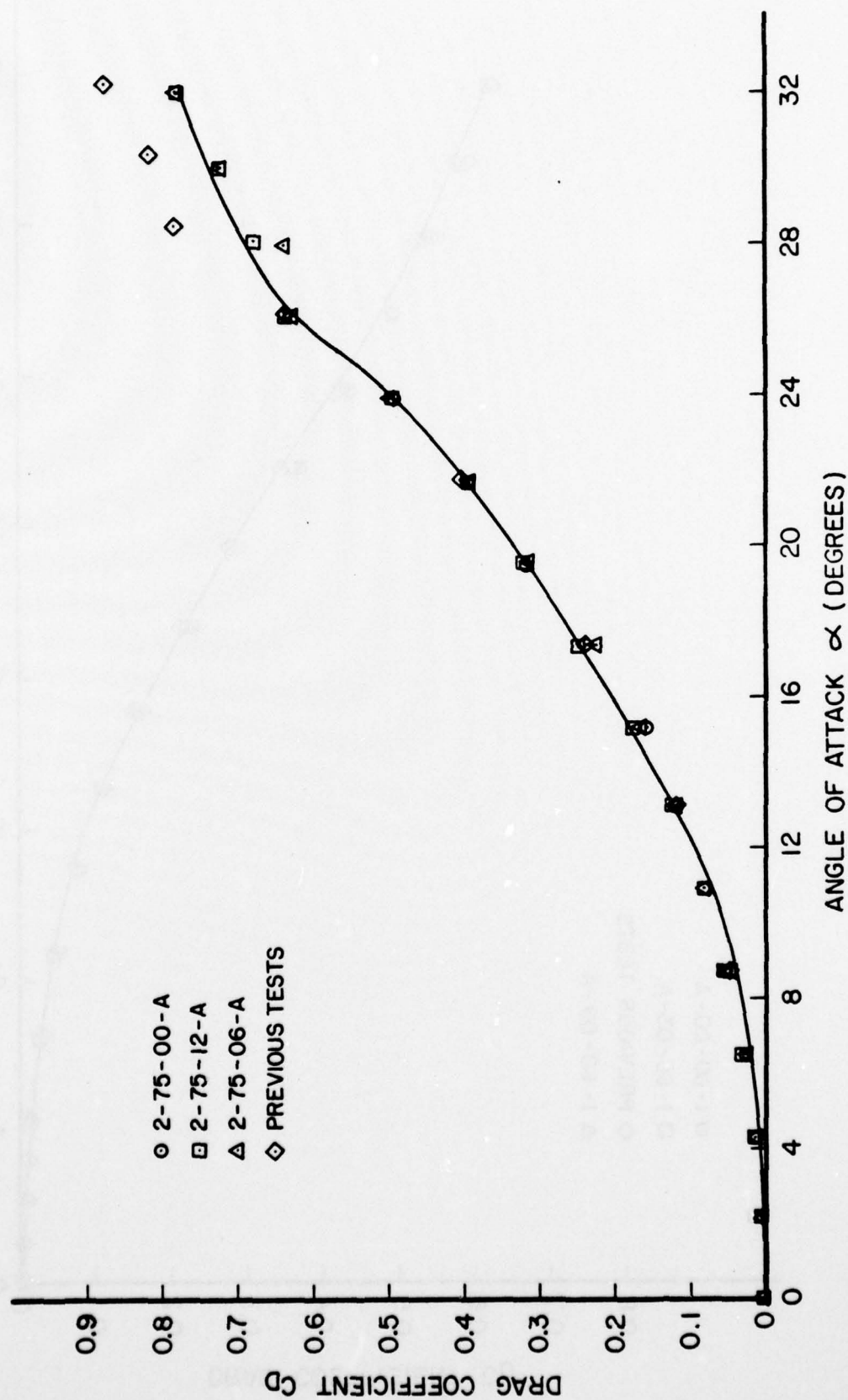
FIGURE 12: Effect of Wing-Strake Model Location in the Wind Tunnel on the Drag Coefficient.
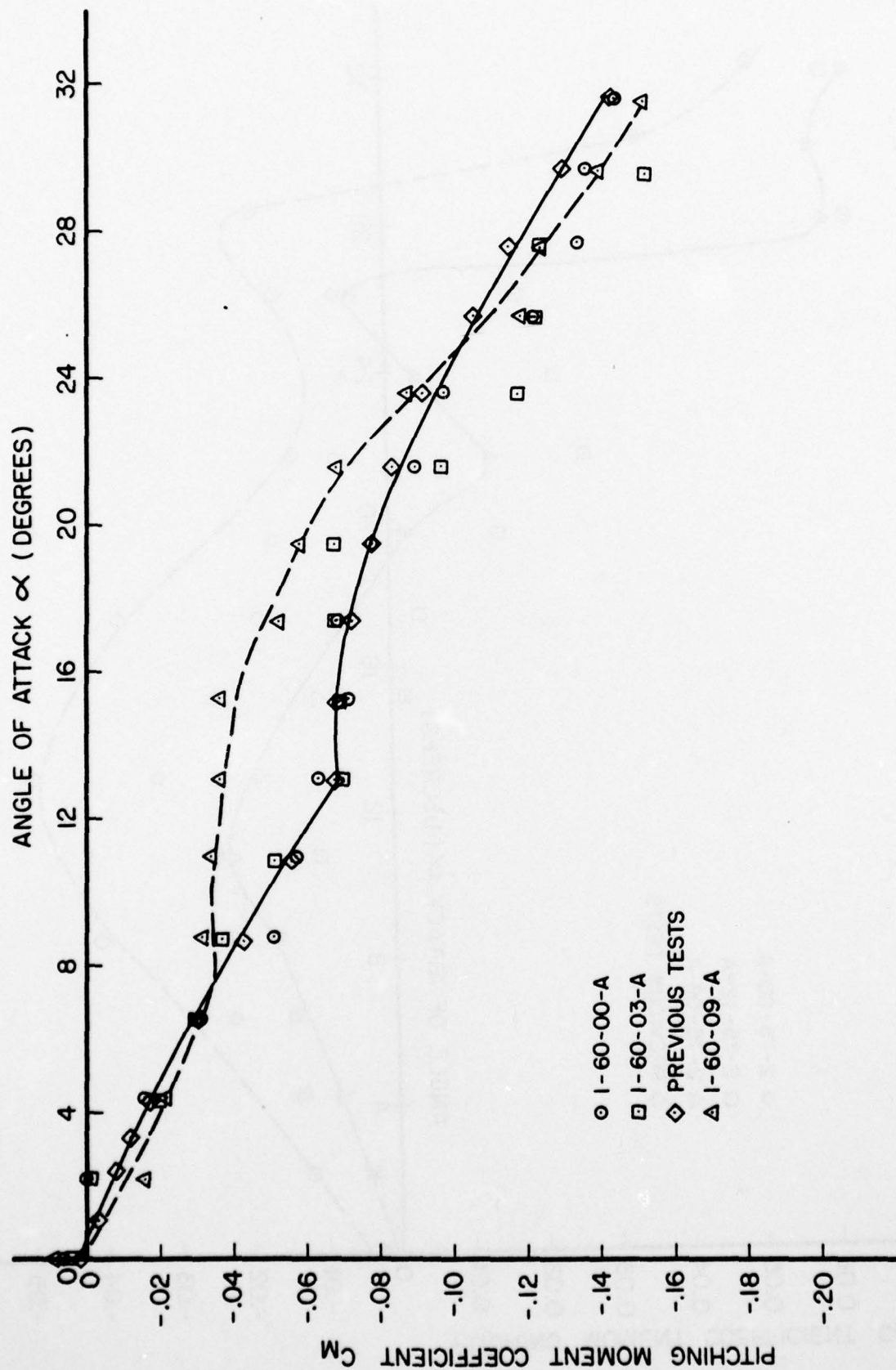
FIGURE 13: Effect of Basic Wing Location in the Wind Tunnel on the Pitching Moment Coefficient.

89
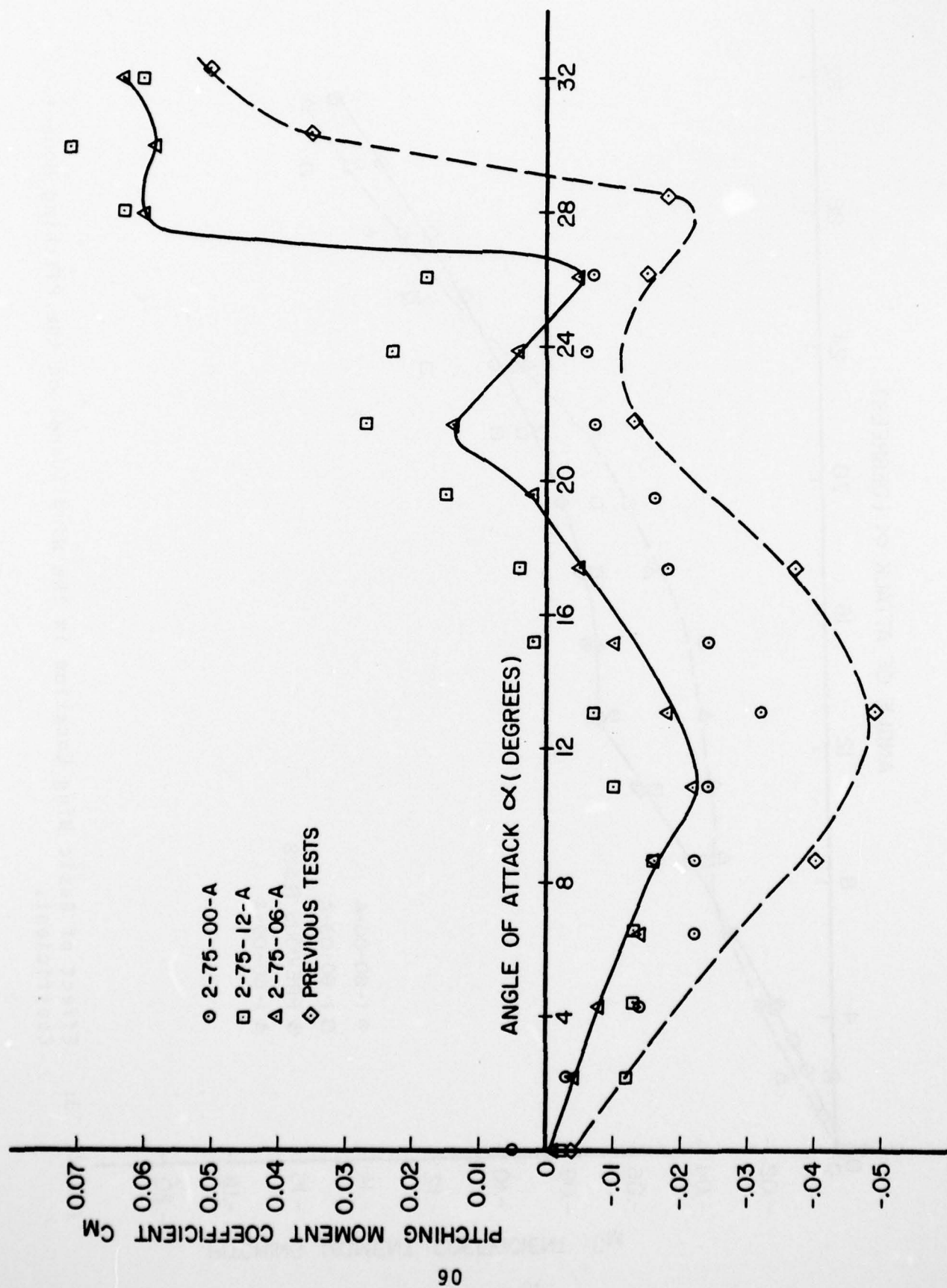
FIGURE 14: Effect of Wing-Strake Model Location in the Wind Tunnel on the Pitching Moment Coefficient.
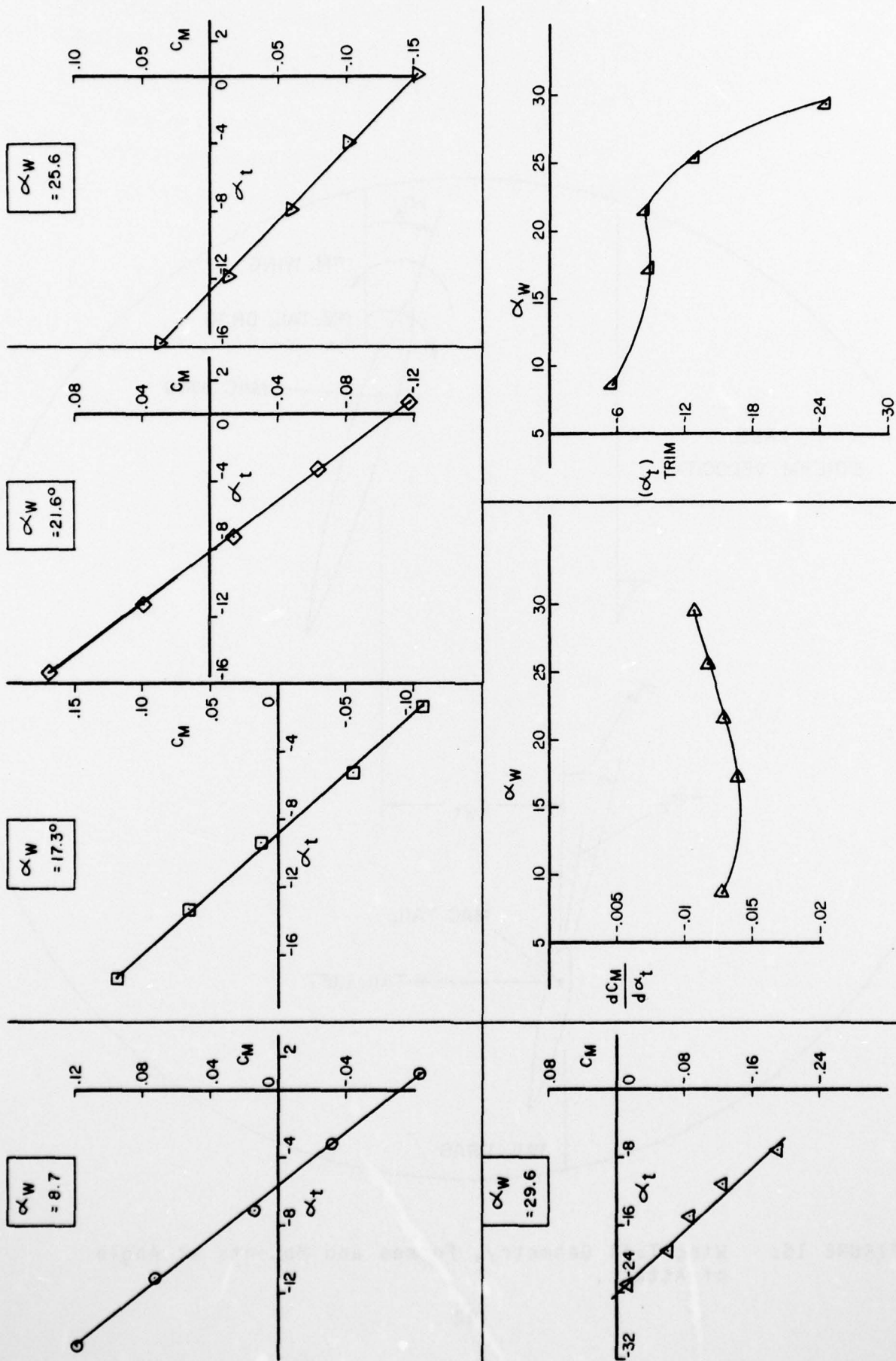
FIGURE 15: Tail Effectiveness of Configuration 1-75-06B.
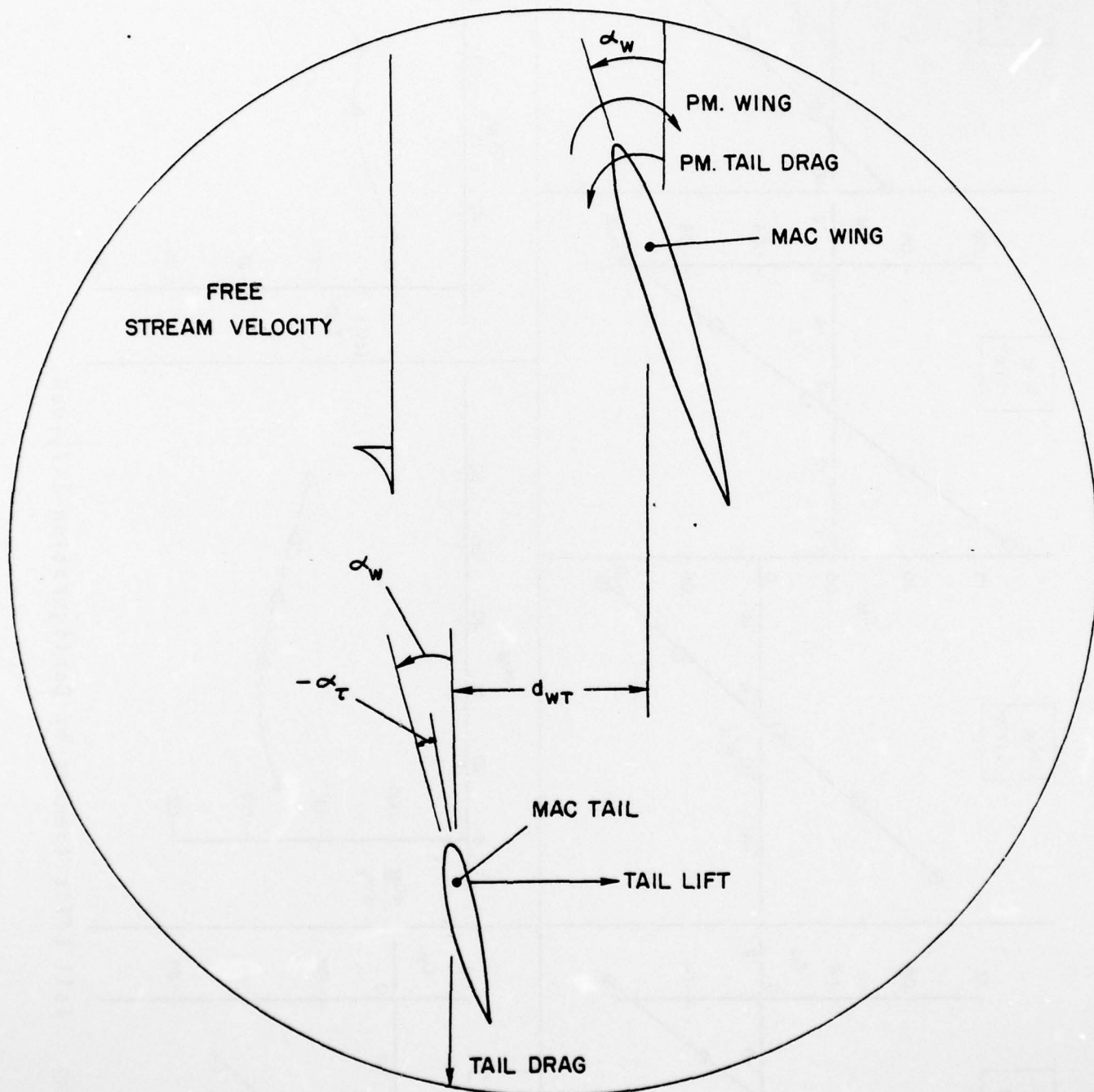
FIGURE 16: Wing-Tail Geometry, Forces and Moments at Angle of Attack.

92
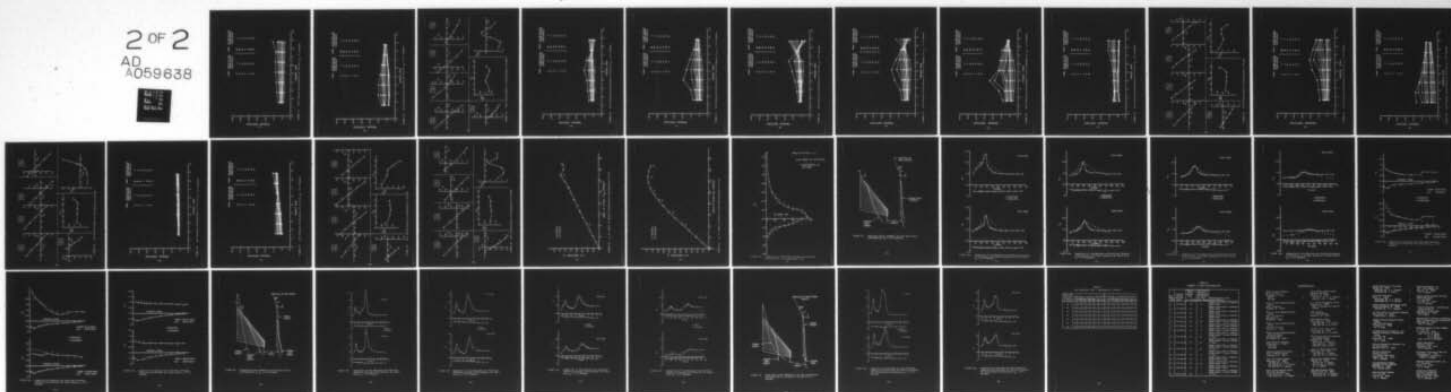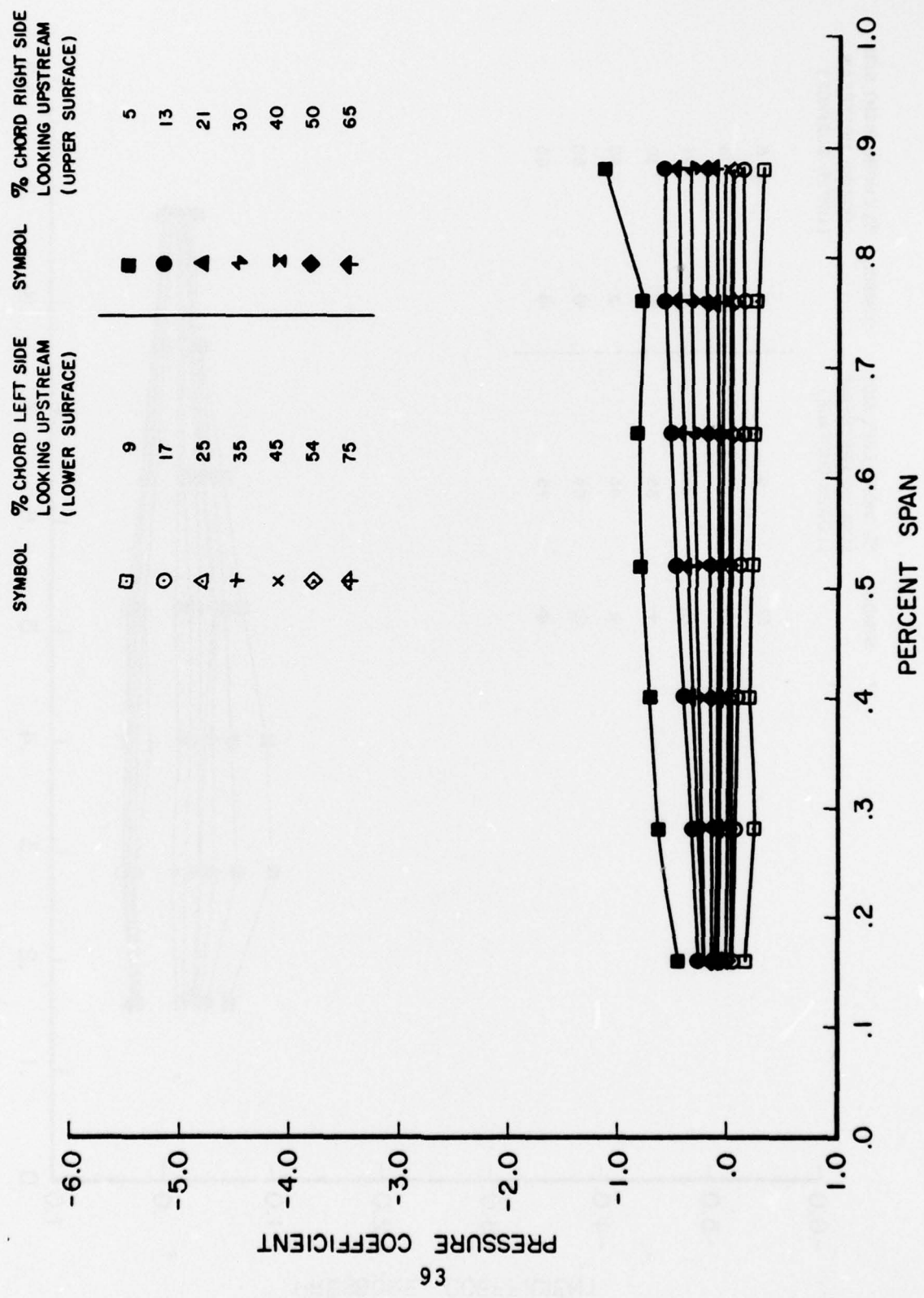
FIGURE 17:   Tail Pressure Distributions at Trim for α_w = 8.7 Degrees.
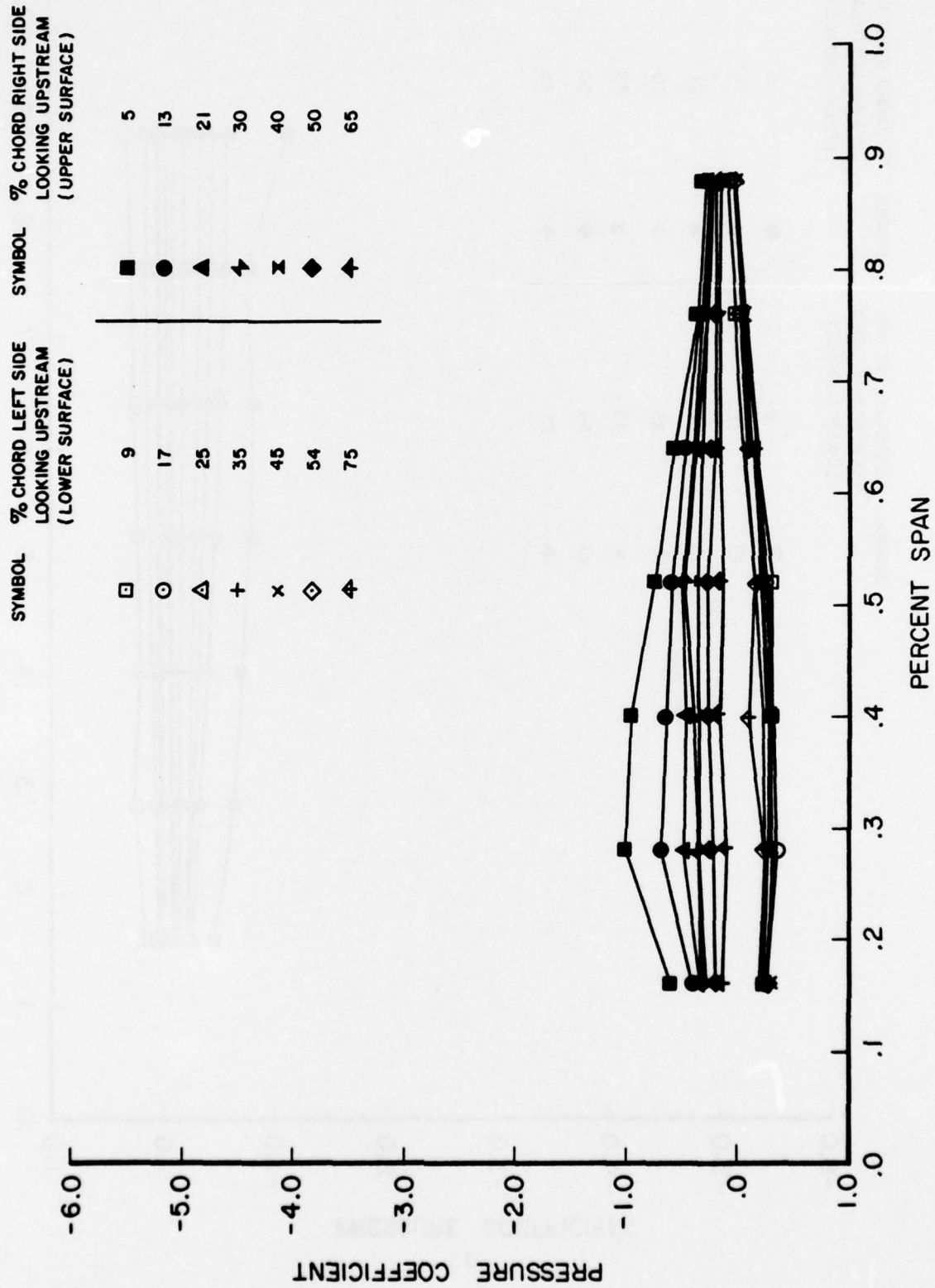
FIGURE 18: Tail Pressure Distributions at Trim for α_w = 29.7 Degrees.

94
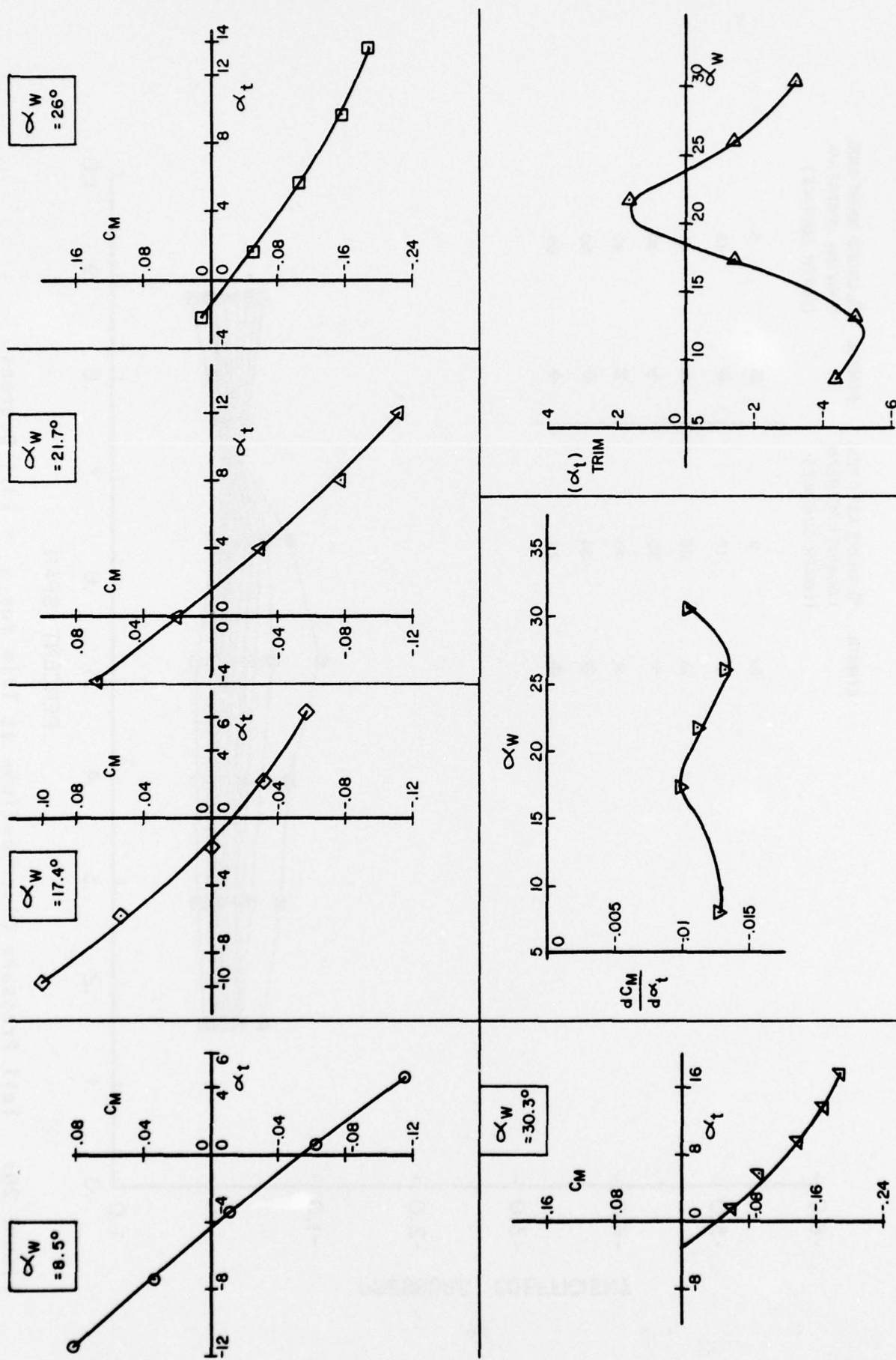
FIGURE 19: Tail Effectiveness of Configuration 2-75-06B.
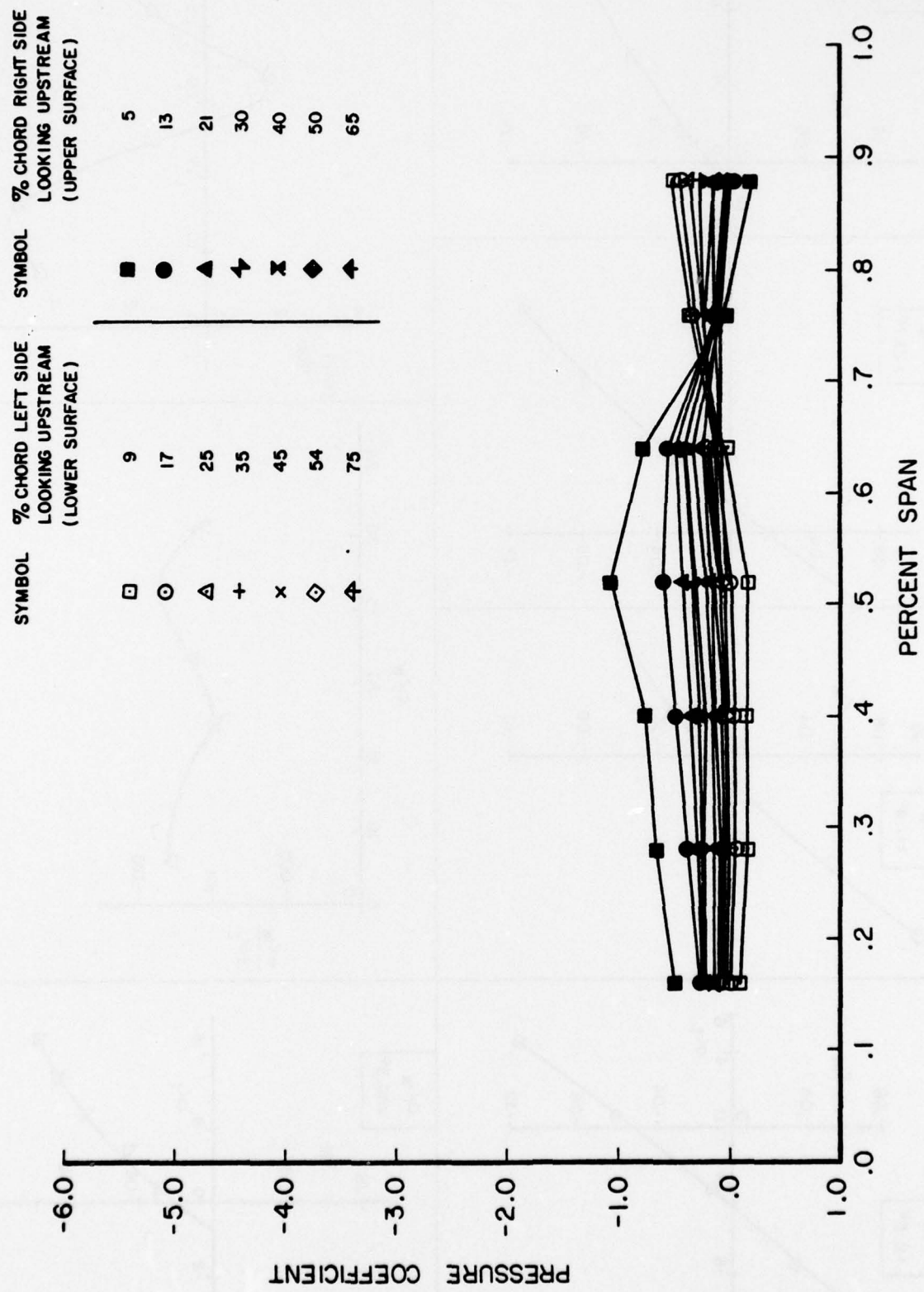
FIGURE 20: Tail Pressure Distributions at Trim for α_w = 13.1 Degrees.

96
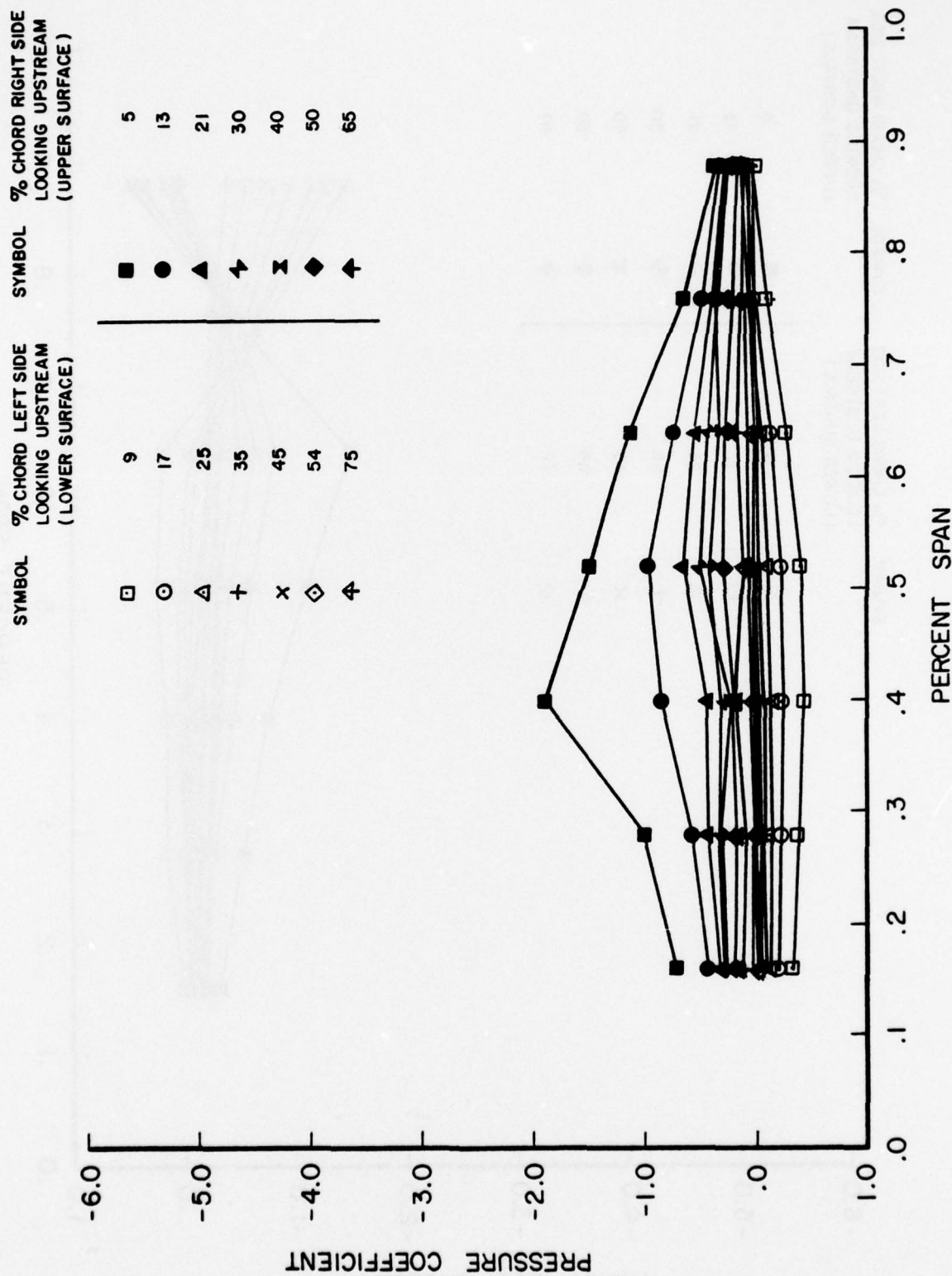
FIGURE 21: Tail Pressure Distributions at Trim -4 Degrees for α_w = 13.1 Degrees.
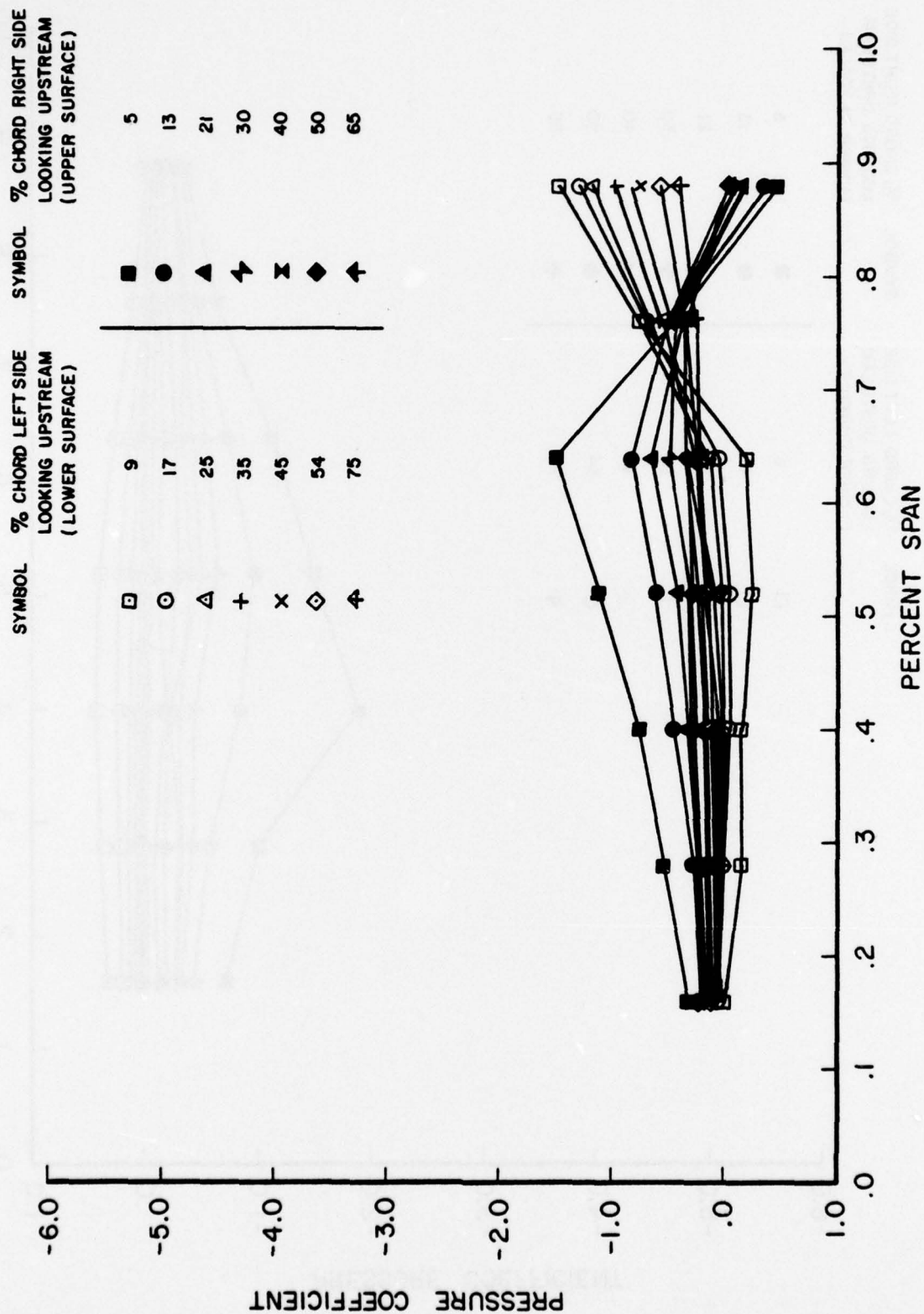
FIGURE 22: Tail Pressure Distributions at Trim for α_w = 17.4 Degrees.

98
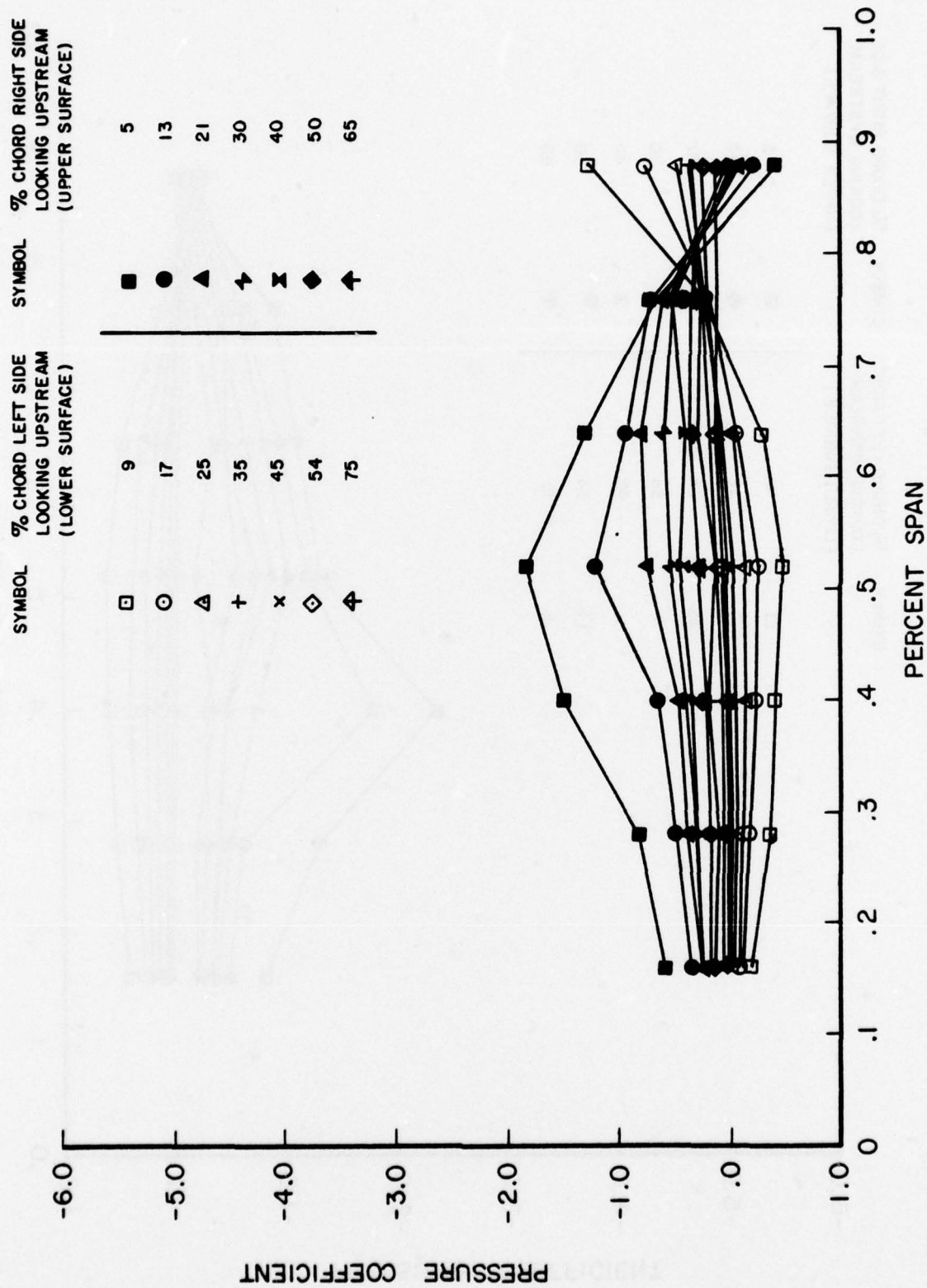
FIGURE 23: Tail Pressure Distributions at Trim -4 Degrees for α_w = 17.4 Degrees.

FIGURE 24: Tail Pressure Distributions at Trim -8 Degrees for $\alpha_w = 17.4$ Degrees.

100
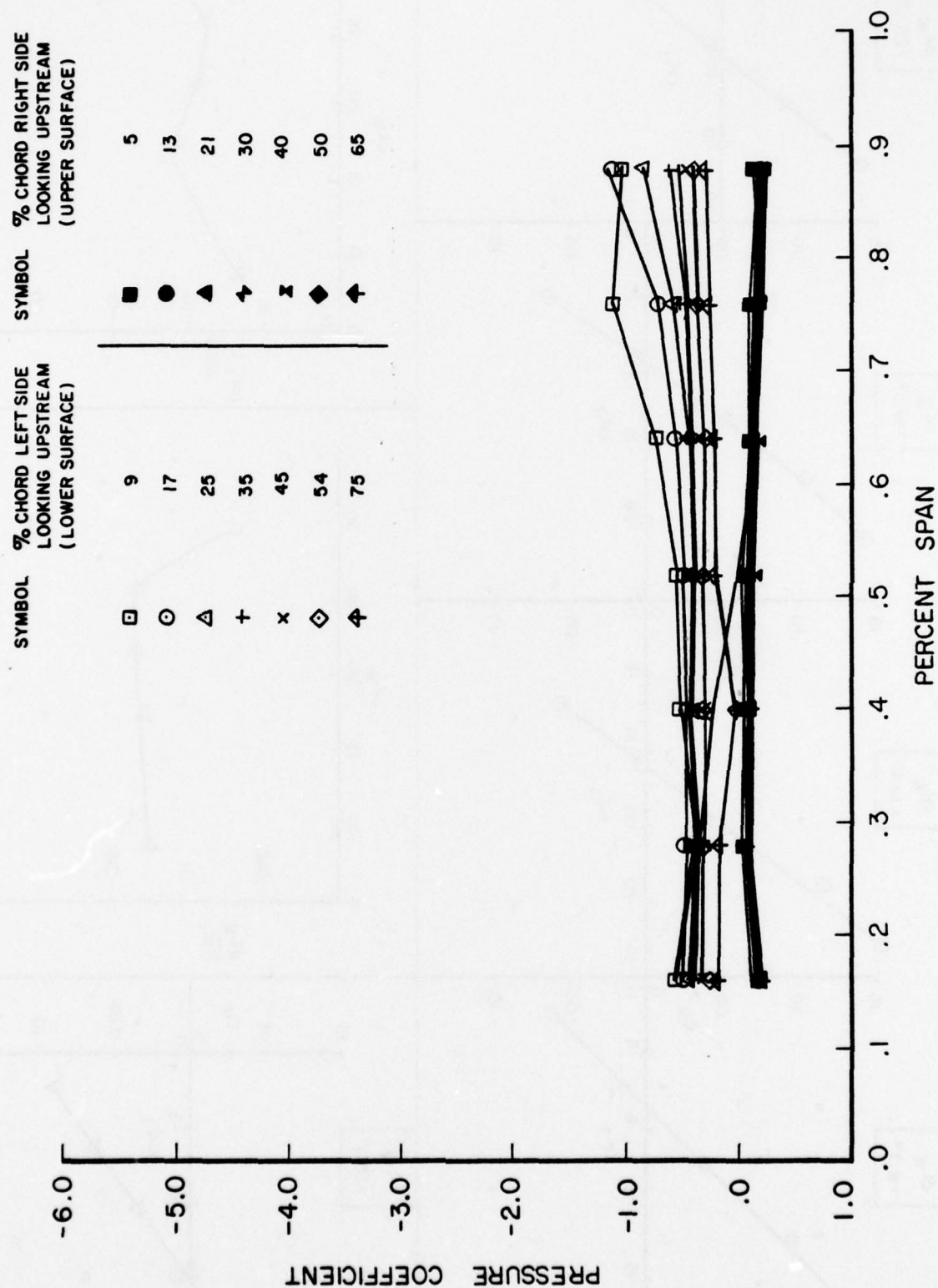
FIGURE 25: Tail Pressure Distributions at Trim for α_w = 30.3 Degrees.
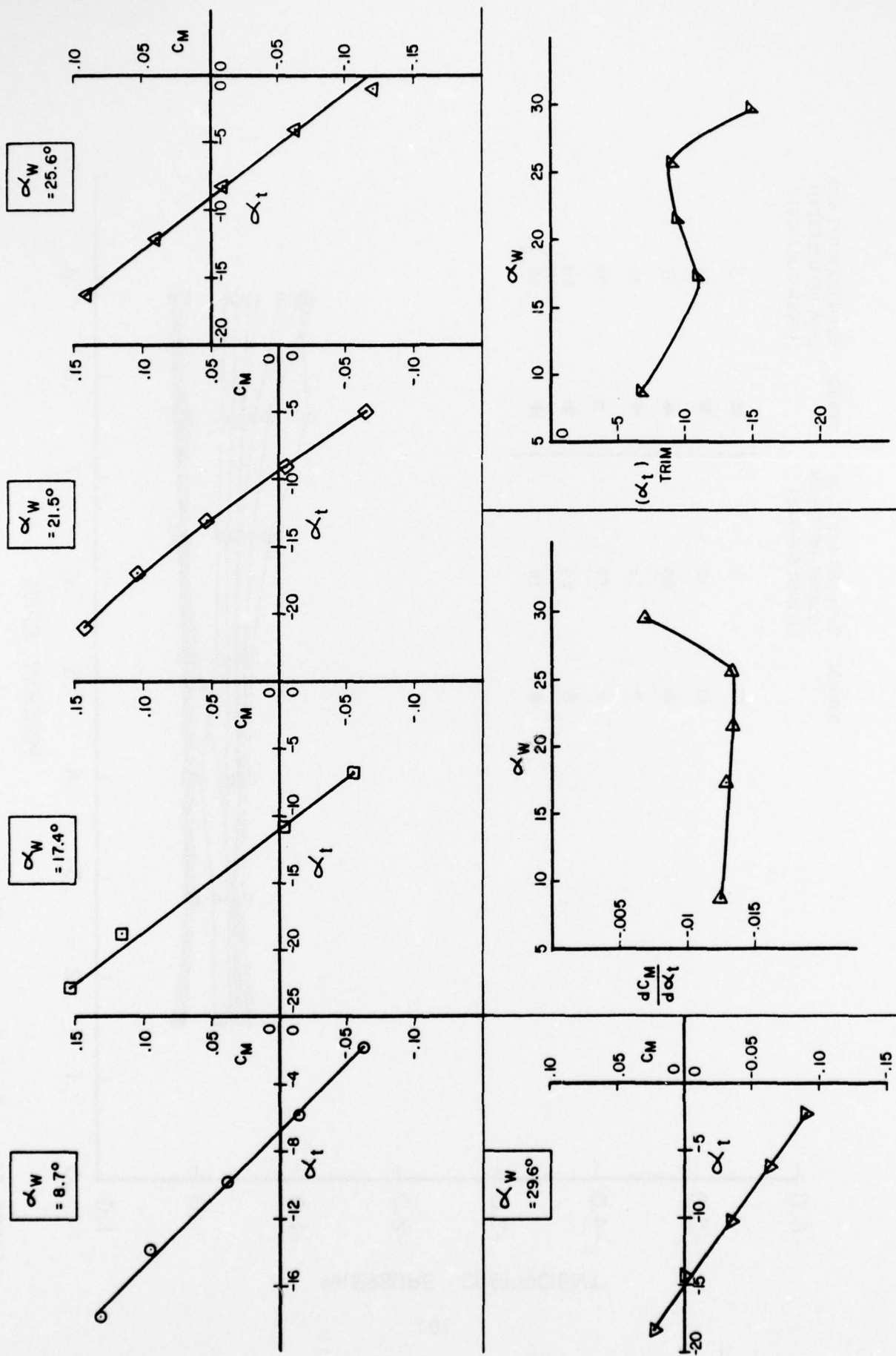
FIGURE 26: Tail Effectiveness of Configuration 1-75-12B.
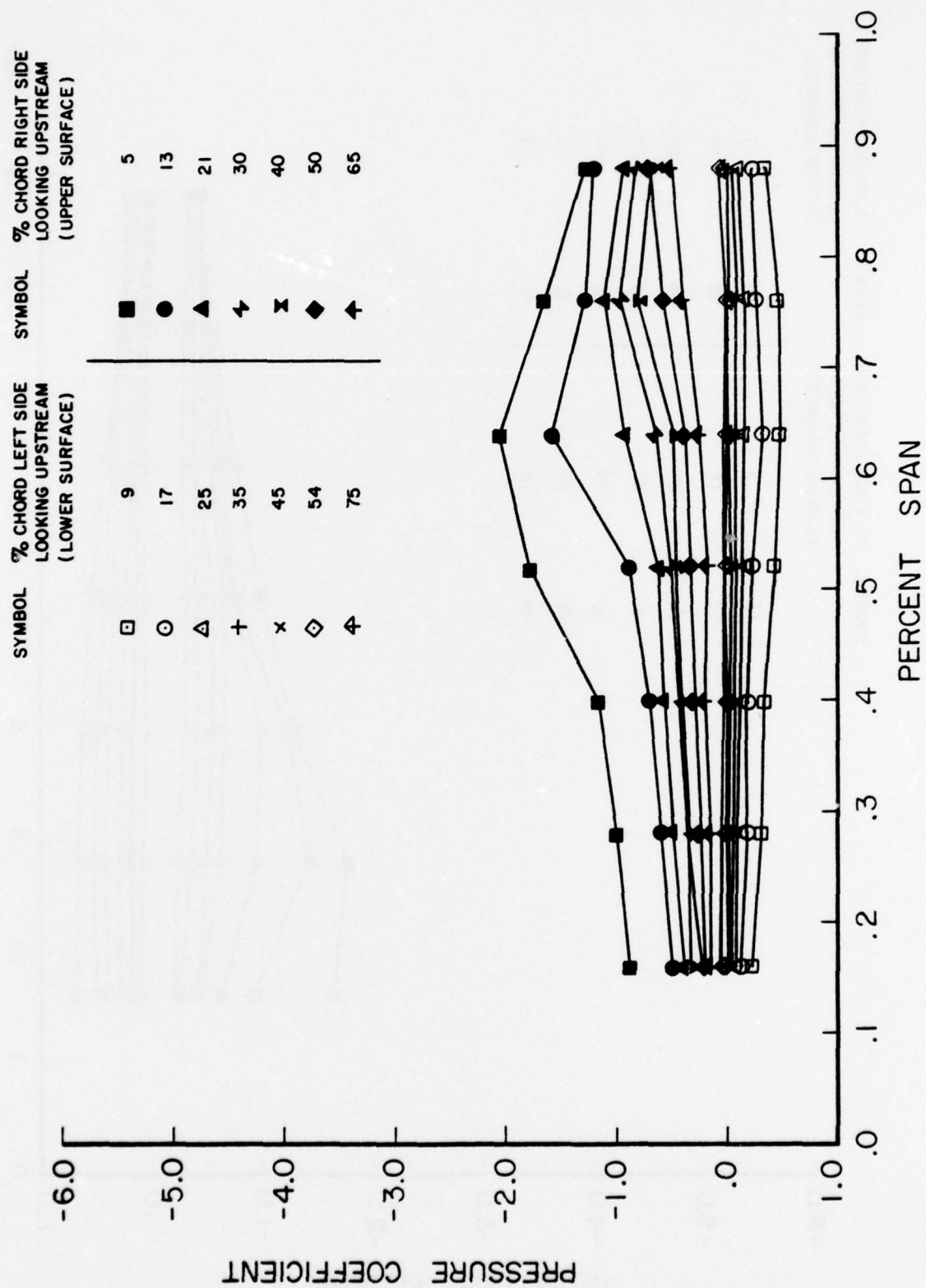
FIGURE 27: Tail Pressure Distributions at Trim for α_w = 25.6 Degrees.

103
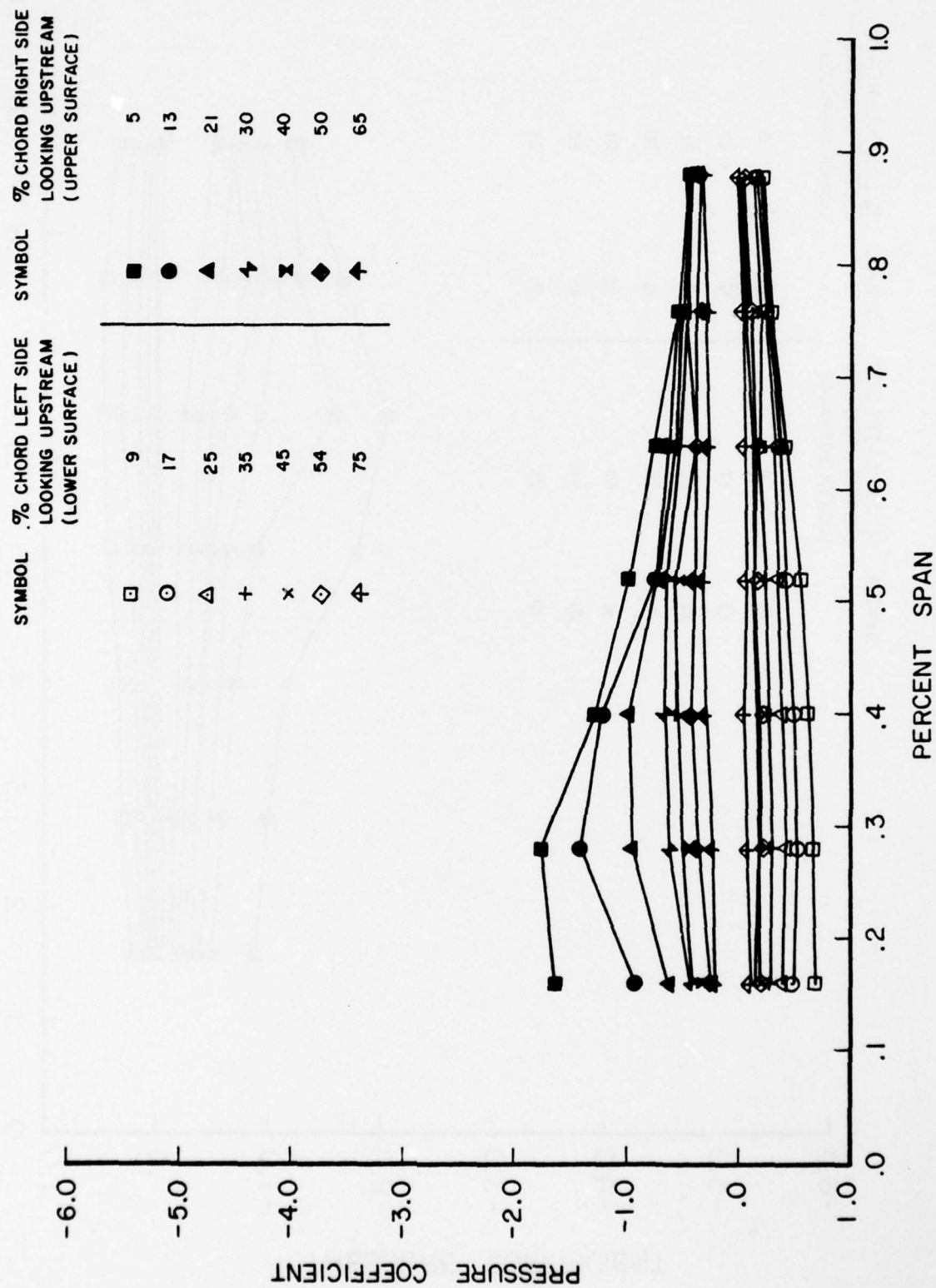
FIGURE 28: Tail Pressure Distributions at Trim for $\alpha_w = 29.6$ Degrees.
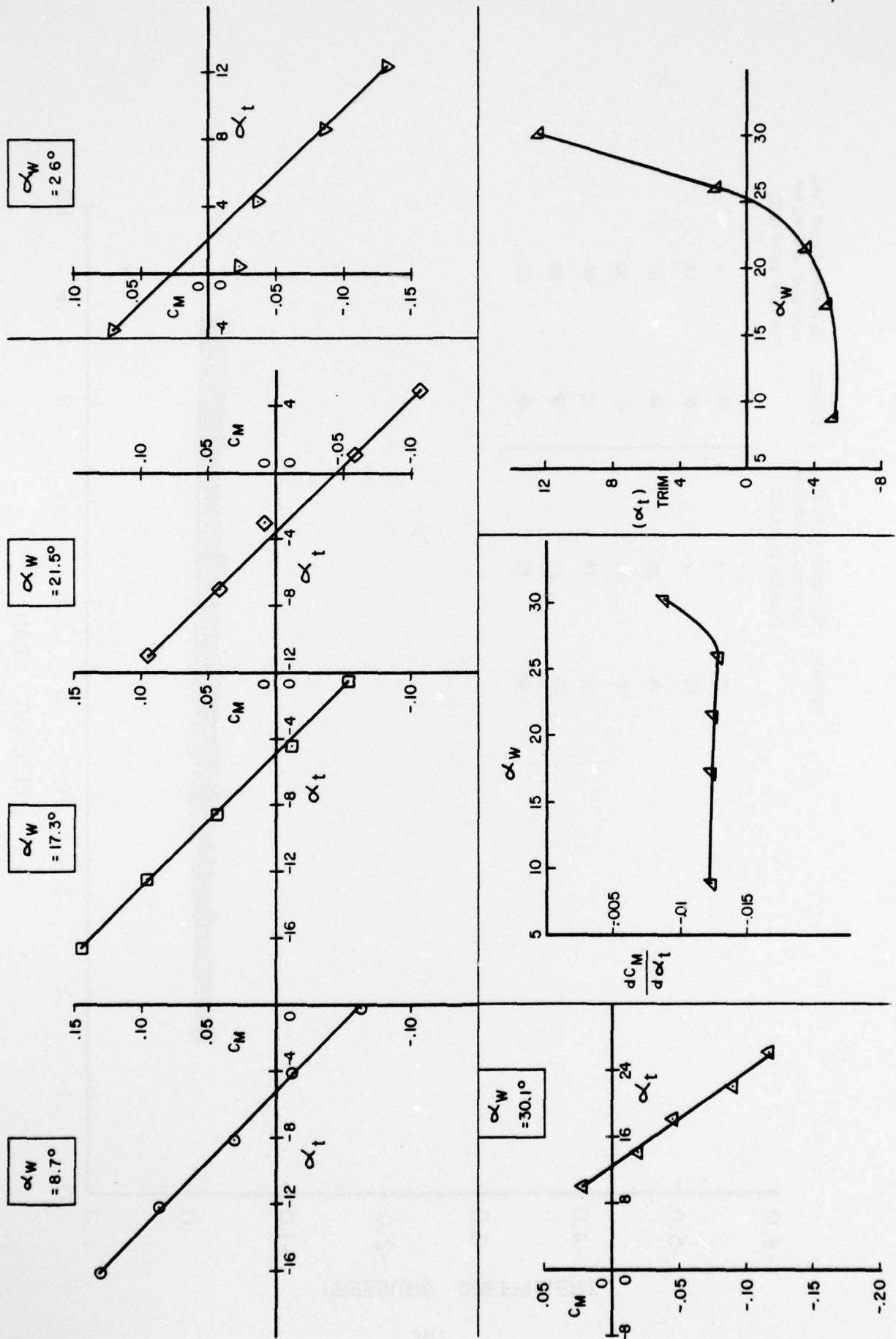
FIGURE 29: Tail Effectiveness of Configuration 2-75-12B.
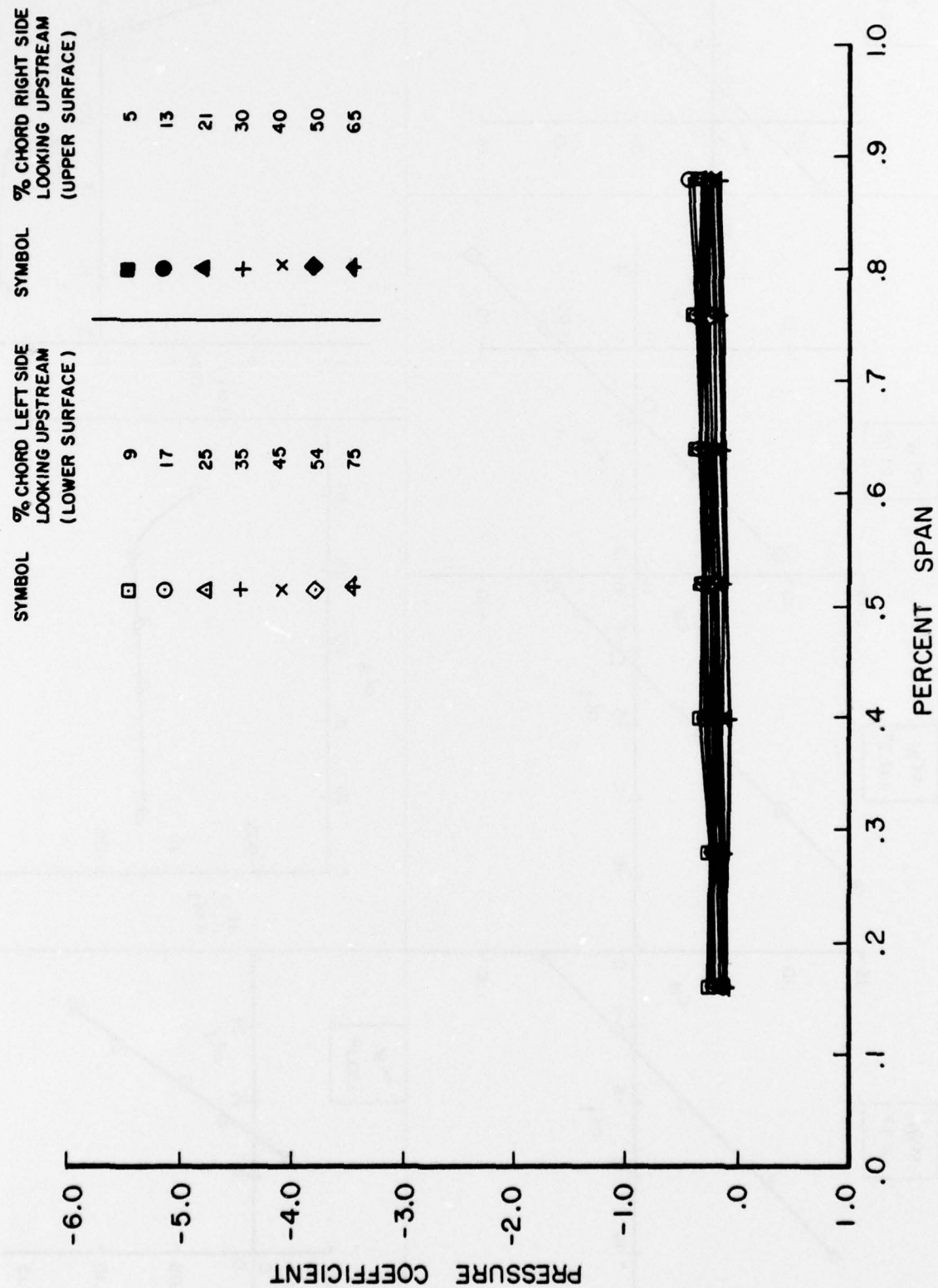
FIGURE 30: Tail Pressure Distributions at Trim for $\alpha_W = 21.5$ Degrees.
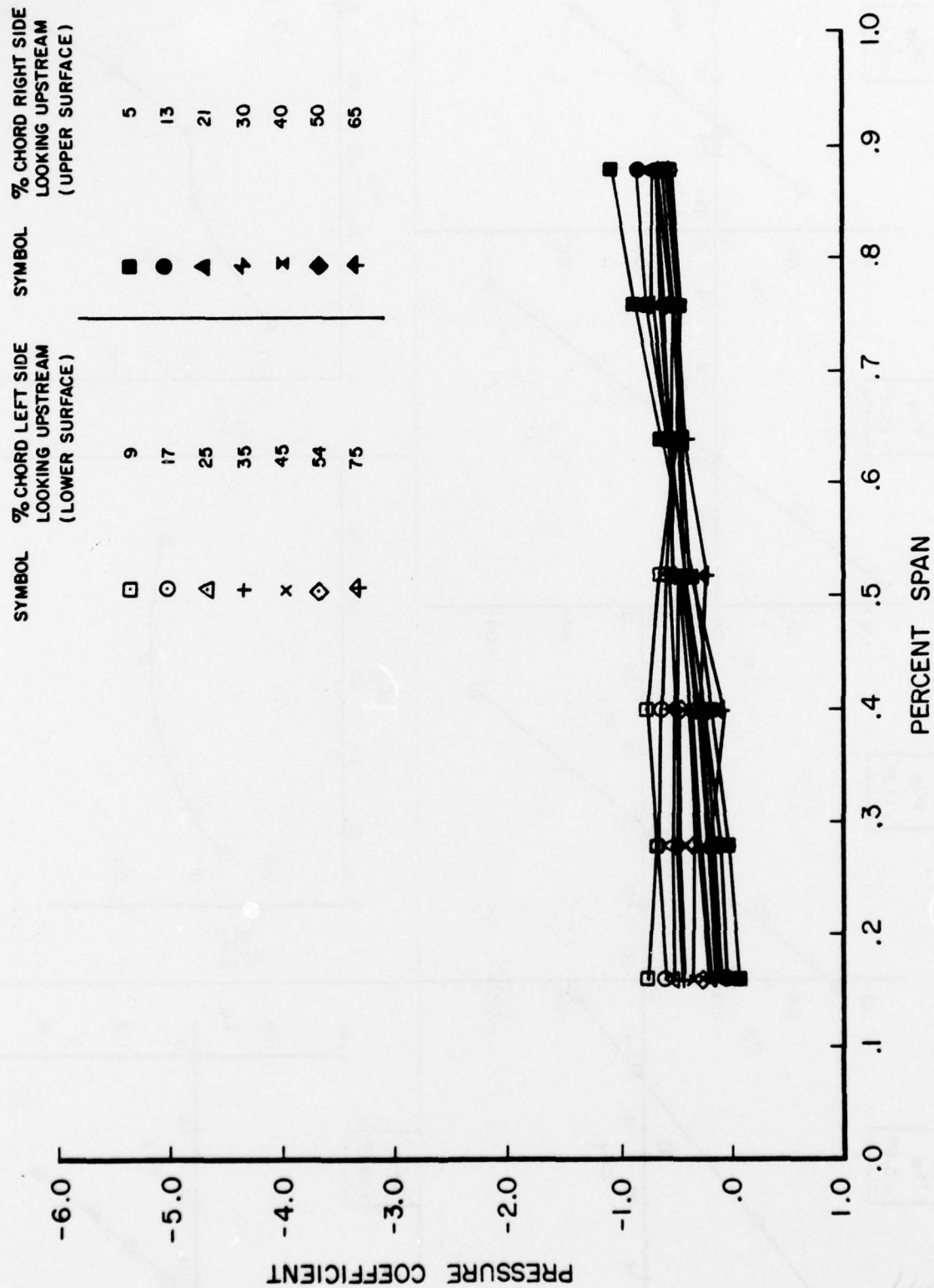
FIGURE 31: Tail Pressure Distributions at Trim for $\alpha_w = 30.1$ Degrees.

107
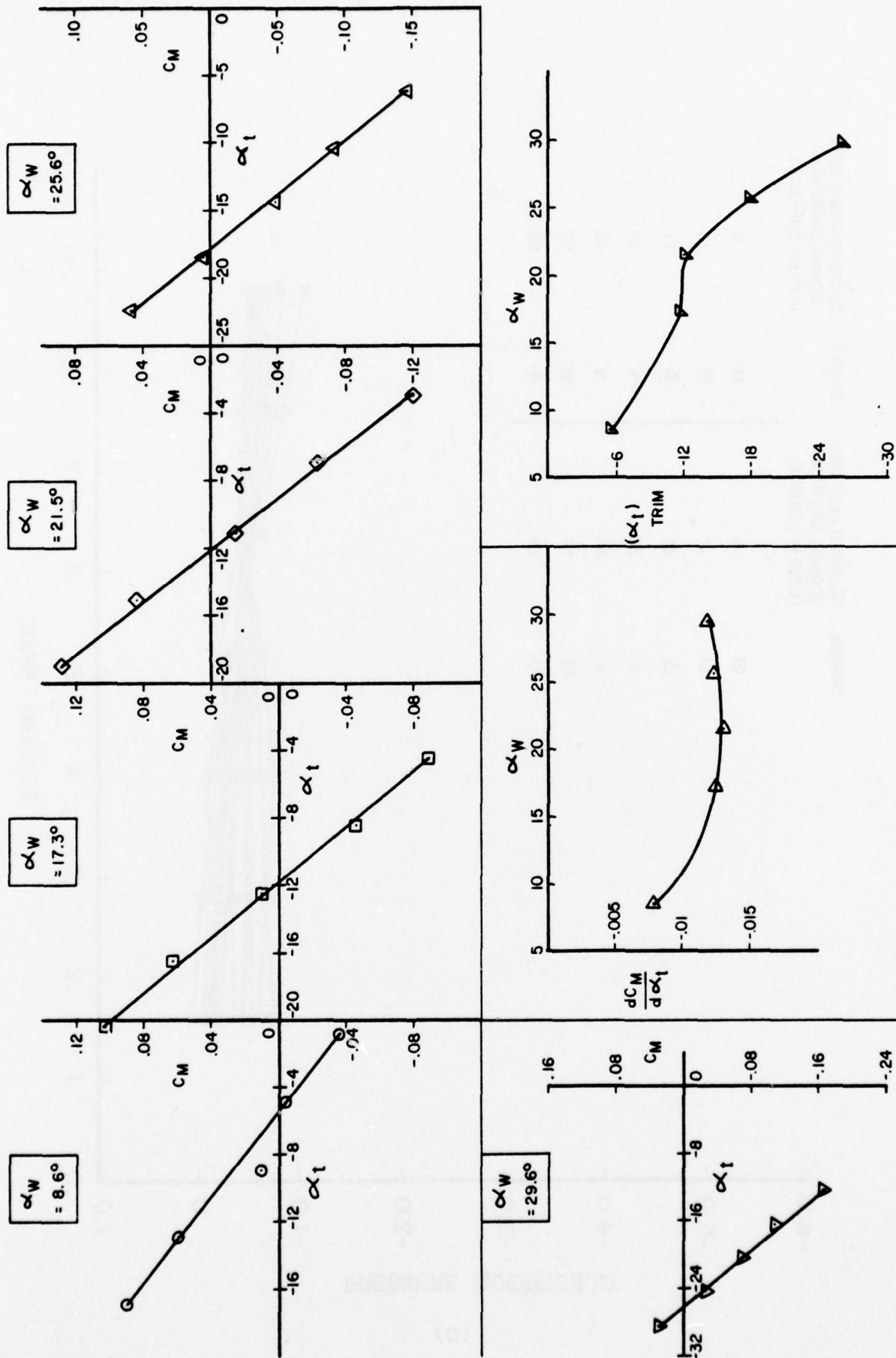
FIGURE 32: Tail Effectiveness of Configuration 1-60-03B.
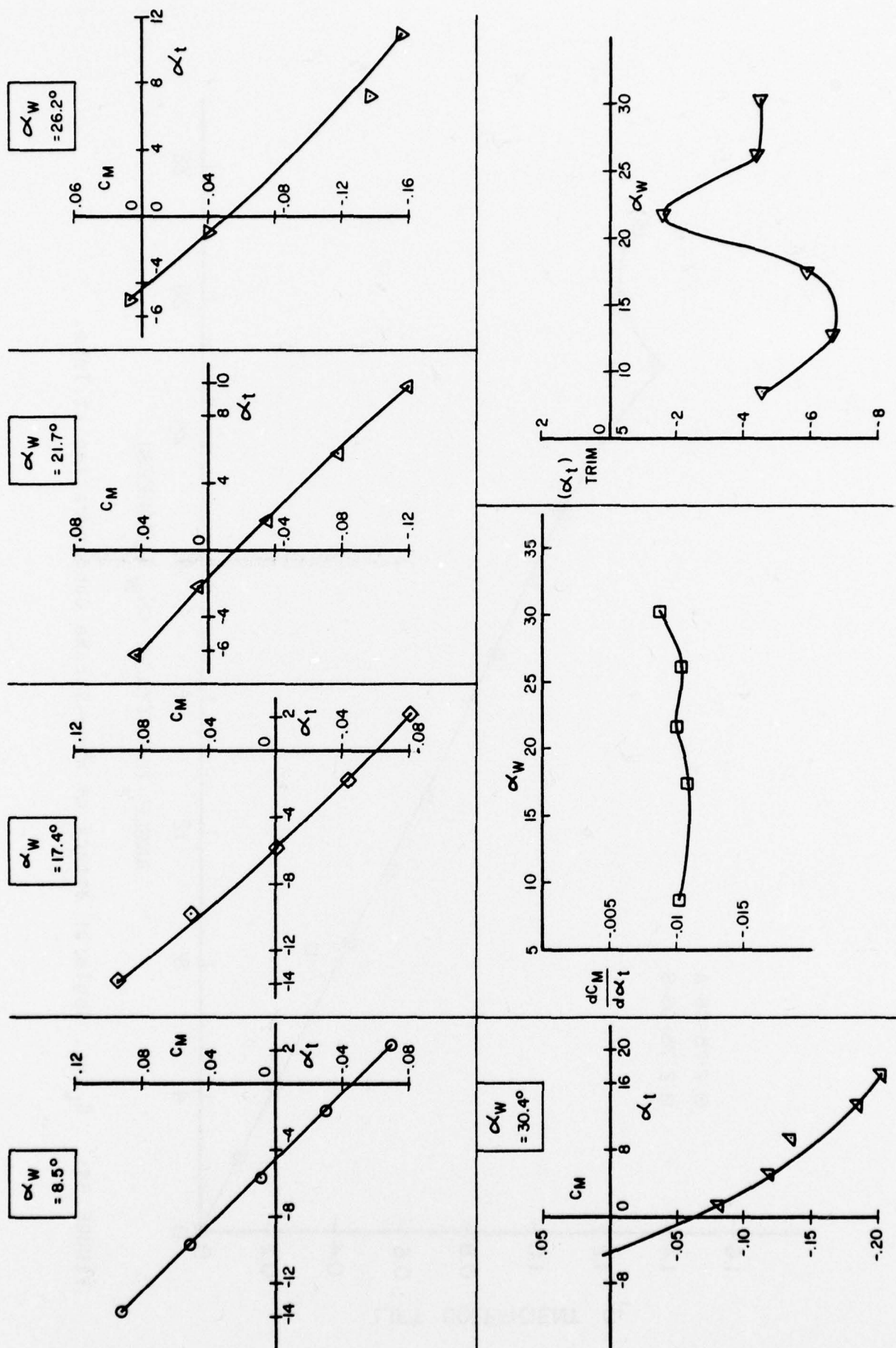
FIGURE 33: Tail Effectiveness of Configuration 2-60-03B.
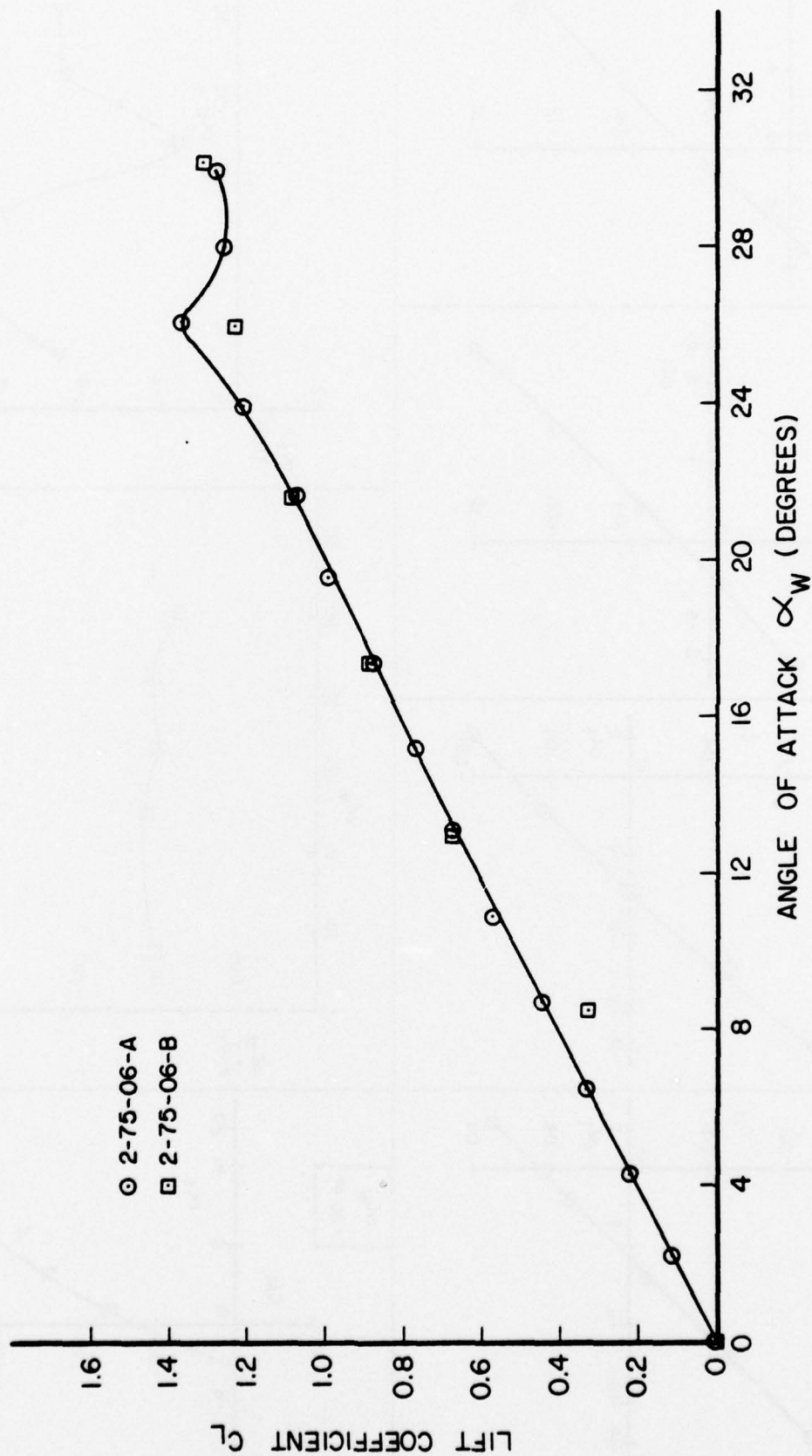
FIGURE 34: C_L vs. Angle of Attack of Wing-Strake Configuration at Trim.

110
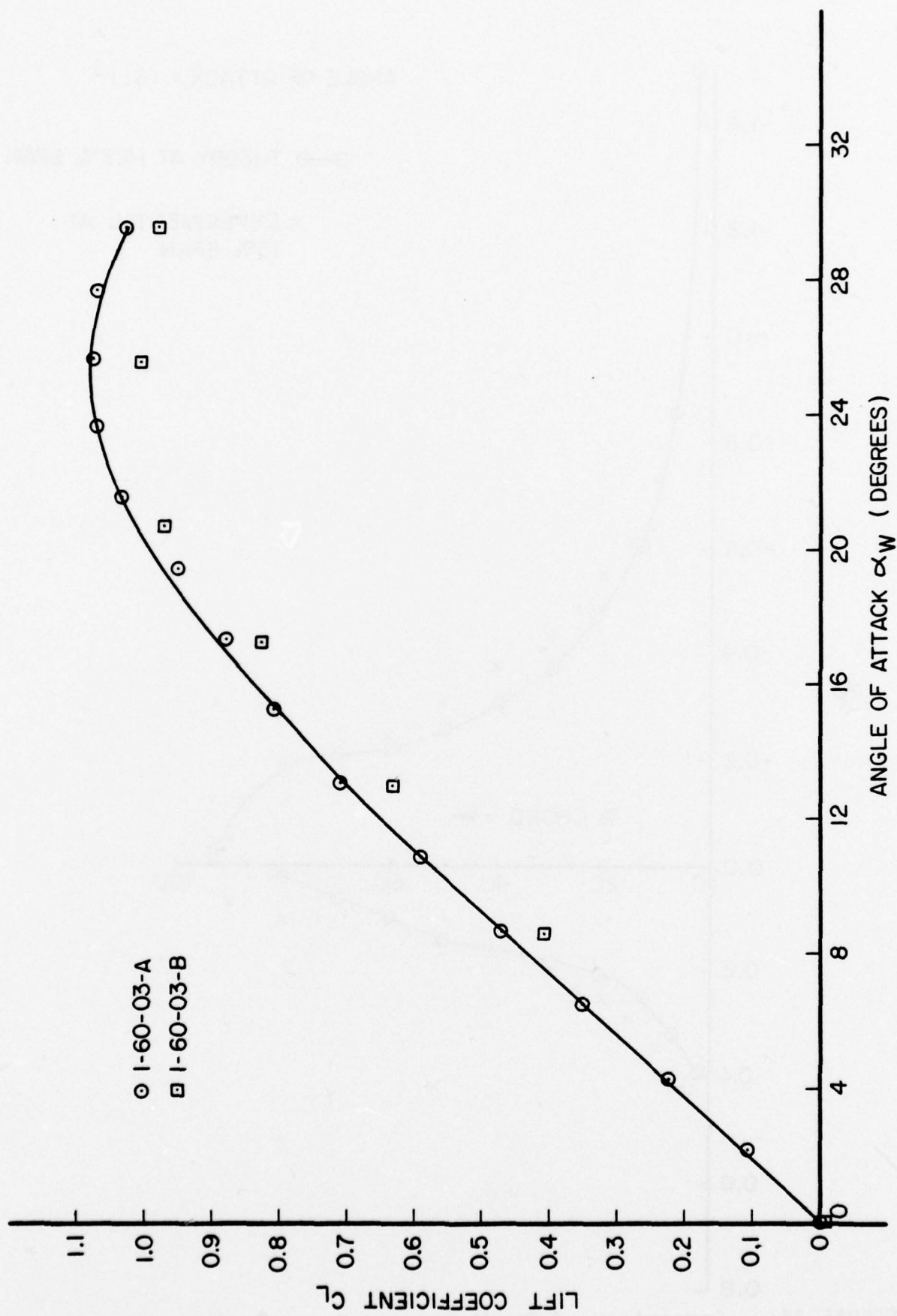
FIGURE 35: C_L vs. Angle of Attack of Wing Configurations at Trim.

ANGLE OF ATTACK α_w (DEGREES)

LIFT COEFFICIENT C_L

⊙ I-60-03-A
▣ I-60-03-B
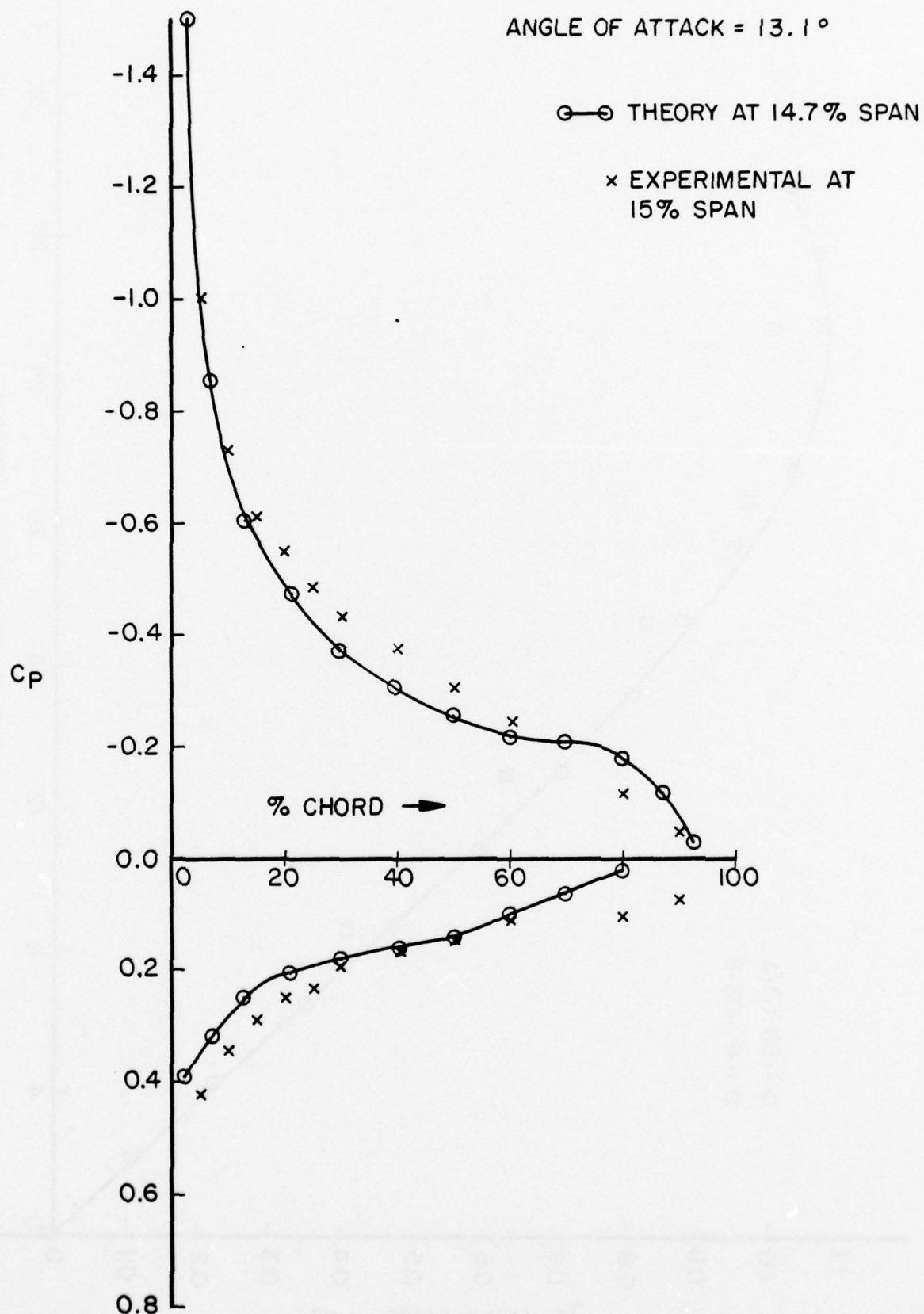
FIGURE 36: Comparison of Predicted and Measured Pressure
Distributions for Unseparated Flow.

112
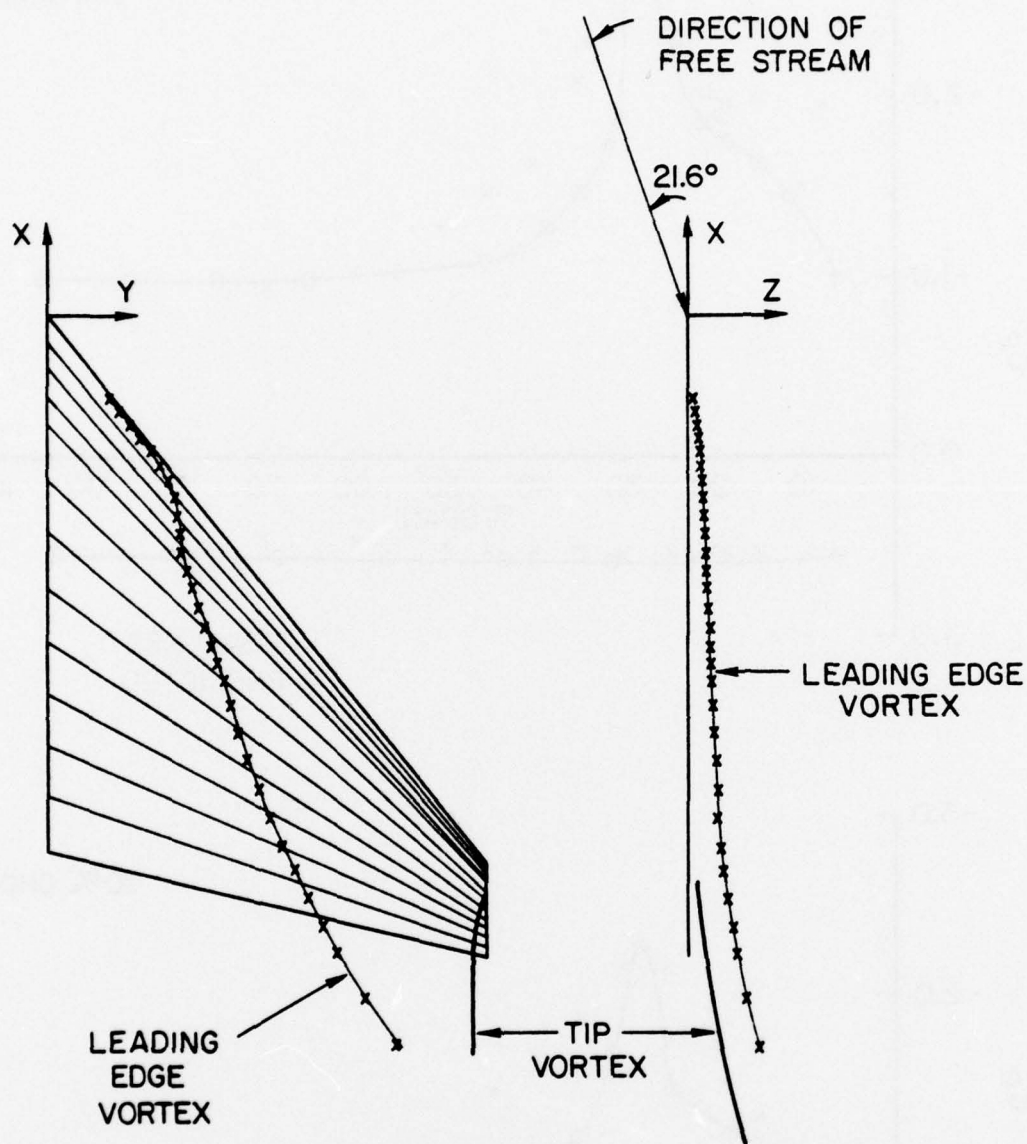
FIGURE 37: Predicted Vortex Geometry for the Basic Wing Configuration α_w = 21.6 Degrees.

113
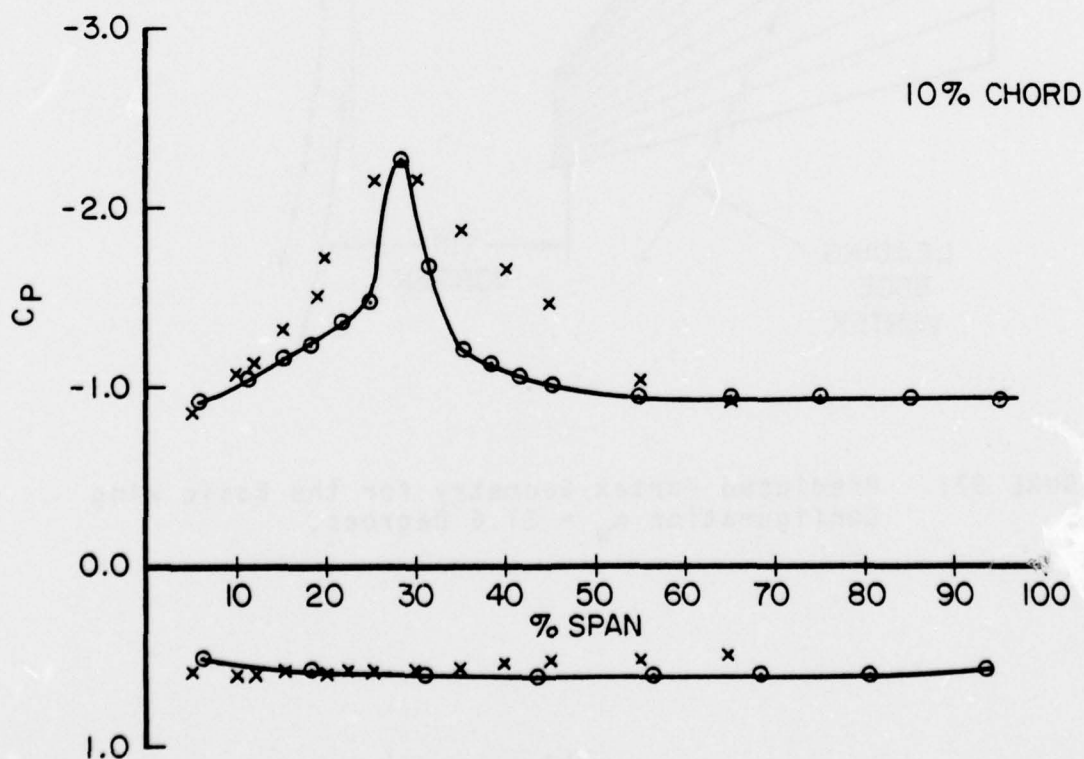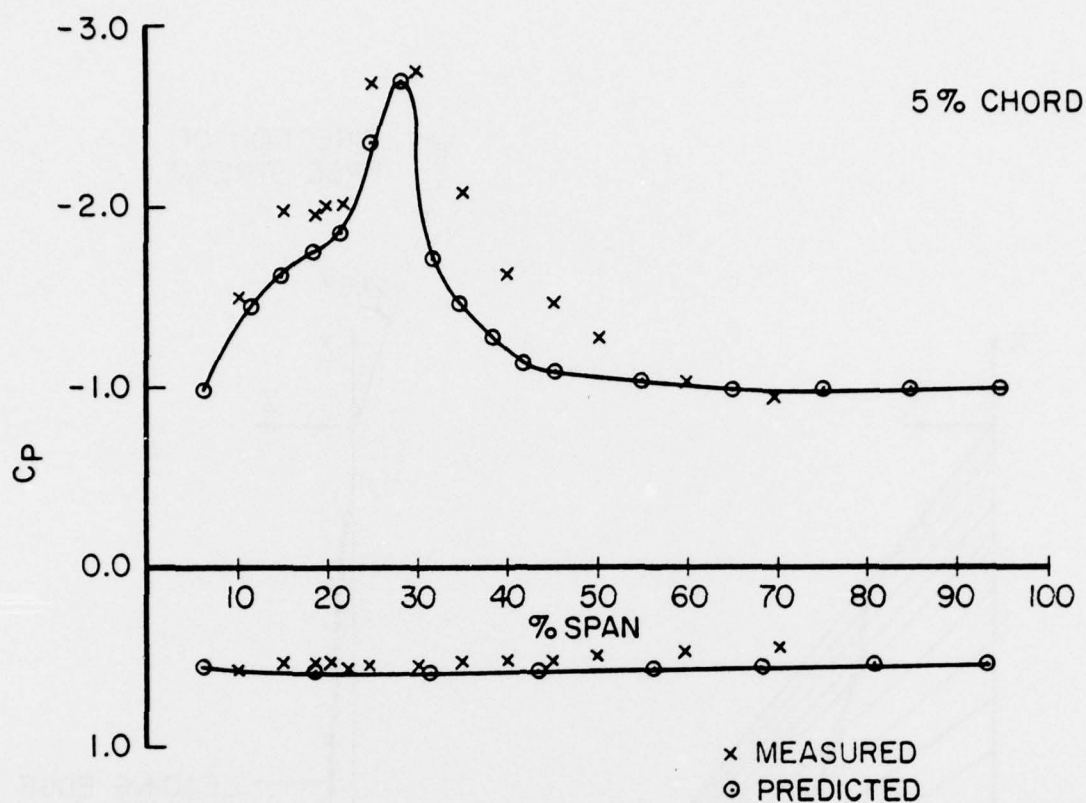
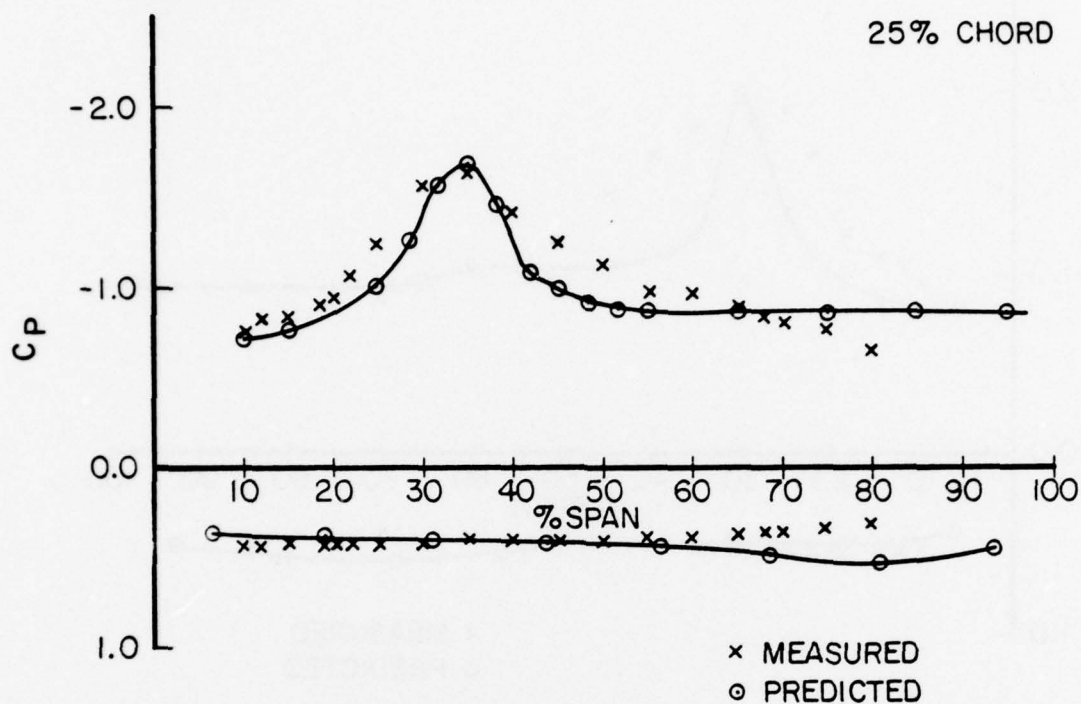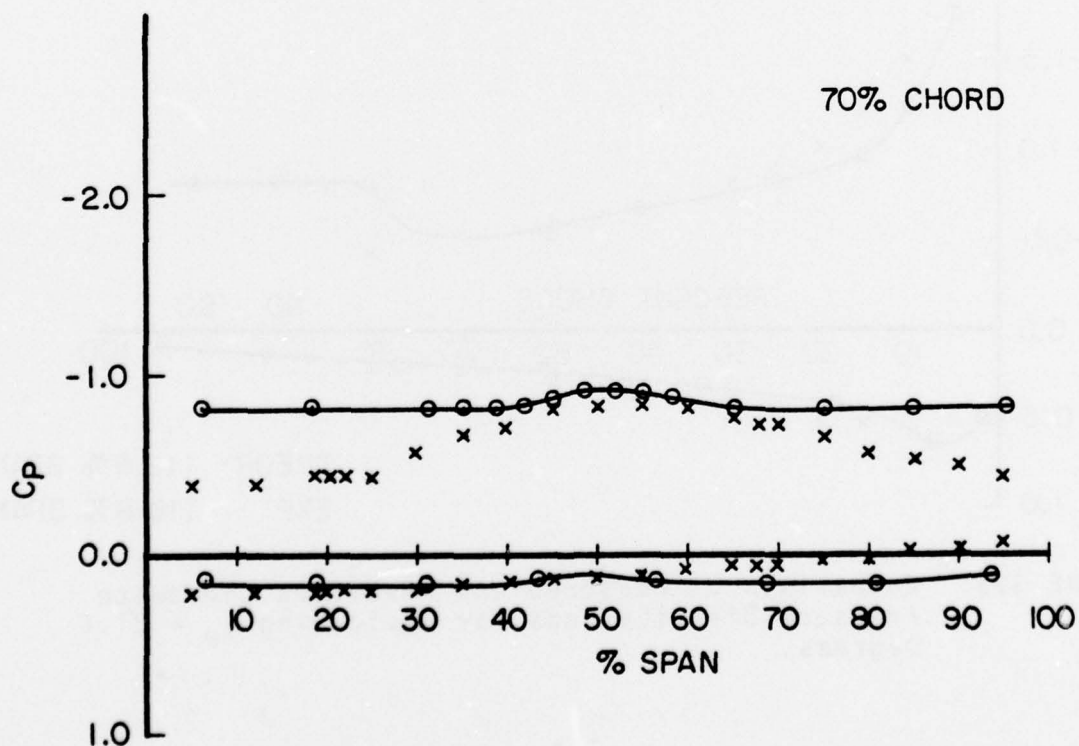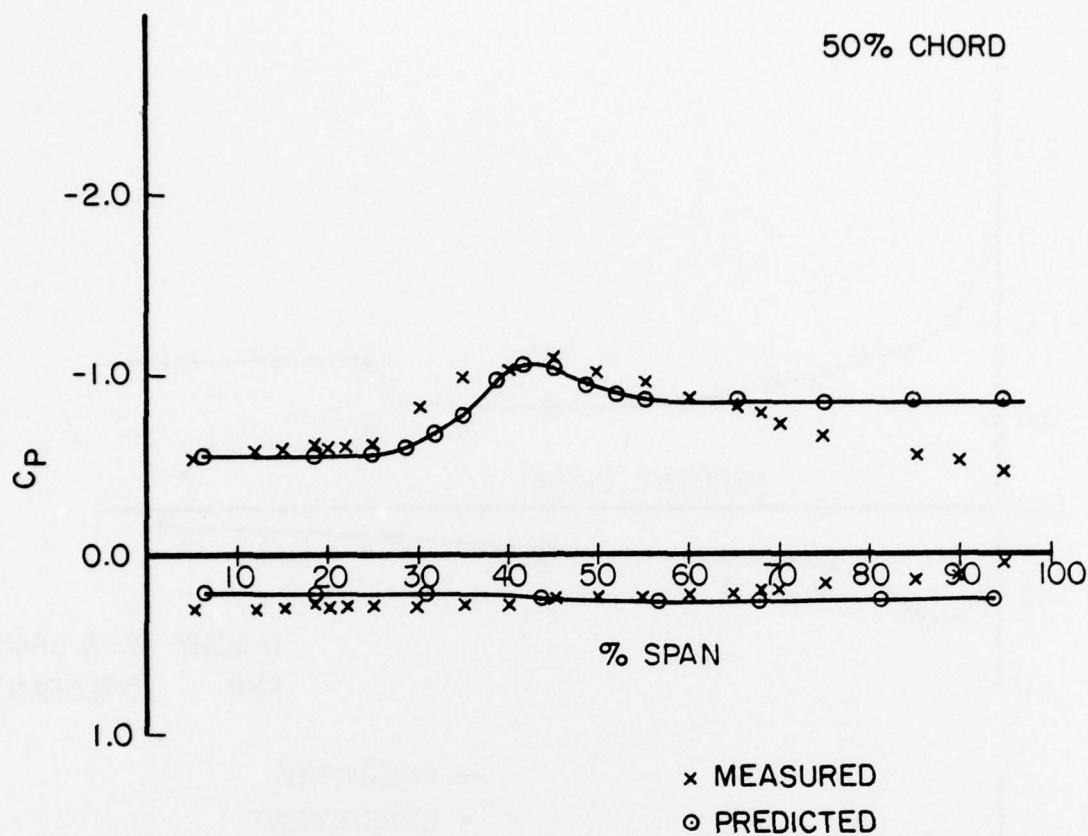FIGURE 38a: Comparison of the Measured and Predicted Spanwise Distribution of Surface Pressures for Basic Wing α_w = 21.6 Degrees.
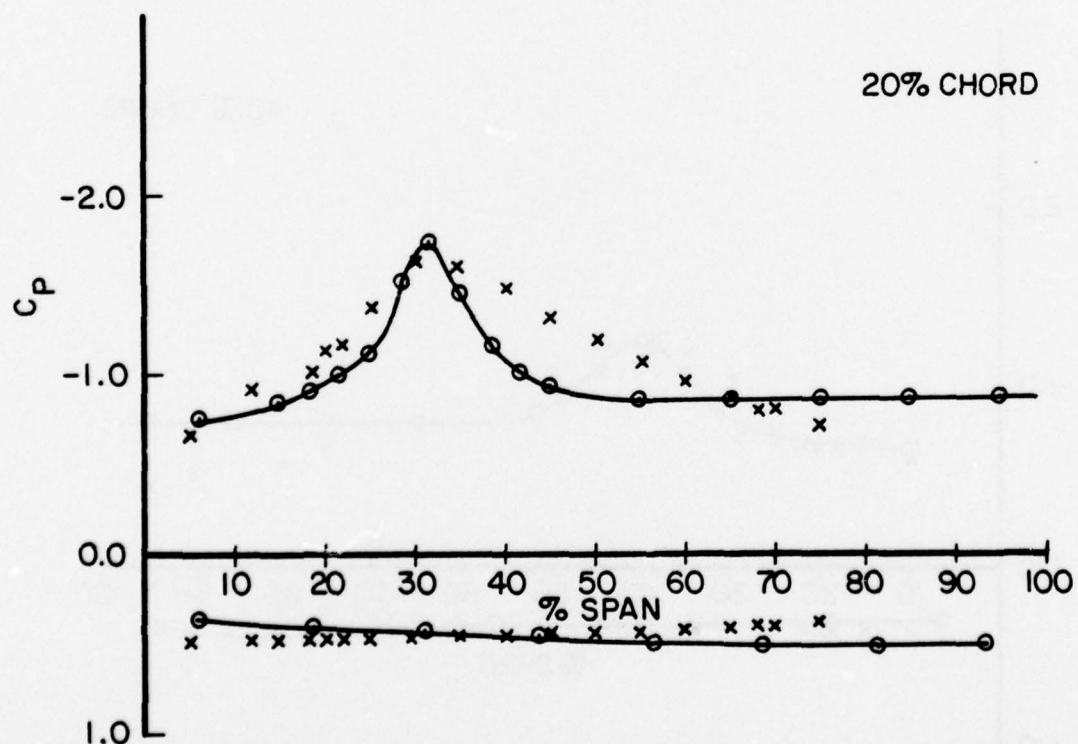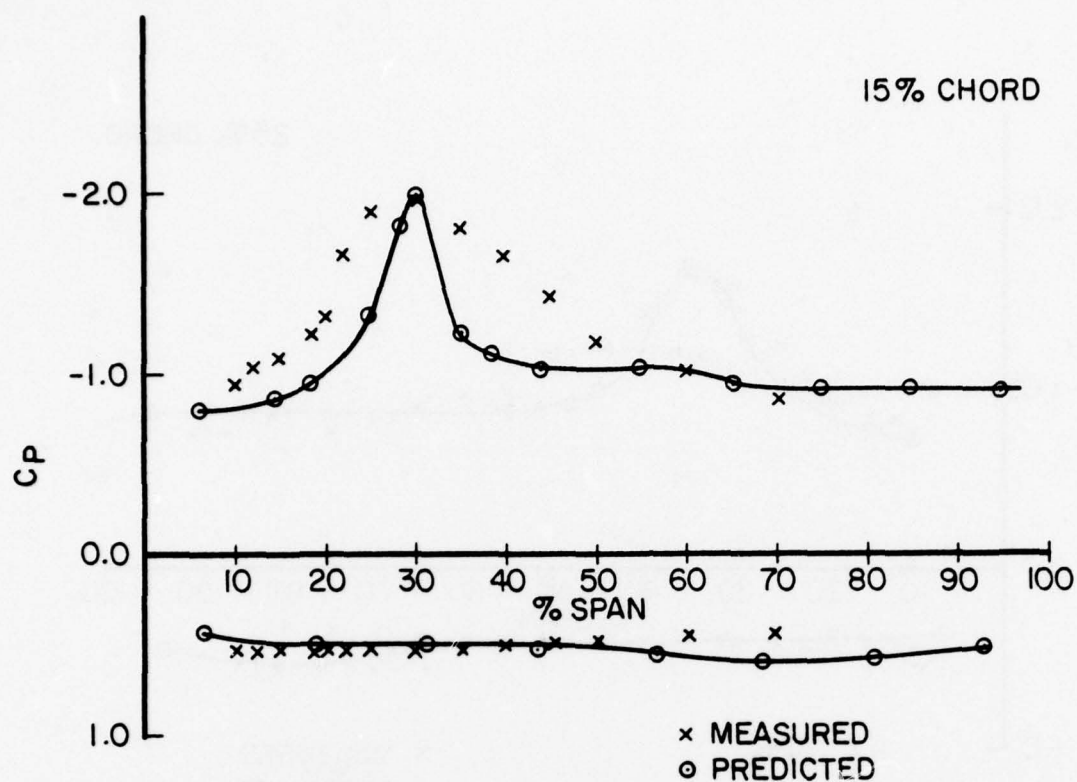
FIGURE 38b: Comparison of the Measured and Predicted Spanwise
Distribution of Surface Pressures for Basic Wing
α_w = 21.6 Degrees.

115
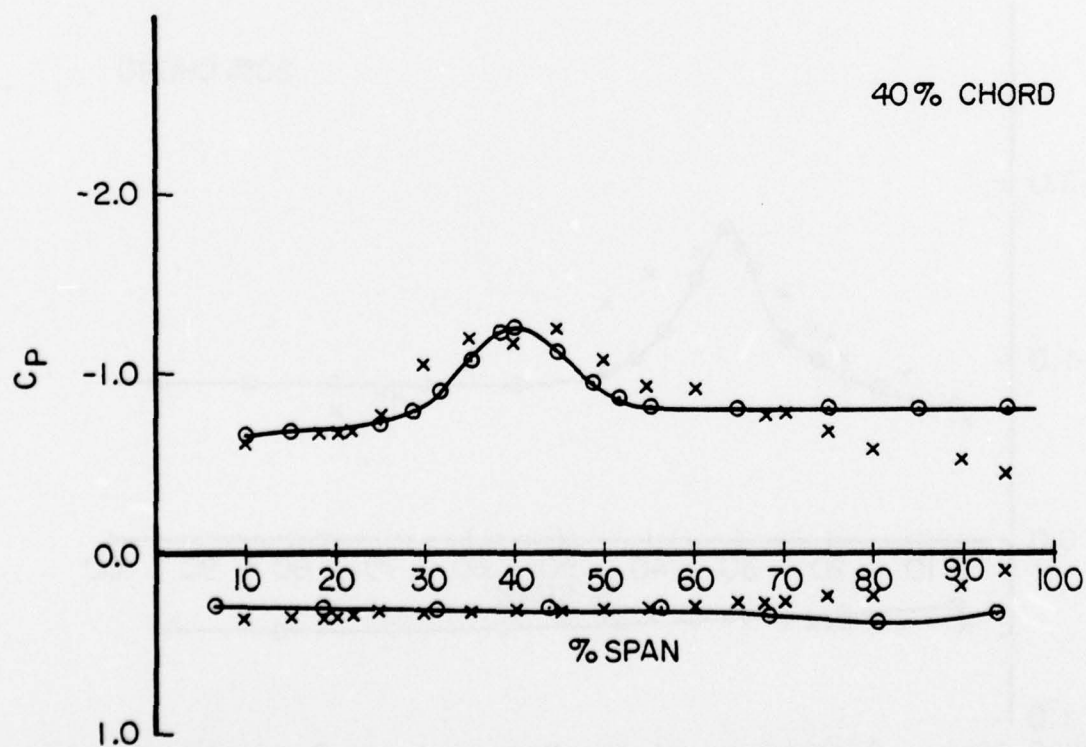
FIGURE 38c: Comparison of the Measured and Predicted Spanwise Distribution of Surface Pressures for Basic Wing α_w = 21.6 Degrees.

FIGURE 38d: Comparison of the Measured and Predicted Spanwise
Distribution of Surface Pressures for Basic Wing
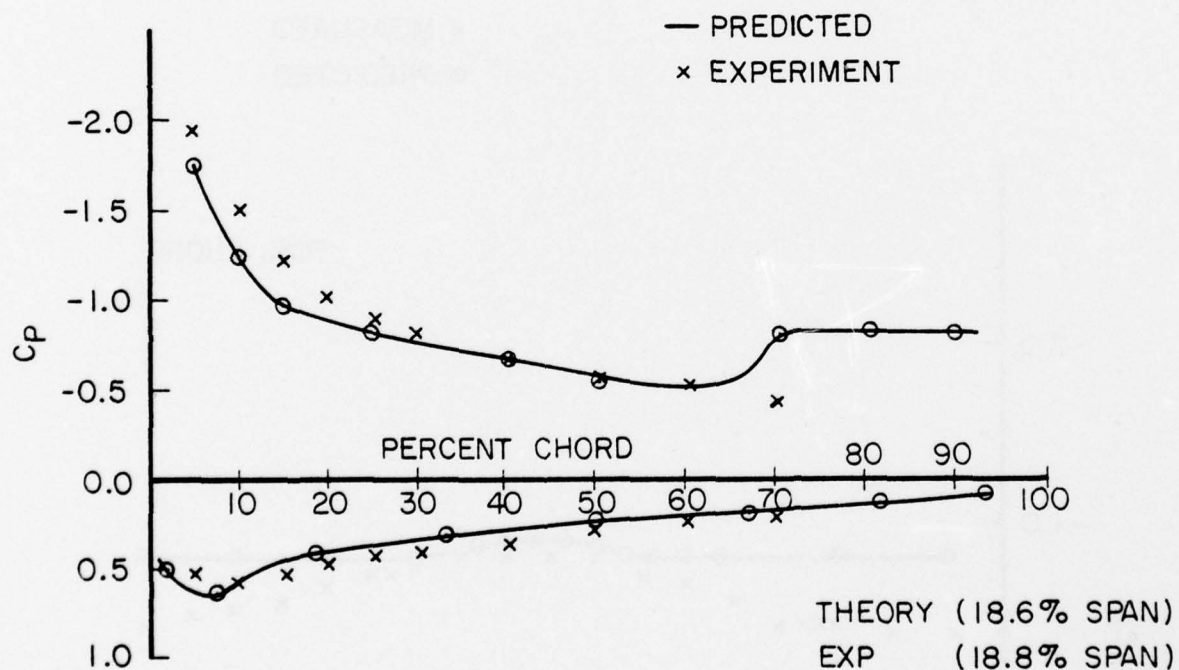α_w = 21.6 Degrees.

117

FIGURE 39a: Comparison of Measured and Predicted Chordwise Pressure Distributions for Basic Wing α_w = 21.6 Degrees.
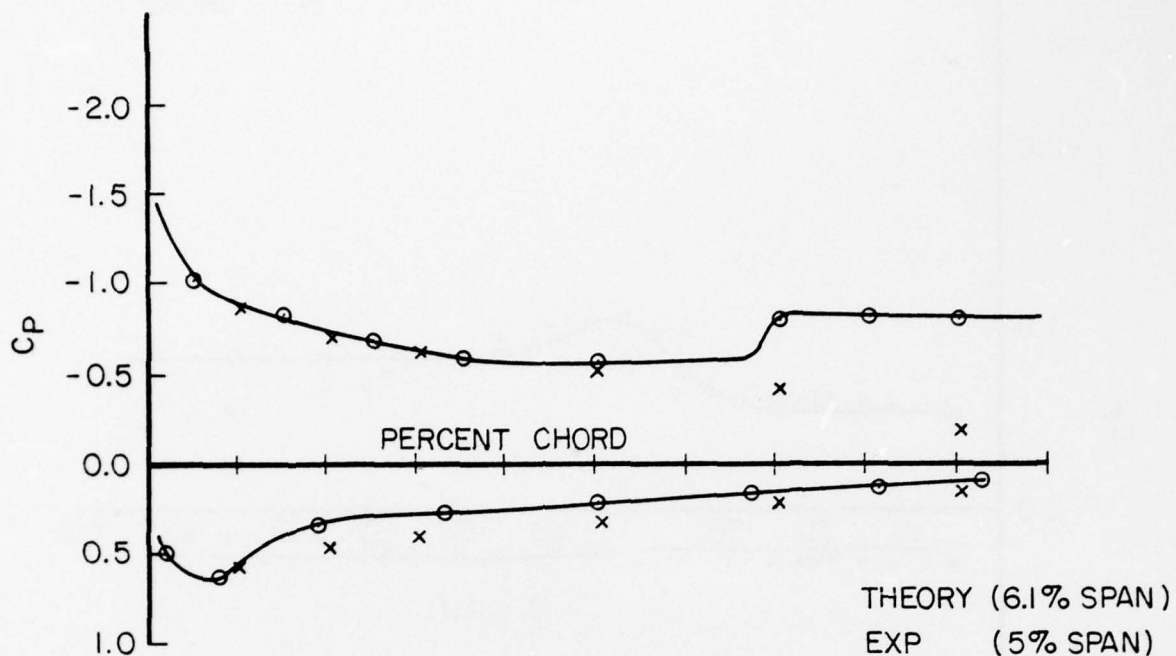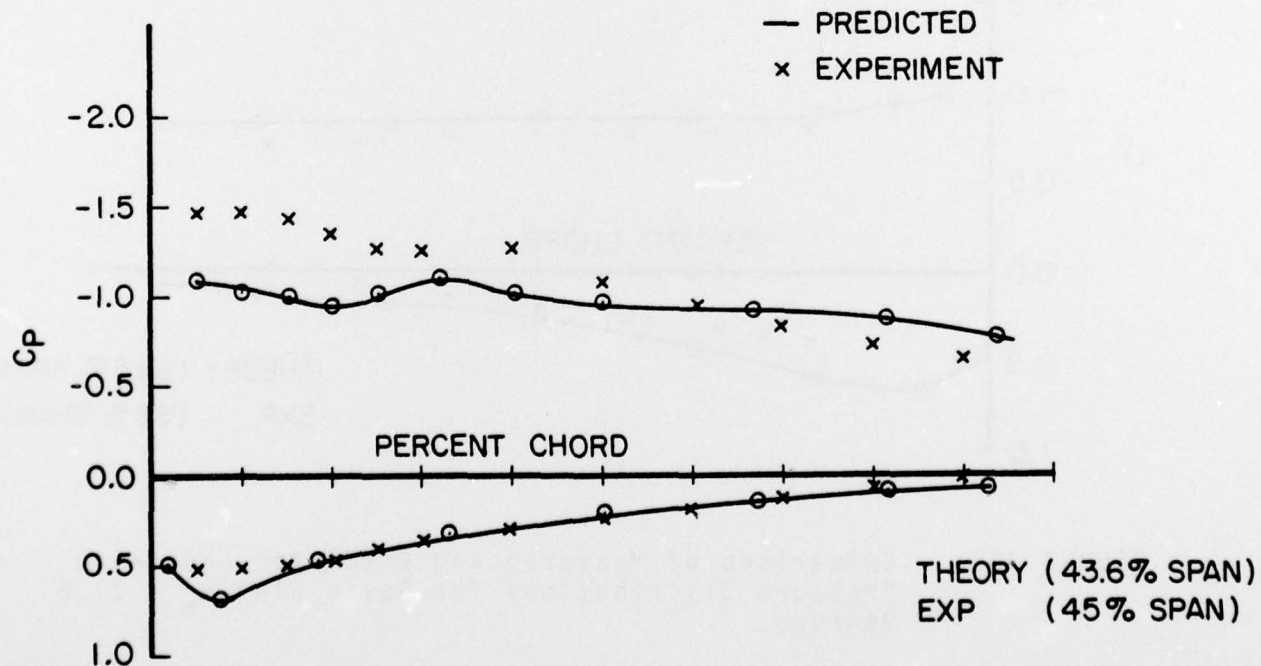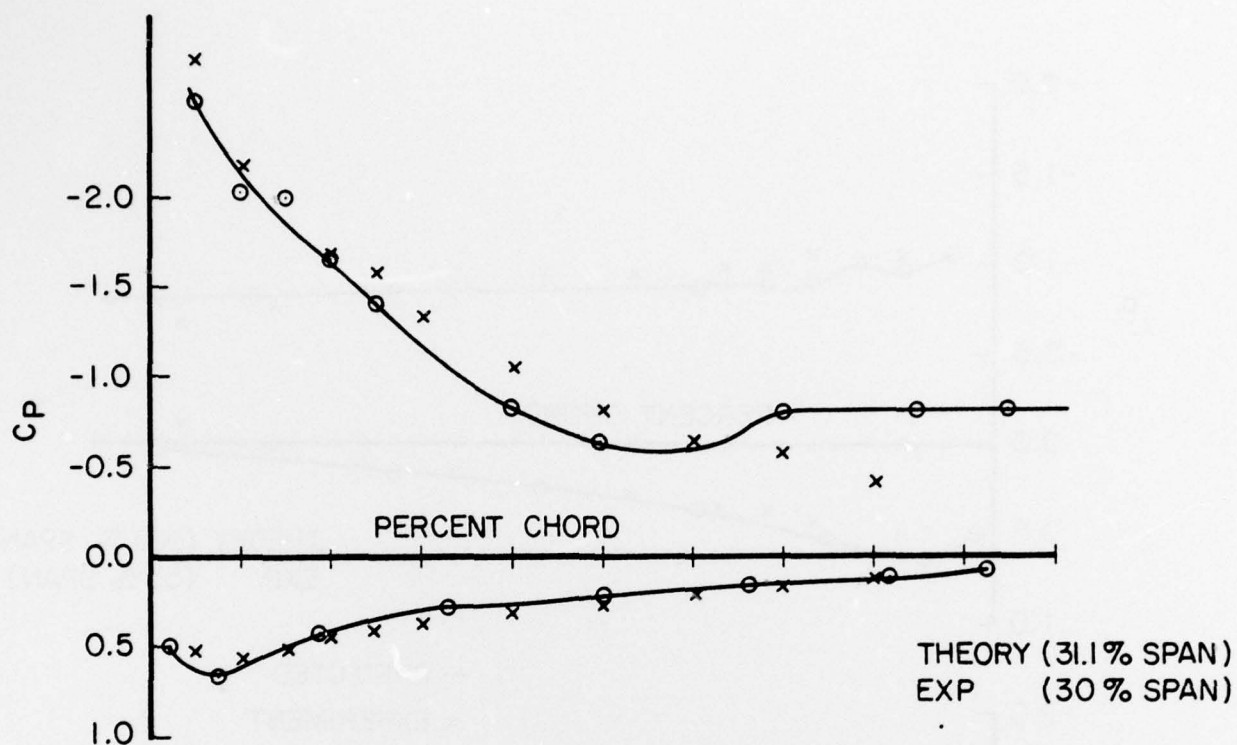
118

FIGURE 39b: Comparison of Measured and Predicted Chordwise Pressure Distributions for Basic Wing α_w = 21.6 Degrees.
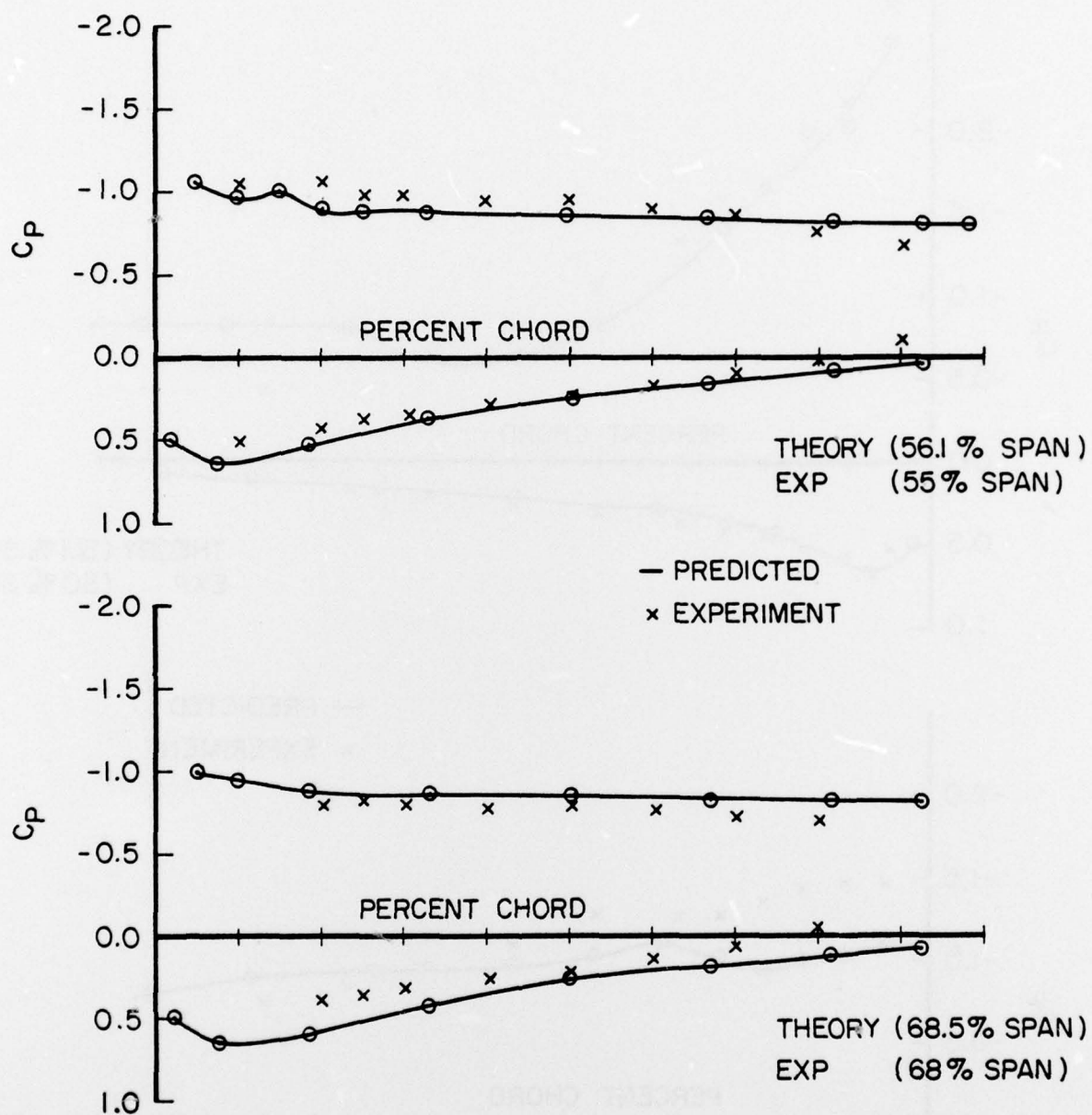
FIGURE 39c: Comparison of Measured and Predicted Chordwise Pressure Distributions for Basic Wing α_w = 21.6 Degrees.
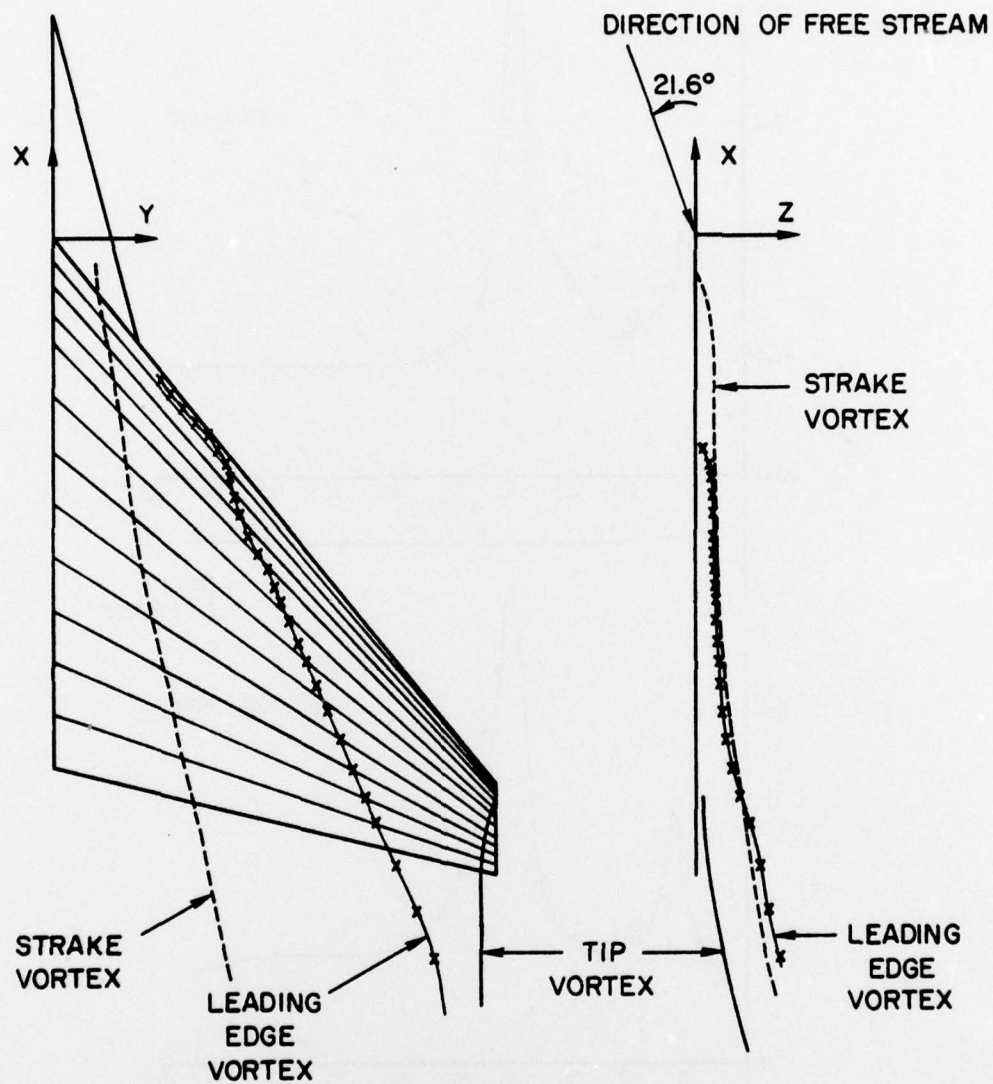
FIGURE 40: Predicted Vortex Geometry for the Wing-Strake Configuration at $\alpha_w = 21.6$ Degrees.

121

FIGURE 41a: Comparison of the Measured and Predicted Chordwise Pressure Distributions for Basic Wing α_w = 21.6 Degrees.

122

FIGURE 41b: Comparison of the Measured and Predicted
Chordwise Pressure Distributions for Basic
Wing α_w = 21.6 Degrees.

123
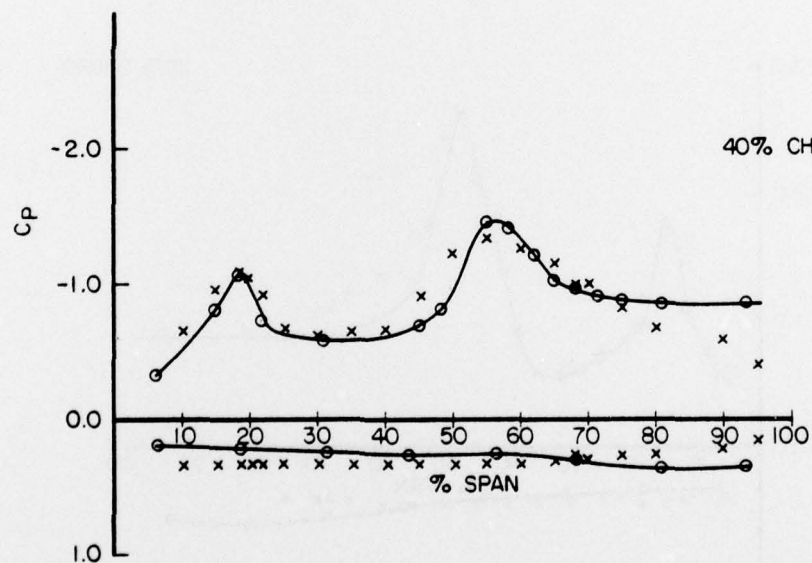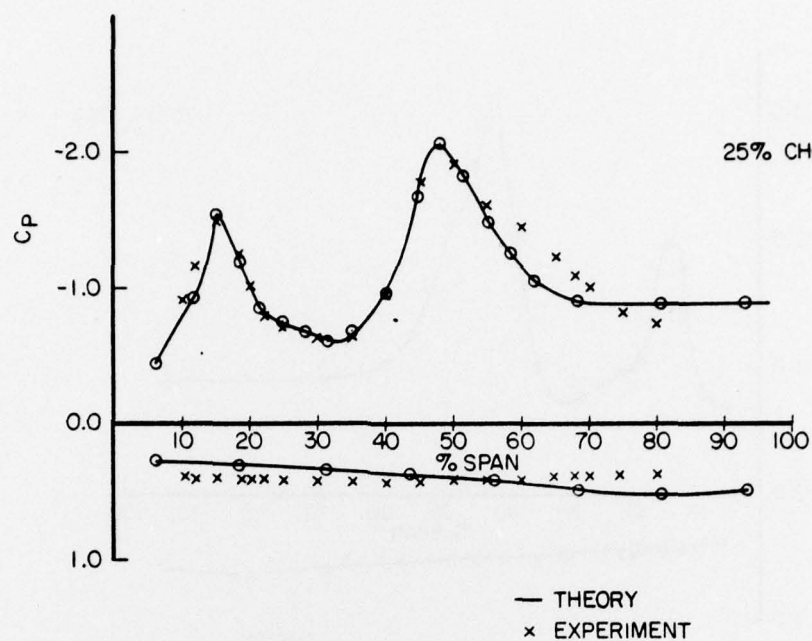
FIGURE 41c: Comparison of the Measured and Predicted Chordwise Pressure Distributions for Basic Wing α_w = 21.6 Degrees.

124
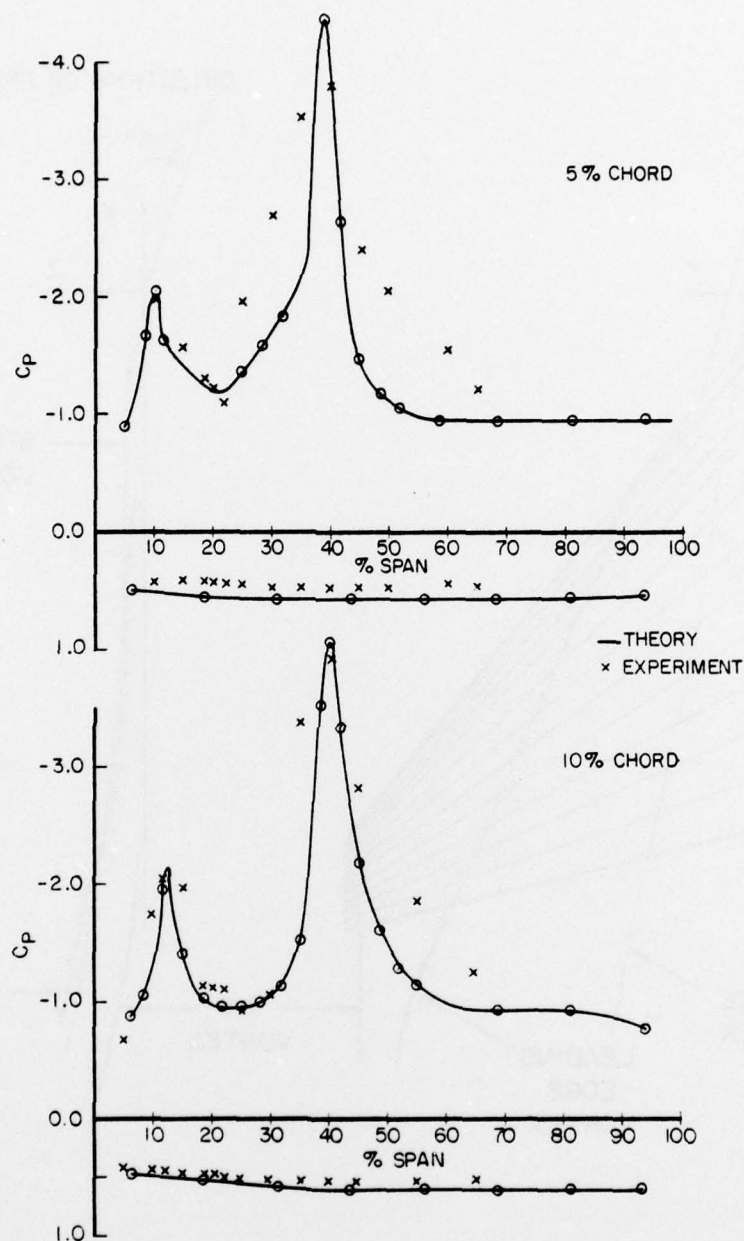
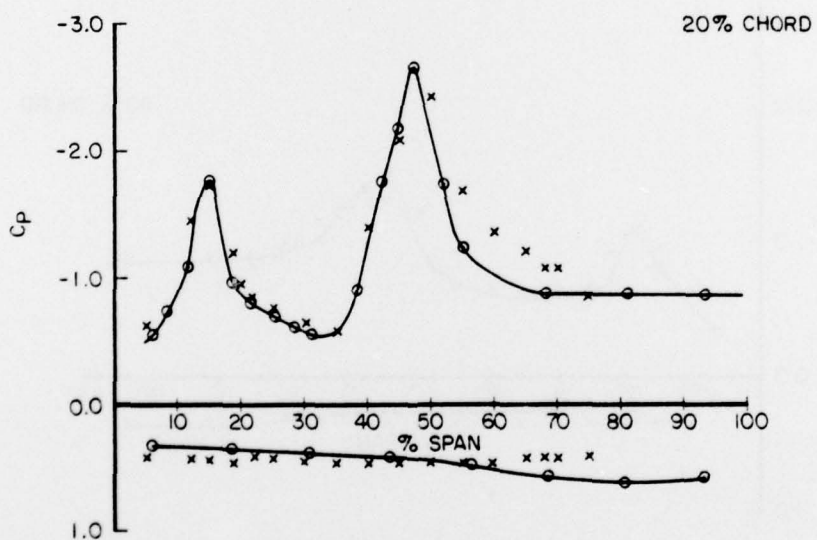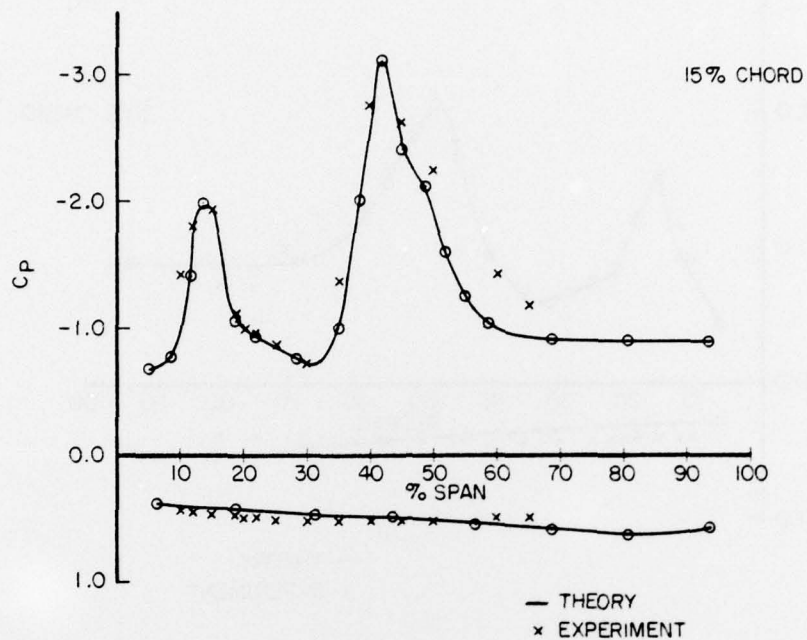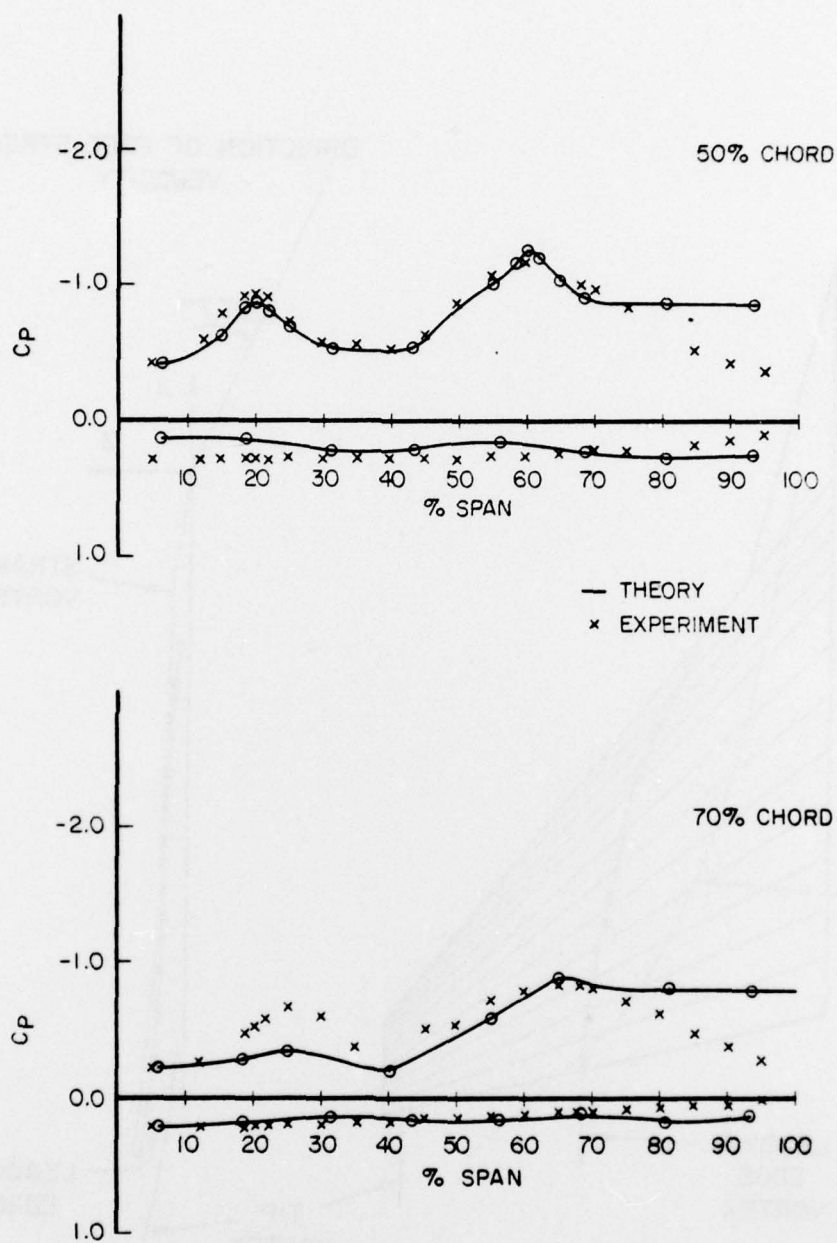FIGURE 41d: Comparison of the Measured and Predicted
Chordwise Pressure Distributions for Basic
Wing α_w = 21.6 Degrees.

FIGURE 42: Predicted Vortex Geometrics for the Wing-Strake Configuration at an Angle of Attack of 27.7 Degrees.
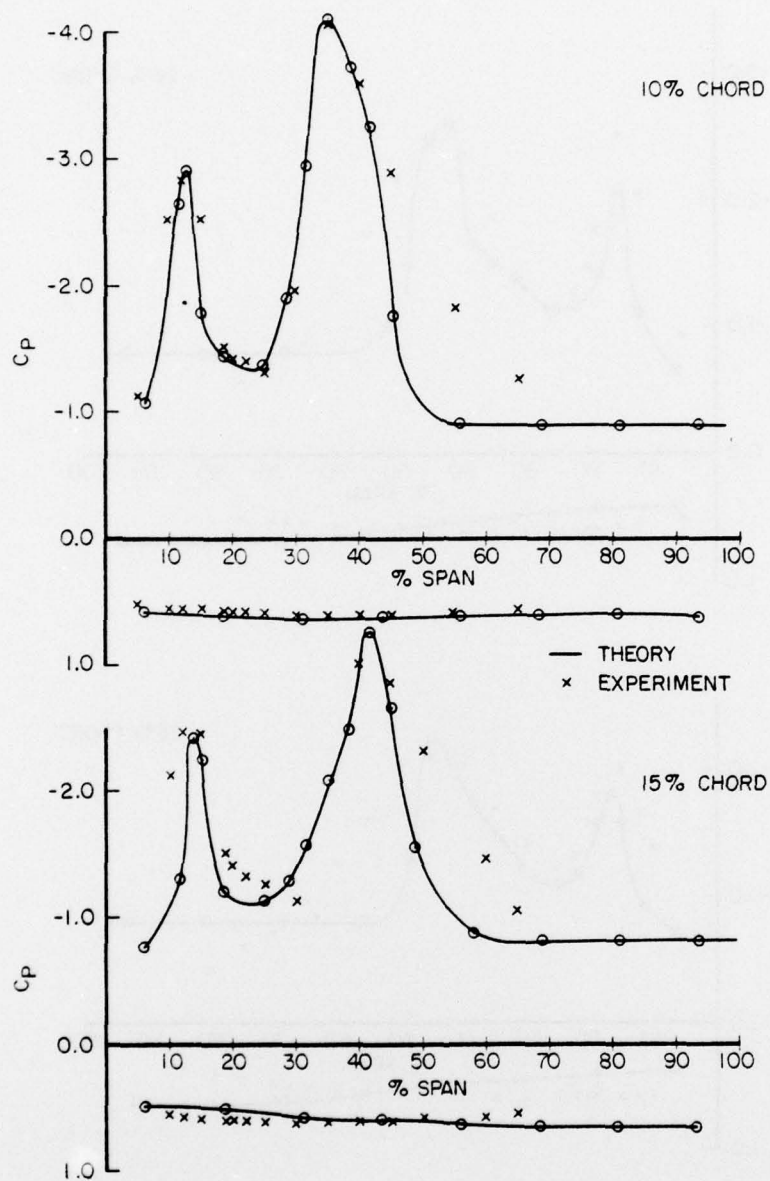
FIGURE 43a: Comparison of the Measured and Predicted Spanwise Distributions of Surface Pressures for Wing-Strake Configuration α_W = 27.7 Degrees.

127
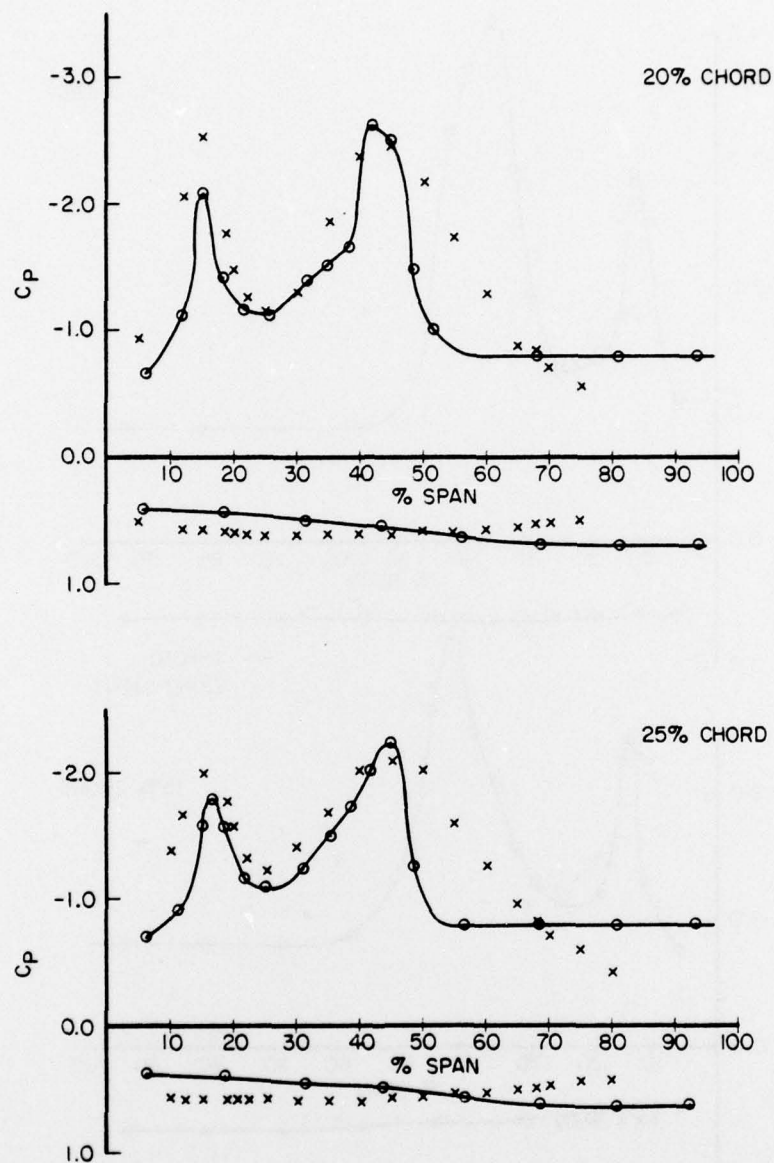
FIGURE 43b: Comparison of the Measured and Predicted Spanwise Distributions of Surface Pressures for Wing-Strake Configuration α_w = 27.7 Degrees.

128

TABLE I
TAIL PRESSURE TAPS - DESIGNATION, LOCATION

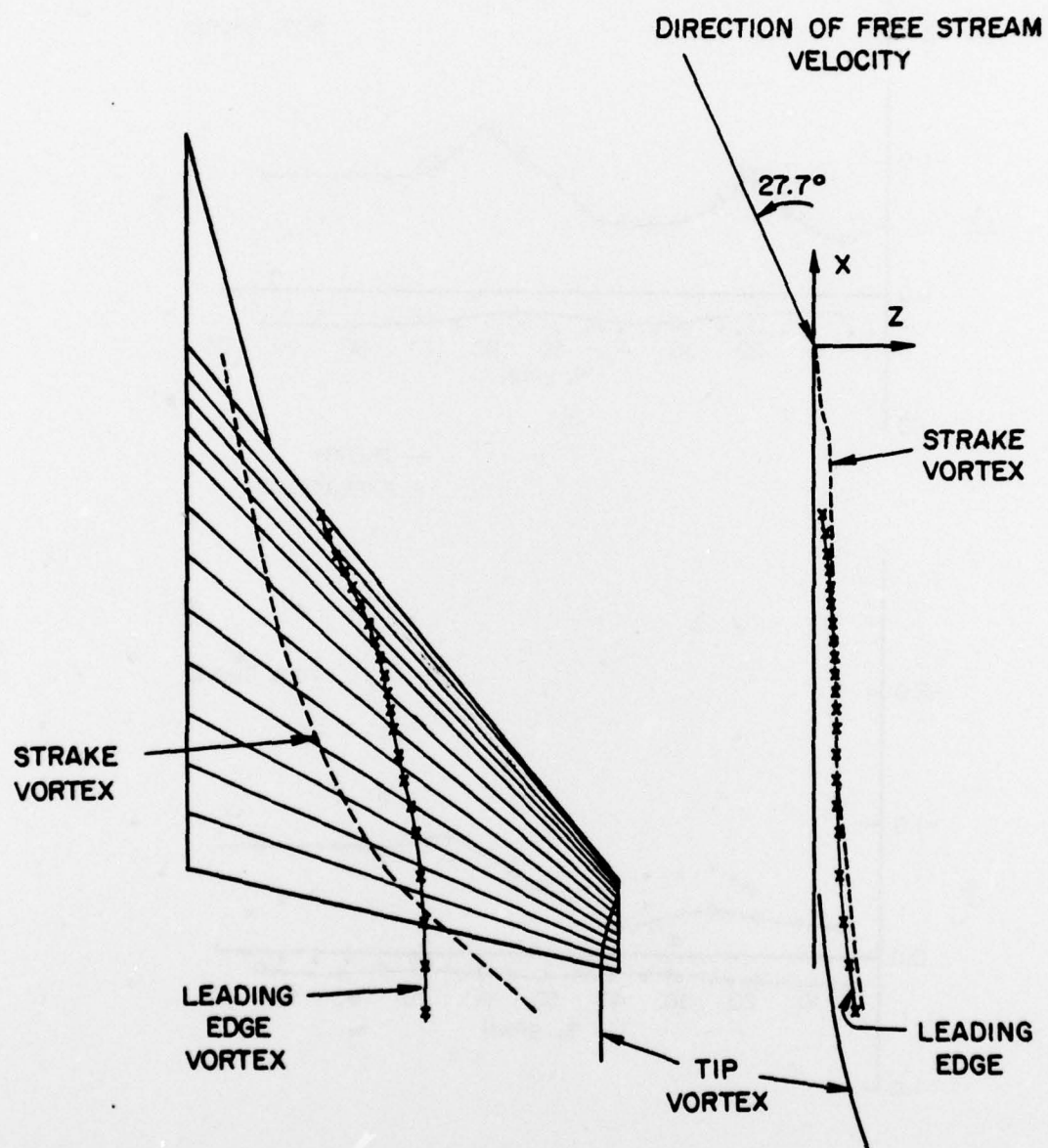| Spanwise Station -Percent of Span	Rightside (Looking Upstream) Chordwise Station - % C							Leftside (Looking Upstream) Chordwise Station - % C						
	5	13	21	30	40	50	65	9	17	25	35	45	55	75
16	307	314	321	328	335	342	349	356	363	370	377	384	391	398
28	306	313	320	327	334	341	348	355	362	369	376	383	390	397
40	305	312	319	326	333	340	347	354	361	368	375	382	389	396
52	304	311	318	325	332	339	346	353	360	367	374	381	385	395
64	303	310	317	324	331	338	345	352	359	366	373	380	387	394
76	302	309	316	323	330	337	344	351	358	365	372	379	386	393
88	301	308	315	322	329	336	343	350	357	364	371	378	385	392

TABLE II

SUMMARY OF TEST CONFIGURATIONS

Run Number	Configuration Designation	Longitudinal Separation L In Inches	Horizontal (Lateral) Separation In Tenths Of Tail Root Chord	Description of the Configuration
1	1-75-00-A	75	0	Basic wing with a leading edge snag
2	1-75-00-A	75	0	Basic wing with a leading edge snag
3	1-60-03-A	60	3	Basic wing with a leading edge snag
4	1-60-09-A	60	9	Basic wing with a leading edge snag
5	2-75-12-A	75	12	Basic wing with a leading edge snag + a root strake
6	2-75-06-A	75	6	Basic wing with a leading edge snag + a root strake
7	2-75-00-A	75	0	Basic wing with a leading edge snag + a root strake
8	2-75-12-B	75	12	Basic wing with a leading edge snag + a root strake + tail
9	2-75-12-B	75	12	Basic wing with a leading edge snag + a root strake + tail
10	2-75-12-B	75	12	Basic wing with a leading edge snag + a root strake + tail
11	2-75-06-B	75	6	Basic wing with a leading edge snag + a root strake + tail
12	1-75-06-B	75	6	Basic wing with a leading edge snag $\pm$ tail
13	1-75-12-B	75	12	Basic wing with a leading edge snag + tail
14	1-60-03-B	60	3	Basic wing with a leading edge snag + tail
15	2-60-03-B	60	3	Basic wing with a leading edge snag + a root strake + tail

130

DISTRIBUTION LIST

Office of Naval Research
800 N. Quincy St.
Arlington, VA 22217
  ONR 211   4
  ONR 430B   1

Office of Naval Research Branch
  Office
1030 E. Green St.
Pasadena, CA 91106   1

Office of Naval Research Branch
  Office
Bldg. 114 Section D
666 Summer St.
Boston, MA 02210   1

Office of Naval Research Branch
  Office
536 South Clark St.
Chicago, IL 60605   1

Defense Contract Administration
  Services Region
866 Malcolm Road
Burlingame, CA 94010   1

Naval Research Laboratory
Washington, DC 20375
  Code 2627   1
  Code 2629   1

Defense Documentation Center
Bldg. 5 Cameron Station
Alexandria, VA 22314   12

Naval Air Systems Command
Washington, DC 20361
  AIR 320C (Mr. W. Volz)   1
  AIR 53012B (Mr. T. F. Martin) 1
  AIR 320D (Mr. R. Siewert) 1

Naval Surface Weapons Center
White Oak Laboratory
Silver Spring, MD 20910
  Code WA-41 (Mr. F. J. Regan) 2

Naval Surface Weapons Center
Dahlgren Laboratory
Dahlgren, VA 22448
  Code DK-21 (Mr. F. L. Stevens) 2
  Code DK-21 (Dr. F. Moore)   1

U. S. Naval Postgraduate School
Monterey, CA 93940
  Dept. of Aeronautics (Code 57) 1
  Library   1

Superintendent
U. S. Naval Academy
Annapolis, MD 21402   1

Naval Weapons Center
China Lake, CA 93555
  Code 4063 (Mr. S. K. Carter) 1
  Code 3914 (Mr. W. H. Clark) 1

Pacific Missile Test Center
Point Mugu, CA 93041
  Code 1241 (Mr. K. A. Larsen) 1

David Taylor Naval Ship Research
  Development Center
Bethesda, MD 20084
  Code 16 (Dr. H. Chaplin)   1
  Code 1660 (Mr. J. Nichols) 1
  Code 522.3 Aero Library   1

Naval Air Development Center
Warminster, PA 18974
  Code 6053 (Mr. C. Mazza)   1
  Code 303 (Dr. E. McQuillen) 1

NASA Langley Research Center
Hampton, VA 23665
  M/S 413 (Mr. W. Sawyer)   1
  M/S 406 (Mr. C. Jackson)   1
  Dr. J. Campbell   1

NASA Ames Research Center
Moffett Field, CA 94035
  FAR Branch (Dr. G. Chapman) 1
  FAE Branch (Dr. T. Gregory) 1

Wright Patterson Air Force Base
Dayton, OH   45433
  AFFDL/FGC (Mr. E. L. Fleeman)   1
  AFFDL/FGC (Mr. J. Olsen)   1

Eglin Air Force Base
Eglin, FL   32542
  AFATL/DLDL (Mr. D. C. Daniel)   1
  AFATL/DLMA (Mr. C. B. Butler)   1

Arnold Engineering Development Center
Arnold AF Station, TN   37389
  AEDC/DYR (Mr. E. R. Thompson)   1

Air Force Office of Scientific Research
Bolling AFB, DC   20332
  Code NA (Dr. J. Wilson)   1

Defense Advanced Research Projects
  Agency
1400 Wilson Boulevard
Arlington, VA   22209
  Mr. R. Moore   1

Lockheed Missiles & Space Co., Inc.
Huntsville Research & Engineering
  Center
P. O. Box 1103
Huntsville, AL   35807
  Mr. A. Zalay   1

Nielsen Engineering & Research, Inc.
510 Clyde Avenue
Mountain View, CA   94043   1

Northrop Corporation
Ventura Division
1515 Rancho Conejo Blvd.
Newbury Park, CA   91320
  Dr. A. Wortman   1

Lockheed-Georgia Company
Department 72-74, Zone 403
Marietta, GA   30063
  Mr. Charles Dixon   1

Boeing Aircraft Company
P. O. Box 3707
Seattle, WA   98124
  Dr. P. Rubbert   1

Analytical Methods, Inc.
100 - 116th Avenue, S.E.
Bellevue, WA   98004
  Dr. F. Dvorak   1

General Dynamics/Convair Division
Kearny Mesa Plant
P. O. Box 80847
San Diego, CA   92138
  Dr. E. Levinsky   1

Virginia Polytechnic Institute and
  State University
Engineering Science Dept.
Blacksburg, VA   24061
  Dr. D. Mook   1

Massachusetts Institute of Technology
Dept. of Aeronautics and Astronautics
Cambridge, MA   02139
  Prof. S. Widnall   1

McDonnell Douglas Aircraft Company
P. O. Box 516
St. Louis, MO   63166
  Dept. 241 (R. B. Jenny)   1
             (J. F. Mello)   1
             (C. W. Miller)   1
  Dept. 230 (R. W. McDonald)   1

Sandia Laboratories
Technical Library
Albuquerque, NM   87115
  Mr. D. Barnette   1

Polytechnic Institute of New York
Farmingdale, NY   11735
  Aerodynamics Laboratories
    (Prof. P. Sforza)   1

Advanced Technology Center, Inc.
P. O. Box 6144
Dallas, TX   75222
  Dr. G. Hough   1

University of Maryland
College of Engineering
Dept. of Aerospace Eng.
College Park, MD   20742
  Dr. J. Anderson, Jr.   1